

Generation and Detection of Short Optical Pulses Using Semiconductor Devices

by

Mohammad Mehdi Karkhanehchi

A thesis submitted to the Faculty of Engineering,
Department of Electronics and Electrical Engineering
of the University of Glasgow for the degree of
Doctor of Philosophy.

March 1997

©Mohammad Mehdi Karkhanehchi, 1997

ProQuest Number: 13815457

All rights reserved

INFORMATION TO ALL USERS

The quality of this reproduction is dependent upon the quality of the copy submitted.

In the unlikely event that the author did not send a complete manuscript and there are missing pages, these will be noted. Also, if material had to be removed, a note will indicate the deletion.



ProQuest 13815457

Published by ProQuest LLC (2018). Copyright of the Dissertation is held by the Author.

All rights reserved.

This work is protected against unauthorized copying under Title 17, United States Code
Microform Edition © ProQuest LLC.

ProQuest LLC.
789 East Eisenhower Parkway
P.O. Box 1346
Ann Arbor, MI 48106 – 1346

Thesis
10737
Copy 1



Acknowledgements

The work in this thesis could not have been performed without the multitude of facilities in the Department of Electronics and Electrical Engineering, Glasgow University. Furthermore, this thesis would not have been possible without the help and support of a number of people.

Firstly, I would like to thank Professor John Marsh, my supervisor. His encouragement, interest, advice, extreme patience, and friendship have been invaluable throughout my research and writing up this thesis.

I thank the members of the academic, technical and administrative staff of the Department of Electronics and Electrical Engineering of the University of Glasgow who contributed directly or indirectly to the completion of this project. Also, in the Optoelectronics Group, special thanks to Catrina Bryce, Steve Ayling, Karen McIlvaney, David Barrow, Ooi Boon Siew, Craig Hamilton, David Hutchings and Jim Gray for their help and guidance.

I also thank all the staff, in the MBE facilities in the Department and the MOCVD facilities in Sheffield, who provided me with high grade material and characterisation.

Furthermore, the Ministry of Culture and Higher Education of I. R. of Iran, is gratefully acknowledged for financial support.

After all this is said, there is one person I would like to thank the most: my wife for her patience, help, and understanding. And with this I dedicate this thesis to my wife and my children; Mojdeh, Atyeh and Sara.

Abstract

The design, fabrication and characterisation of semiconductor waveguide autocorrelator, as a device for use in the analysis of ultra-short pulses, are described.

The initial experiments carried out, using an AlGaAs optical waveguide, to detect the interferometric autocorrelation trace of light from a mode-locked Nd³⁺:YAG laser. Both intensity and interferometric autocorrelation traces of pulses from a mode-locked Nd³⁺:YLF laser were then successfully obtained for the first time using the same device. The autocorrelation trace gives the full width at half maximum of the mode-locked pulses from the Nd³⁺:YLF laser to be approximately 17.7 ps.

The complete polarisation dependence of the two photon absorption coefficient, β , has been obtained by measuring the orientational dependence and the contrast ratio of the photocurrent in the device at an optical frequency far above that of the half-bandgap.

Measurements of the pulse width dependence of the two-photon absorption photocurrent in GaAs p-i-n waveguide photodetector using subpicosecond optical pulses at 1.5 μm are reported. For a fixed pulse energy, the photocurrent is observed to depend linearly on the inverse of the optical pulse width. A subnanosecond electrical response is also observed.

The propagation loss and the single photon absorption coefficients are measured as a function of wavelength in a device with an Al_{0.2}Ga_{0.8}As waveguide core. The propagation loss was as low as 1.37 cm⁻¹ at a wavelength of 904 nm. Using a photocurrent technique, band-to-band absorption was measured for photon energies well below that of the bandgap. It was demonstrated that, although the band-to-band absorption coefficient is small ($\sim 10^{-2}$ cm⁻¹ at a wavelength of 1 μm), it is responsible for reducing the contrast ratio of the waveguide autocorrelator.

Two-section lasers were fabricated in strained layer InGaAs/GaAs double quantum well material with intracavity saturable absorbers. Passive Q-switching was demonstrated in these lasers. Self-pulsation is seen at frequencies up to 12.5 GHz with a full width at half maximum of 20 ps.

Publications

Journal Publications

1. Mohammad M. Karkhanehchi, David A. Barrow, A. Catrina Bryce, Craig J. Hamilton and John H. Marsh, "The influence of single photon absorption on the performance of the two photon waveguide autocorrelator", *IEEE J. Quantum Electron.*, Vol. 33, No. 6, June 1997.
2. M. M. Karkhanehchi, C. J. Hamilton and J. H. Marsh, "Autocorrelation measurements of mode-locked Nd:YLF laser pulses using two photon absorption waveguide autocorrelator", *IEEE Photonics Tech. Lett.*, Vol. 9, No. 5, pp. 645-647, May 1997.
3. M. M. Karkhanehchi, J. H. Marsh and D. C. Hutchings, "The polarisation dependence of two-photon absorption in an AlGaAs waveguide autocorrelator", Submitted to *Applied Optics* 1997.
4. Z. Zheng, A. M. Weiner, J. H. Marsh and M. M. Karkhanehchi, "Ultrafast optical thresholding based on two-photon absorption GaAs waveguide photodetectors", *IEEE Photonics Tech. Lett.*, Vol. 9, No. 4, pp. 493-495, April 1997.

Conference Publications

1. David A. Barrow, Frances R. Laughton, Mohammad M. Karkhanehchi and John H. Marsh, "Two-photon absorption semiconductor waveguide autocorrelator for ultrashort pulse measurements", in *Conference on Lasers and Electro-Optics Europe (CLEO/Europe '94)*, Amsterdam, The Netherlands, Aug. 1994, paper CThM5.
2. Mohammad M. Karkhanehchi, David A. Barrow, A. Catrina Bryce and John H. Marsh, "The influence of single photon absorption on the performance of the two photon absorption waveguide autocorrelator", in *Semiconductor and Integrated Opto-Electronics Conference (SIOE'96)*, Cardiff, Wales, March 1996, paper 17.
3. Mohammad M. Karkhanehchi, David A. Barrow, A. Catrina Bryce and John H. Marsh, "The influence of single photon absorption on the performance of the two-photon absorption waveguide autocorrelator", in *LEOS'96, Inaugural meeting of the Scottish Chapter*, Glasgow University, Glasgow, Scotland, April 1996, poster 30.

4. M. M. Karkhanehchi, C. J. Hamilton and J. H. Marsh, "Nd:YLF laser pulse measurement using a semiconductor waveguide autocorrelator", in *LEOS'96, meeting of the Scottish Chapter*, Heriot-Watt University, Edinburgh, Scotland, Sep. 1996, poster 22.
5. M. M. Karkhanehchi, J. H. Marsh and D. C. Hutchings, "The polarisation dependence of the two-photon absorption coefficient in an AlGaAs waveguide autocorrelator", in *Conference on Lasers and Electro-Optics (CLEO)*, Baltimore, Maryland, U.S.A., May 1997, paper CFG5.
6. Z. Zheng, A. M. Weiner, J. H. Marsh and M. M. Karkhanehchi, "Two-photon absorption GaAs waveguide photodetectors for ultrafast optical thresholding", in *Conference on Lasers and Electro-Optics (CLEO)*, Baltimore, Maryland, U.S.A., May 1997, paper CTuS4.

Contents

Acknowledgements		i
Abstract		ii
Publications		iii
Contents		v
Chapter 1		
1.1	Introduction	1
1.2	Semiconductors	2
1.3	Quantum Wells	3
1.4	Strained Quantum Well Materials	8
1.5	Generation of Short Pulses in Semiconductor Laser	12
1.6	Ultra-Short Pulse Measurement Techniques	17
1.7	Outline of the Thesis	19
1.8	References	21
Chapter 2	Theory of Optical Properties of Semiconductors	
2.1	Introduction	25
2.2	The classical Non-linear Optics Theory	25
2.3	Nonlinearities in Optics	28
2.4	Semiconductor Bandgap Physics	29
2.4.1	Exciton Absorption	32
2.4.2	The Electric Field Effects	35
2.4.3	Refractive Index	36
2.4.4	Kramers-Kronig Relations	37
2.5	Linear Absorption in Bulk Semiconductors	38
2.6	Free Carrier Absorption	41
2.7	Two Photon Absorption	45
2.8	Conclusions	47
2.9	References	48

Chapter 3	Waveguide Design and Fabrication	
3.1	The Slab Waveguide	51
3.2	Three Dimensional Waveguide	54
3.3	Numerical Methods	55
3.3.1	Effective Index Method	55
3.3.2	Vector Finite Difference Method	57
3.4	Refractive Index of Bulk AlGaAs	57
3.5	Waveguide Design	59
3.6	Waveguide Structure	61
3.7	Photoluminescence Spectroscopy	62
3.8	Waveguide Fabrication	64
3.9	Conclusions	68
3.10	References	69
Chapter 4	Two Photon Absorption Waveguide Autocorrelator and Photodetector	
4.1	Introduction	70
4.2	The Structure of Ultra-short Pulses	71
4.3	Methods of Detection and Measurement	74
4.4	Autocorrelation Techniques	74
4.4.1	Linear Autocorrelation of Two Pulses	75
4.4.2	Non-linear Autocorrelation—Slow Correlation	77
4.4.3	Non-linear Interferometric Autocorrelation-Fast Correlation	79
4.4.4	Interferometric Correlation and Pulse Shape	80
4.5	Experiments	80
4.5.1	Nd ³⁺ :YAG Laser	81
4.5.2	Device Fabrication	81
4.5.3	Testing the Waveguides	82
4.5.4	Single Beam Measurements of a Nd ³⁺ :YAG Laser Pulses	84
4.5.5	Interferometric Autocorrelation of a Nd ³⁺ :YAG Laser Pulses	85

4.6	Autocorrelation Measurements of Nd³⁺:YLF Laser Pulses	87
4.6.1	Single Beam Measurements of a Nd ³⁺ :YLF Laser Pulses	88
4.6.2	Intensity Autocorrelation of a Nd ³⁺ :YLF Laser Pulses	89
4.6.3	Interferometric Autocorrelation of a Nd ³⁺ :YLF Laser Pulses	93
4.7	The Polarisation Dependence of Two Photon Absorption Coefficient in a Waveguide Autocorrelator	94
4.7.1	Introduction	94
4.7.2	Experiments	97
4.8	Ultra-fast Optical Thresholding based on Two-Photon Absorption GaAs Waveguide Photodetectors	101
4.8.1	Introduction	101
4.8.2	Waveguide Structure	102
4.8.3	Experiments	103
4.9	Conclusions	108
4.10	References	110

Chapter 5 The Influence of Single Photon Absorption on the Performance of the Two Photon Waveguide Autocorrelator

5.1	Introduction	114
5.2	Waveguides Fabrication	116
5.3	Theory of Fabry-Perot Technique	116
5.4	Experimental Set-up	120
5.5	Simulation of Waveguide Losses using F-Wave IV	124
5.6	Linear Absorption Photocurrent Measurements	128

5.7	Influence of Single Photon Absorption on the Contrast Ratio of the Waveguide Autocorrelator	132
5.8	Conclusions	134
5.9	References	136
Chapter 6	Two-Section Semiconductor Laser	
6.1	Introduction	138
6.2	Band Filling in Semiconductor Lasers	140
6.3	Two-section Q-switched Diode Laser	141
6.3.1	Active Q-switching	142
6.3.2	Passive Q-switching (Self-Pulsation)	143
6.3.2	Description of Self-Pulsating Behaviour	145
6.4	Device Fabrication	149
6.4.1	Material Structure	150
6.4.2	Fabrication Technique	151
6.5	Testing	157
6.5.1	Experimental Set-up	157
6.5.2	Device Characterisation	158
6.5.3	Optical Spectra	160
6.5.4	Testing the Devices under Self-Pulsation	161
6.5.5	Temporal Measurements	162
6.5.6	Streak Camera Results	163
6.5.7	The Effect of Reverse Bias on Self-Pulsation	164
6.5.8	CW Measurements	168
6.6	High Speed Material	171
6.6.1	Material Structure and Characterisation	171
6.6.2	Fabrication, Experiment and Results	172
6.7	Temperature Dependence of the Threshold Current	176
6.7.1	Introduction	176
6.7.2	Material, Experiment and Results	177
6.8	Conclusions	179
6.9	References	181

Chapter 7

7.1	Summary and Conclusions	185
7.2	Future Work	188
7.3	References	190

Chapter 1

1.1 Introduction

The quest for increasingly higher speeds and capacities in information transmission and information processing has strongly influenced the research effort into optoelectronic and photonic devices and their integration. Optoelectronic integration enables very large scale signal processing and electronic-light conversion to be combined on the same chip. The integration on single chips has the promise of great cost reduction, since much of the cost of producing circuits arises from the packaging and interconnection of the devices.

Optical integrated circuits represent one of the great research challenges in the optoelectronics field. Optical semiconductor devices have shown immense improvements over the last two decades, and the push for ever higher speed circuits at lower costs has been a major force behind the interest in optical integrated circuits.

Physical investigations in many branches of pure and applied scientific and technological research are now being carried out using ultra-short optical pulses (ULPs) [1-3]. 'Ultra-short' refers to a time interval in the range of picoseconds to femtoseconds.

Semiconductor lasers are important sources of short optical pulses. They are small in size, use electrical pumping, are easy to operate, and consequently short optical pulses can now be used in many applications that were previously unfeasible or uneconomical. Ultra short pulses are now being used in a wide range of fields such as high speed optical fiber communication systems, electrooptic sampling and impulse response testing of optical components.

It has been realised that ultra-short pulses can be used in a wide range of applications and their pulse shape—in amplitude and phase—can be fully determined in many cases [4].

The areas of application of ultra short pulses have multiplied and the means of producing such pulses have become more readily available. However, the instrumentation for measuring pulse widths and, what is more important, pulse shape and internal structure has not kept pace with the expansion of possible applications. Most effort has gone into modifying pulse structure using pulse compression techniques to approach the bandwidth limited 'ideal pulse'. The desire to produce ever shorter pulses may have overshadowed the need to investigate pulse structure more thoroughly.

This thesis examines both the generation and detection of ultra short pulse using some of the recent advances in semiconductor technology. The first part of the thesis describes the design, fabrication and characterisation of a particular optoelectronic device, namely the waveguide autocorrelator, followed by the measurements of ultra-short pulses using such a device. Then, the results of loss measurements in the waveguide are presented. The second part involves the generation of ultra short optical pulses using passively Q-switched two section semiconductor lasers.

1.2 Semiconductors

Many areas of the research into non-linear optical guided wave devices has been carried out in semiconductors, because of the potential benefits of monolithic integration with semiconductor lasers. Semiconductor growth and processing are now well understood and reproducible, and the GaAs/AlGaAs material system in particular has the great advantage that the aluminium fraction x can be altered without affecting the lattice constant of the $\text{Al}_x\text{Ga}_{1-x}\text{As}$ so much as to introduce significant strain at the GaAs interface. Altering x changes both the band gap and the refractive index of the $\text{Al}_x\text{Ga}_{1-x}\text{As}$ layer. Waveguiding occurs in a higher refractive index

material when it is surrounded by a material of lower refractive index, and so x can be tailored to produce the ideal refractive index difference between the layers which will confine the light optimally.

The other main semiconductor systems of major interest are indium based ternary or quaternary alloys which are used to make devices for long-haul optical communication, since the lowest signal dispersion and lowest loss windows of optical fiber lie at 1.3 and 1.55 μm , respectively.

Several non-linear optical devices have been demonstrated in bulk material, but recently most attention has been given to semiconductor Multiple Quantum Well (MQW) material. Therefore, the next section gives an introduction to quantum well structure and quantum well lasers, which are key elements for realisation of OEICs.

1.3 Quantum Wells

This section gives a brief introduction to a quantum well structure and lasers. For a more detailed treatment, the reader should refer to references 5 to 10.

A quantum well structure consists of one or more very thin layers of a relatively narrow bandgap semiconductor interleaved with layers of a wider bandgap semiconductor, for example GaAs for the narrow and AlGaAs for the wider bandgap semiconductor. If these narrow bandgap layers are thinner than the electron mean free path, the system enters into a quantum regime, in a manner analogous to the well known quantum mechanical problem of the particle in a box. The carriers (electron and holes) are confined to the narrow bandgap 'well' by larger bandgap 'barrier' layers. For infinitely high barriers, the magnitude of the wave function of the carriers must approach zero at the barrier wall because the probability of finding the particle within the wall is very small. The set of wave functions which satisfy these boundary conditions corresponds to only certain allowed states for the carriers. The carrier motion is thus quantised, with discrete allowed energies corresponding to the different wave functions.

Due to the quantisation of the wave functions in one direction (z direction, the growth direction of the epitaxial layer) in the well layer, the energy dependence of the density of state for electrons and holes changes to a staircase form. Figure 1.1 shows a quantum well energy bandgap structure with the quantised energy levels and the corresponding density of state $\rho(E)$ for quantum well and bulk materials.

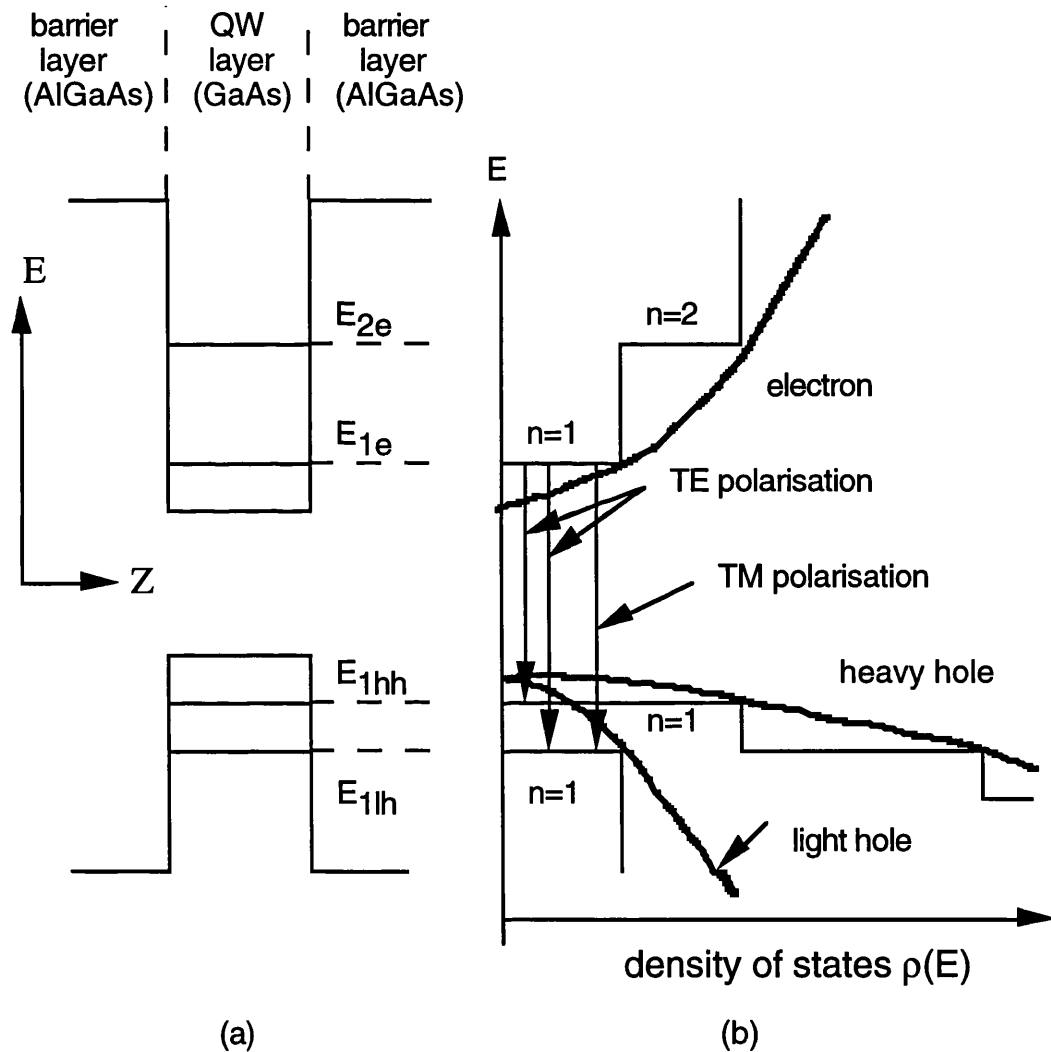


Figure 1.1: (a) Band structure for conduction and valence band with the quantum energy levels in a quantum well. E_{1e} and E_{2e} are $n=1$ and $n=2$ electron levels, and E_{1hh} and E_{1lh} are $n=1$ heavy hole and $n=1$ light hole levels, respectively. (b) Density of states as a function of energy for a QW structure (solid line) and for a bulk crystal (solid thick line) [after ref. 5].

In a bulk crystal where the layer thickness are larger than the carrier mean free path, the density of states is always parabolic and is equal to zero at the minimum energy (i.e. at band edge). In contrast, the staircase form of $\rho(E)$ in quantum well structures has a finite non-zero value of density of states even at the minimum energy. Furthermore, the form of the staircase can be tailored by changing the layer thicknesses of the structure, which change the energies of the confined states.

For most practical purposes quantum size effects are negligible for layers thicker than 20 nm. Therefore, the realisation of quantum well structures followed the advancement of crystal growth technology by molecular beam epitaxy (MBE) and metal organic chemical vapour deposition (MOCVD). These techniques are superior to liquid phase epitaxy (LPE) technology in preparing QW structures, in the reproducibility of samples with a given thickness of the active region and the degree of its spatial homogeneity.

Another remarkable feature of quantum well structures is the observation of room temperature excitons. From three dimensional (bulk) semiconductor physics, it is known that the absorption spectrum is not simply determined by the creation of a free electron and a free hole. The carriers are correlated in their motion in a way that can be described by the simple Coulomb attraction of the electron and the hole. They orbit around each other as in a hydrogen atom, with the hole acting as the proton. These bound states are known as excitons and, as their formation energy is less than that to excite an electron into the conduction band, exciton states can be thought of as existing within the forbidden energy gap. Excitons are seen as narrow lines in the absorption spectrum of a semiconductor, giving an enhancement in the continuum absorption, and situated just below the absorption edge. The increased absorption occurs because of the attraction between the electron and hole, so excitons also tend to disappear in the presence of a high concentration of free electrons and holes, which screens the excitons. Normally, excitons have such a short lifetime (their lifetime at room temperature in GaAs/AlGaAs QWs is about 400 fs) that their effects can only

be observed at cryogenic temperatures. In quantum wells, however, the confinement of carrier motion in wells whose thickness is smaller than the excitonic Bohr diameter (28 nm in GaAs) leads to an increase of the coulombic binding force, and consequently excitonic states become stable at room temperature [5, 9]. Excitons are not important for laser action since they are screened by the high level of carrier injection in the laser material. However, this exciton persistence at room temperature leads to effects such as the dc Quantum Confined Stark Effect (dc QCSE), which occurs when a dc electric field is applied to a MQW structure, and which has been used for electro-optic modulators [11]. In a similar way, the ac Quantum Confined Stark Effect (ac QCSE) occurs when an optical electric field is applied to a MQW structure, and has been shown to produce ultrafast all optical modulation (< 500 fs recovery time) in a GaAs/AlGaAs directional coupler [12]. The exciton and the QCSE will be discussed in more detail in Chapter 2.

A quantum well (QW) laser diode is a double heterostructure (DH) laser whose active layer is so thin that quantum size effects are present. The use of very thin active layers has several consequences for the laser operation [9]. Firstly, the photon generation occurs through carrier transitions between confined states in the conduction band and valence band. Therefore, lasing will occur at energies determined mainly by the band gap of the material and the confining energies of the QW states.

Due to the staircase density of states of quantum wells, the bottom of the conduction band and the top of the valence band have a finite density of states, whereas in a bulk DH the density of states is zero at minimum energy. This implies that in bulk lasers, the gain has to build up by carriers filling up the low density of states levels first before reaching high gain (high density of states) and the carriers at energies below that high gain level can make no useful contribution to lasing action. In QW lasers, carriers at the bottom of the conduction band and top of the valence band contribute to the gain at its peak. This effect contributes to the lower

transparency current density and to higher differential gain, i.e. gain per injected carrier, of QW lasers. However, the price paid is that gain will saturate at a given value when the electron and hole states of a given quantised energy level are fully inverted, whereas the gain in DH never saturates due to the filling of an ever increasing density of states. Nevertheless, the problem of low gain saturation can be overcome by the use of several wells, rather than only one, separated by barriers, forming a so—called multiple quantum well (MQW) structure. Quite obviously, MQW lasers have larger transparency current densities than single quantum well (SQW) lasers, but they offer higher differential gain and higher gain saturation. Therefore, MQW lasers are more suitable for high loss cavities.

In semiconductors, narrow bandgap materials generally have a larger refractive index, therefore a DH provides both optical and carrier confinement around the guiding active layer. The thin active layer improves carrier confinement by concentrating the carriers in a smaller volume and transparency is more easily reached, but, on the other hand, it reduces optical confinement of the lasing mode in the active region since the layer is too thin to work as an effective guiding layer. To overcome this problem, an extra guiding layer is introduced in the structure, in the so-called separate confinement heterostructure (SCH) or, if there are several intermediate layers, a graded-index separate confinement heterostructure (GRIN-SCH) [9]. The refractive index profiles of these structures are shown in Figure 1.2.

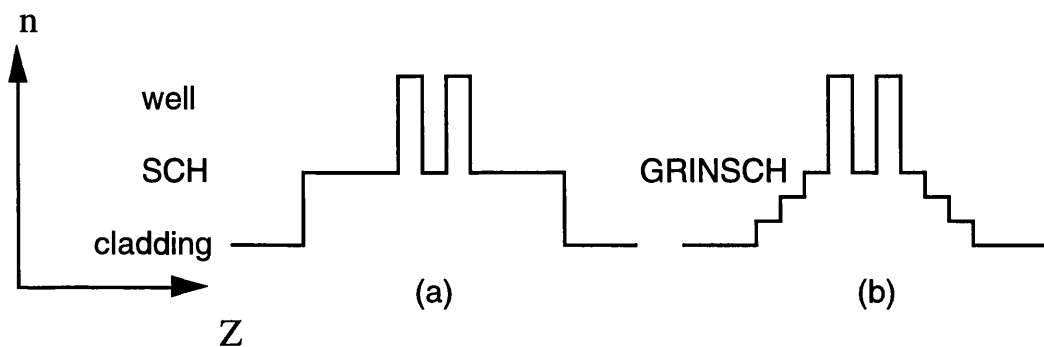


*Fig. 1.2: Refractive index profile of a DQW demonstrating
(a) SCH (b) GRINSCH*

1.4 Strained Quantum Well Material

An ideal semiconductor laser should have a band structure in which both the conduction and valence bands have low effective mass [13, 14]. In practice, conventional semiconductor lasers satisfy only one of these requirements. The conduction band has a low effective mass m_c but the valence band properties are dominated by the heavy hole band, where the effective mass m_h can be an order of magnitude larger than m_c . The high density of valence states increases the carrier density required for transparency and is primarily responsible for the two major loss mechanisms in long wavelength lasers, namely intervalence band absorption (IVBA) and Auger recombination. IVBA occurs when the photon is subsequently reabsorbed by lifting an electron from the spin-split-off band into an injected hole state in the heavy-hole band. This absorption loss contributes both to increasing the threshold current and to reducing the quantum efficiency above threshold. In Auger recombination, an electron and hole again recombine across the bandgap but now, instead of emitting a photon, excite a third carrier to higher energy.

A laser, in which the highest valence band has a low effective mass, should therefore have considerable advantages. The reduced hole effective mass allows the Bernard-Duraffourg condition ($E_{fc} - E_{fv} > E_c - E_v$) for transparency to be satisfied at a lower carrier density, improved efficiency and enhanced dynamic response and high speed performance [15-17]. Moreover the differential gain is enhanced due to the ease of penetration of the valence quasi-Fermi level into the band edge [15]. The low effective mass should also lead to the elimination of the two major loss mechanisms in long wavelength lasers, namely intervalence band absorption (IVBA) and Auger recombination, as they are both associated with holes at large wavevector k and the holes are now confined in a much smaller region of k space [13].

In a semiconductor laser with a strained active layer, the heavy hole and light hole band degeneracy at the bandgap is lifted. Under compressive strain, the heavy hole band is lifted above the light hole band and the bandgap increases whereas the opposite occurs when the active region is placed under tension. This results in TE and TM polarised emission for compressive and tensile strain respectively [10]. In addition, the heavy hole effective mass is reduced in the plane of the active region. By reducing the effective mass of the holes at the top of the valence band, or raising the light hole band above the heavy hole band, the idealised semiconductor band structure can be approached. For example, in conventional QW lasers, a two-or three fold increase in the modulation bandwidth is expected compared to ordinary double heterostructure (DH) lasers [18], and with strained QW layers the modulation bandwidth can be increased further by a factor of three [19].

It has also been shown that, as well as the addition of strain in the active region, an increase in the number of quantum wells and the addition of p-doping in the barriers can increase the modulation response [20, 21]. The differential gain is increased both by the addition of strained QW's and by an increase in the number of QW's. The addition of p-doping, on the other hand, has been proposed in order to further increase relaxation oscillation frequency by further enhancing differential gain [22]. The improvements in these properties basically result from the unsatisfied charge neutrality due to the modulation doped effect and from asymmetry in the density of states between the conduction and valence bands. In other words, it is due to the asymmetry of effective masses between electrons and heavy holes. The modulation- doped MQW (MD- MQW) structure is composed of a periodic structure with highly doped barrier layers and undoped well layers. The band edges of the conduction and valence bands are bent by the space charge, that is, ionised impurities in the barrier layers. The majority carriers from impurity atoms, that is majority holes from acceptors for the p- type case or majority electrons from donors for the n-type case, relax and become localised only in the well layers. However, the MD- MQW structure enables the utilisation of the effect of majority carriers in addition to the

quantum size effect. Therefore, the quasi- Fermi levels can be controlled by the impurity doping in the barrier layers. As a result, the gain and differential gain are enhanced or suppressed by the concentration and type of impurity in the barriers.

Recently, by improvements in both the MBE growth parameters and the doping sequence, a modulation bandwidth up to 40 GHz in undoped short cavity MQW lasers has been demonstrated [23].

So, it has been shown that the combination of strained multiple quantum wells, p-doping in the QW barriers and improvements in the growth parameters in the future appears to be the most promising route to maximise the bandwidth of semiconductor lasers [20, 23].

In summary, the advantages of QW lasers over conventional bulk DH lasers are briefly listed below [5, 9, 10]:

- *Lower threshold current density:* This is normally lower by a factor of around 3. As described above, this is due to thinner active region of QW lasers, which leads to a lower transparency current, higher differential gain and narrower bandwidth of optical gain as compared with DH lasers.

- *Threshold current density is less temperature sensitive:* QW lasers have a larger temperature coefficient T_0 than DH lasers. The reason for this is, as the density of states is modified, there are fewer energy states into which the carriers may be thermally scattered. Therefore, the thermal spreading of carriers is reduced in QW laser compare to bulk devices and so the devices are less temperature sensitive. GaAs QW lasers typically have T_0 in the range 180 to 250 K compared to 120-165 K for bulk. Values of T_0 for long-wavelength lasers are typically in the range $T_0 = 55 \pm 20$ K.

- *Polarisation dependent optical gain, which makes the laser oscillate in the TE mode:* In QW structure, a TE polarised optical wave whose electric vector lies in the plane of the QW layers can couple with both the electron-heavy hole transition and the

electron-light hole transition. The TM polarised optical wave whose electric vector is perpendicular to the plane of QW layer, on the other hand, can only couple with the latter transition (Fig. 1.1). Since the density of states of the heavy hole band is approximately 3 times larger than that of the light hole, the gain and consequently the laser emission from unstrained QW lasers is highly TE polarised. In bulk material the heavy and light hole states are degenerate, therefore, the DH laser gain is less polarisation selective. Although a Fabry- Perot laser will always oscillate TE because of the higher reflection coefficient for TE light, the QW polarisation advantage is important for DFB/DBR lasers. In this type of laser diode, there is no function provided for selecting polarisation, so that small perturbations such as changes in the ambient temperature make the oscillation unstable in polarisation.

- *Higher direct modulation frequency:* This may exceed 30 GHz, which is higher by factor of 3 than for DH lasers. This higher modulation speed comes from the higher differential gain of QW lasers, specially with strained MQW layers, as discussed before.

- *Higher stability in oscillation wavelength:* QW lasers have a narrower optical gain spectrum width, due to the stair density of states, than DH lasers, so that they oscillate more easily in a single longitudinal mode (single mode emission).

- *Reduced chirping:* Chirp is a temporal sweep of the lasing wavelength across the laser pulse, resulting from change of the refractive index due to modulation of the carrier density. This effect is reduced by a factor of up to 3 in QW lasers as compared with DH lasers due to the higher differential gain of QW lasers.

- *Higher reliability:* Reliability problems in semiconductor lasers come from catastrophic failure due to facet degradation and damage induced by high optical fields and recombination at the facet, and gradual degradation due to dark line defects which grow at higher current densities [10]. The thin active material compared with the thick

optical cavity in QW lasers reduces the effects that cause catastrophic failure and gradual degradation, improving the device reliability.

- *Easier monolithic integration:* QW structures are more suitable for applications in optoelectronic integrated circuits (OEICs) than bulk semiconductors. Due to their steeper absorption edge, QW can form lower loss passive waveguides for integration of a laser and an optical modulator for example, making use of the electric field effect on the excitons which improves the modulation characteristics. Electroabsorption in a QW structure close to the bandgap is dominated by the Quantum Confined Stark Effect (QCSE) [11]. Under zero external electric field the material is transparent so the light can pass with very little loss. When an external electric field is applied, the bandgap narrows so that the material becomes highly absorptive and the light is absorbed. Monolithic integration of QW lasers with photodetectors, amplifiers, modulators, switches and transistors has been realised [24, 25]. The monolithic integration of a laser and saturable absorber to form a Q-switched two section laser will be discussed in Chapter 6. Also, QW structures can be intermixed by compositional disordering, which changes their bandgap and refractive index. This technique can be very useful for the realisation of very low loss passive waveguides for OEICs, monolithic extended cavity lasers, low loss optical modulators and the fabrication of quantum wire and quantum dot lasers from quantum well material [5, 25, 26].

The reason for those characteristics is essentially the staircase density of states of quantum well structures, which is their most important feature.

1.5 Generation of Short Pulses in Semiconductor Laser

Practically from the moment of discovery of the laser effect in the early 1960s, much of the research in quantum electronics has been directed to generation of ultra-short optical pulses and their use in many branches of fundamental research as well as in practical applications.

Optical short pulses can be generated from semiconductor lasers by several means, including Q-switching, gain switching, and mode-locking [8, 27-30]. The basic principle of these techniques is to switch or modulate the gain or loss of the laser.

Q-switching works by modulation of the loss of the laser cavity. While the laser population inversion is building up, the switch is held off (in the high loss state), ensuring a low Q of the cavity and there is no laser emission. As the carrier density in the laser reaches its peak, the cavity is rapidly switched on (low loss state), to give a high Q condition and the stored energy is emitted in form of a intense optical pulse [27]. Q-switched lasers usually have two sections, a gain and a loss modulation section. If the loss modulation is provided by external electrical modulation it is called active Q-switching [27, 30]. If the loss modulation is caused by saturable absorption it is called passive Q-switching [12, 27, 31]. The loss modulator or saturable absorber region can be accomplished by reverse biasing a short segment in a split contact laser, for example. The reverse bias red shifts the semiconductor band edge, introducing loss. In the case of active Q-switching, a short electrical pulse is applied to the section, forward biasing it and opening a short time window of low loss in the cavity for the optical pulse being emitted. 15 ps pulses at 1 GHz repetition rate, with 4 pJ pulse energy were obtained with this scheme [30]. In the case of passive Q-switching, the saturation of the absorber opens the cavity for short pulse emission. Generation of pulses as short as 2 ps at 18 GHz repetition rate, with peak power above 10 W (50 pJ pulse energy) has been achieved with passive Q-switched lasers [32]. Lately, Portnoi, et.al. [33] have obtained high power optical pulses above 45 W from single heterostructure devices, but only at low repetition rates (10 s of kHz) due to power supply limitation. However, the pulse width and repetition rate are ultimately determined by carrier-photon interaction in the laser and are limited by the relaxation oscillation phenomenon [27]. The relaxation oscillation frequency is given by [8]:

$$f_r = \frac{1}{2\pi} \sqrt{\frac{Gp_0}{\tau_p}} \quad (1.1)$$

where G is the differential optical gain, p_0 is the photon density and τ_p is the photon lifetime in the laser cavity, given by [8]:

$$\tau_p = \frac{1}{v_g \left(\alpha + \frac{1}{L} \ln \sqrt{R_1 R_2} \right)} \quad (1.2)$$

where v_g is the group velocity of light, α is the loss of the cavity, L is the cavity length and R_1 and R_2 are the mirror reflectivities. The relaxation oscillation frequency also limits the speed of direct signal modulation of diode lasers [34]. Higher relaxation oscillation frequency of the laser allows shorter pulse generation at higher repetition rates. From the equations above, one can see that the maximum speed of the laser can be tailored by proper device design, including cavity configuration (reducing photon lifetime by using short cavities and anti-reflection coatings), semiconductor material design (increasing the differential gain by using MQW structures for example), and optimisation of pumping level (to increase the photon density) [27]. Also, reduction of parasitic capacitance and series resistance, which filters the high speed electrical signal, as well as the reduction of carrier transport time across the confinement heterostructure improves the laser speed [27, 34].

Due to the nature of Q-switching operation, which involves high carrier density modulation and high power pulse generation, Q-switched lasers have speed limitations. Pulse width and repetition rate also depend on device geometry (cavity length, gain section to absorber section length ratio), gain current and absorber reverse bias [27, 31, 32]. Therefore, these parameters can be used to tune the pulse width and repetition rate of the laser. Moreover, Q-switched pulses are also very chirped, which can be highly undesirable for some applications. For the Q-switched case, many of the longitudinal modes of the cavity are excited as consequence of the dynamic overshooting of carrier concentration. During the emission of such high

power optical pulses, the wavelength of each longitudinal mode is shifted due to the large variation of carrier concentration, and the spectral line of the mode is broadened. However, pulse compression techniques can be used to shorten these chirped pulses and obtain short transform limited pulses from them [27].

Gain switched lasers employ a DC current and a short electrical pulse current source to pump the laser. The DC current can bias the laser just below or above lasing threshold, whereas the large amplitude short electrical pulses (of the order of tens to hundreds of picoseconds) switch the gain on and off by modulating the carrier density in the cavity. This large carrier density modulation raises the gain well above lasing threshold, leading to high intensity laser emission, which in its turn, depletes the carrier density below lasing threshold, switching the laser off until the gain recovers and is raised again. Typically, this process can generate pulses of around 10 ps width (a few round trips) at around a few gigahertz repetition rate maximum, although pulses as short as 7 ps at 100 MHz repetition rate have been achieved [35].

The pulse energy of a gain switched laser is of order of 4 pJ giving about 0.3 W peak power for 13 ps pulse width [30]. The laser emits in a broad optical spectrum, since many longitudinal modes of the cavity are excited as consequence of the dynamic overshooting of carrier concentration. This means that gain switched pulses are highly chirped, i.e. far from being transform limited pulses [27, 36]. Also, gain switched lasers have similar speed limitations to Q switched lasers.

The mode-locking technique is also based on gain or loss modulation in the cavity, but differently from the previous cases, here the modulation is small and its period must be equal to (or multiples of) the round trip time of the cavity [28, 30]. It does not shut the cavity completely to allow the build up of a high gain and the emission of a high energy pulse. In mode-locked lasers, the modulation is just enough to synchronise the emission, or lock the phases, of the several longitudinal modes oscillating in the laser cavity. Constructive and destructive interference of these highly coherent longitudinal modes leads to pulse formation in the cavity. If an

external electrical signal provides gain modulation, the laser is actively mode-locked and this can be achieved by applying a fast electrical signal superimposed on the DC bias level of the gain section of the laser. Passively mode-locked lasing can be accomplished by incorporating a saturable absorber in the laser cavity, leading to internal loss modulation of the cavity. Hybrid mode-locking, which uses the saturable absorption effect to produce the optical pulse and external modulation to synchronise the pulse, can also be implemented.

Since the repetition rate of mode-locked pulses depends on cavity length (round trip time of the cavity), external cavity configurations lead to low repetition rates, typically in the megahertz range, and the short length of monolithic cavities, typically of the order of 500 μm , gives repetition rates of the order of tens to hundreds of gigahertz. Monolithic passively mode-locked lasers can generate subpicosecond pulses at hundreds and even thousands of gigahertz because the pulse shaping mechanisms are determined by the difference in transient saturation and recovery time constants between the gain and absorber. Therefore, in contrast to gain switched and Q-switched lasers, it is possible to generate short optical pulses with a repetition rate beyond the relaxation oscillation frequency of the laser [37]. Pulses as short as 0.61 ps at 350 GHz repetition rate have been achieved with a monolithic passive mode locked laser [37].

Mode locked pulses are usually low energy, ranging from 0.02 pJ to 1 pJ, giving peak powers within the tens to hundreds of milliwatts range [30]. Furthermore, due to the relatively low carrier density modulation in the laser and the low peak power emitted, the pulses generated by mode locked lasers are close to the Fourier transform limit, i. e. they have low levels of frequency chirp.

In summary, Q-switched and gain switched lasers can generate high power pulses, at a tuneable repetition rate in the range of hundreds of megahertz up to a few tens of gigahertz. The short pulses and high peak power provided by Q-switched semiconductor lasers are potentially useful in fibre optical systems. Other Q-switched

lasers (e.g. Q-switched Nd:YAG lasers) are useful for laser radar, cutting and drilling applications and basic scientific experiments, especially in non-linear optics. Pulse widths are of the order of 10 ps, however they are highly chirped. Mode locked lasers generate low energy pulses (about 100 times lower than in Q switched lasers), at a fixed repetition rate given by the cavity length of the laser (which can be about 100 times higher than the Q-switched ones). Pulse widths in the range of subpicosecond up to tens of picoseconds can be achieved, and they are high quality, nearly transform limited.

1.6 Ultra-Short Pulse Measurement Techniques

The accurate measurement and a reliable knowledge of the optical pulse structure is very essential in both basic research and applications of lasers.

All the techniques for determining the temporal profile $I(t)$ of a laser pulse can be generally classified into direct and indirect methods of diagnostics [38]. The direct method consists of measurements of $I(t)$ taken with a photodetector-oscilloscope combination or an electron-optical streak camera. The indirect method deals with the correlation functions of $I(t)$ of different orders [39]. One indirect method is based on the determining the second order autocorrelation function of $I(t)$ obtained by second harmonic generation (SHG) in a non-linear element (e.g. a waveguide autocorrelator) and, also, a modification of the conventional intensity autocorrelation technique, namely, the interferometric or fringe-resolved autocorrelation, which allows the exact pulse shape and pulse chirp to be determined. A combination of intensity autocorrelation, interferometric autocorrelation and optical spectrum allows the amplitude and phase of an optical pulse to be determined uniquely [40]. A novel technique, frequency-resolved optical gating (FROG), has also been developed for the direct determination of the fully intensity $I(t)$ and phase of a single ultra-short laser pulse [4]. This method involves splitting the pulse and overlapping the two resulting replicas $E(t)$ and $E(t-\tau)$ in an instantaneously responding non-linear optical medium. In this polarisation-gating arrangement, the probe pulse $E(t)$ passes through crossed

polarisers and is gated in the non-linear optical medium by the gate pulse $E(t-\tau)$. The signal pulse is then spectrally resolved, that is, its intensity is measured versus frequency and delay.

First the direct measurement technique is discussed. The simplest and most direct method of recording the temporal intensity profile of a laser pulse is provided by the photodetector-oscilloscope combination. This method has the advantage of being able to measure any pulse train without the need of a triggering source, however the main disadvantage of this technique is its time resolution. The time resolution is determined by the detection bandwidth of the detector and by the rise time of the sampling oscilloscope characteristics. High speed photodiodes or photoconductive detectors are often used in recording laser pulses. High speed photodiodes that have a rise time down to 9 ps (a detection bandwidth of 45 GHz) at all of the most important wavelengths of 0.85, 1.3, and 1.5 μm are commercially available at present [41]. Sampling oscilloscopes that are presently available have a typical bandwidth of 50 GHz. Recent developments in high speed metal-semiconductor-metal (MSM) photodetectors have shown usable electrical bandwidth in excess of 100 GHz, along with high efficiencies [42].

The photodiode-pulse sampling technique has been used to examine the self-pulsating frequency of two section lasers in Chapter 6. The time resolution of the system was too large to measure the pulse width of individual pulses accurately, the photodiode had bandwidth of 18 GHz and the sampling head's bandwidth was 50 GHz which gave a total rise time of about 30 ps. By using the fastest commercial devices, however, direct pulse measurements down to a time resolution of about 10 to 20 ps can be readily achieved with the use of the photodetector-sampling oscilloscope combination.

If a better time resolution is required, electron-optical streak cameras may be used. The method of studying rapidly varying luminous phenomena by electron-optical chronography was proposed by Zavoiskii and Fanchenko [43, 44]. Streak

cameras have the advantages of (1) the ability to determine directly the profile of optical pulses with picosecond and subpicosecond time resolution, (2) the capability for two dimensional analysis, such as time-resolved spectroscopy, i. e. time variation of the incident light with respect to wavelength, and (3) wide spectral range, from X-rays to the near-infrared region. One problem the streak camera has with measuring semiconductor laser pulses is the low sensitivity the streak tubes have when operating at 1.3 and 1.5 μm wavelengths [45]. Although streak cameras are versatile tools capable of measuring diode laser pulses with a subpicosecond time resolution, they are quite expensive, so indirect techniques for laser pulse diagnostics have been developed. These techniques are simple and inexpensive with a considerable practical advantages over the methods described above. They provide an extremely high time resolution down to tens of femtoseconds. The indirect techniques will be described in Chapter 4.

1.7 Outline of the Thesis

This thesis is organised as follows: the next chapter, chapter two, provides the theoretical background to the optical properties of semiconductor materials. Chapter three describes the process involved in design and fabricating the waveguides used in this work, starting from the waveguide theory and numerical methods necessary to design the structure. Chapter four describes the indirect pulse width measurement techniques, i.e. intensity and interferometric autocorrelation. First, intensity and interferometric trace of mode-locked Nd^{+3} :YAG laser pulses are given, and afterwards autocorrelation measurements of the mode-locked Nd^{+3} :YLF laser pulses are discussed. The results and discussion of optical loss and single photon absorption measurements in a p-i-n waveguide, followed by a discussion of the influence of single photon absorption on the contrast ratio of the two photon absorption waveguide autocorrelator are documented in chapter five. Chapter six contains a brief theoretical background of Q-switching and the device fabrication details of a passively

Q switched two section laser, followed by the results and discussion. Finally, Chapter seven summarises the content and the results of this thesis.

1.8 References

- [1] A. Miller and W. Sibbett, "A perspective on ultra-fast phenomena", *J. Modern Optics*, Vol. 35, pp. 1871-1890, 1988.
- [2] G. H. C. New, "The generation of ultra short pulses", *Reports on Progress in Physics*, Vol. 46, pp. 877-971, 1983.
- [3] A. J. Demaria, "Picosecond laser pulses", *Proc. IEEE J. Quantum Electron.*, Vol. 57, pp. 2-25, 1969.
- [4] R. Trebino and D. Kane, "Using phase retrieval to measure the intensity and phase of ultra-short pulses: Frequency-resolved optical gating", *J. of the Optical Society of America A*, Vol. 10, pp. 1101-1111, 1993.
- [5] H. Okamoto, "Semiconductor quantum well structure for optoelectronics-Recent advances and future prospects", *Jap. J. Appl. Phys.*, Vol. 26, pp. 315-330, Mar. 1987.
- [6] L. Esaki, "A bird's-eye view on the evolution of semiconductor superlattices and quantum wells", *IEEE J. Quantum Electron.*, Vol. 22, pp. 1611-1624, Sep. 1986.
- [7] W. T. Tsang, "Quantum Confinement Heterostructure Semiconductor lasers" *Semiconductors and Semimetals*, Vol. 24, Editor Raymond Dingle, Academic Press, 1987, Chapter 7.
- [8] A. Yariv, "Quantum Electronics", 3rd edition, Wiley, 1989.
- [9] C. Weisbuch and B. Vinter, "Quantum Semiconductor Structures: fundamentals and applications", Academic Press, 1991.
- [10] P. S. Zory, Jr. (Editor), "Quantum Well Lasers", *Quantum Electronics: principles and applications series*, Academic Press, 1993.
- [11] D. A. B. Miller, D. S. Chemla, T. C. Damen, A. C. Gossard, W. Wiegmann, T. H. Wood, C. A. Burrus, "Band-edge absorption in quantum well structures: The Quantum Confined Stark Effect", *Phys. Rev. Lett.*, Vol. 53, pp. 2173-2176, 1984.
- [12] R. Jin, J. P. Sokoloff, P. A. Harten, C. L. Chuang, S. G. Lee, M. Warren, H. M. Gibbs, N. Peyghambarian, J. N. Polky and G. A. Pubanz, "Ultrafast modulation

with subpicosecond recovery time in a GaAs/AlGaAs nonlinear directional coupler", *Appl. Phys. Lett.*, Vol. 56, p. 993, 1990.

[13] A. R. Adams, "Band structure engineering for low-threshold high efficiency semiconductor lasers", *Electro. Lett.*, Vol. 22, pp. 249-250, 1986.

[14] E. Yablonovitch and E. O. Kane, "Reduction of lasing threshold current density by the lowering of valence band effective mass", *J. Lightwave Tech.* Vol. 4, pp. 504-506, 1986.

[15] I. Suemune, L. A. Coldren, M. Yamanishi, and Y. Kan, "Extremely wide modulation bandwidth in a low threshold current strained QW laser", *Appl. Phys. Lett.*, Vol. 53, pp. 1378-1380, 1988.

[16] A. Ghiti, E. P. O'Reilly, and A. R. Adams, "Improved dynamics and linewidth enhancement factor in strained-layer lasers", *Electron. Lett.*, Vol. 25, pp. 821-823, 1989.

[17] K. Y. Lau, S. Xin, W. I. Wang, N. Bar-Chaim, and M. Mittelstein, "Enhancement of modulation bandwidth in InGaAs strained-layer single quantum well lasers", *Appl. Phys. Lett.*, Vol. 55, pp. 1173-1175, 1989.

[18] y. Arakawa, K. Valhala, and A. Yariv, "Quantum noise and dynamics in quantum well and quantum wire lasers", *Appl. Phys. Lett.*, Vol. 45, pp. 950-952, 1984.

[19] L. F. Lester, S. D. Offsey, B. K. Ridley, W. J. Schaff, B. A. Foreman, and L. F. Eastman, "Comparison of the theoretical and experimental differential gain in strained layer InGaAs/GaAs quantum well lasers", *Appl. Phys. Lett.*, Vol. 59, pp. 1162-1164, 1991.

[20] J. D. Ralston, S. Weisser, I. Esquivias, E. C. Larkins, J. Rosenzweig, P. J. Tasker, and J. Fleissner, "Control of differential gain, and damping factor for high speed application of GaAs-based MQW lasers", *IEEE J. Quantum Electron.*, Vol. 29, pp. 1648-1659, 1993.

[21] K. Y. Lau, Ch. Harder, and A. Yariv, "Direct amplitude modulation of short cavity GaAs lasers up to X-band frequencies", *Appl. Phys. Lett.*, Vol. 43, pp. 1-3, 1993.

[22] K. Uomi, "Modulation-doped multi-quantum well (MD-MQW) lasers", *Jap. J. Appl. Phys.*, Vol. 29, pp. 81-87, 1990.

- [23] S. Weisser, E. C. Larkins, K. Czotscher, W. Benz, J. Daleiden, I. Esquivias, J. Fleissner, J. D. Ralston, B. Romero, R. E. Sah, A. Schönfelder, and J. Roseenzweig, "Damping-limited modulation bandwidths up to 40 GHz in -undoped short-cavity $\text{In}_{0.35}\text{Ga}_{0.65}\text{As}$ -GaAs multiple-quantum-well lasers", *IEEE Photon. Tech. Lett.*, Vol. 8, pp. 608-610, 1996.
- [24] R. G. Hunsperger, "Integrated Optics: Theory and Technology", Third Edition, Optical Sciences Series, Springer-Verlag, 1991.
- [25] R. M. De La Rue and J. H. Marsh, "Integration technologies for III-V semiconductor optoelectronics based on quantum well waveguides", in *Integrated optics and Optoelectronics*, K. K. Wong and M. Razeghi, Eds. Los Angeles, CA:SPIE (Int. Soc. Opt. Eng.), pp. 259-288, Jan. 1993.
- [26] I. Gontijo, T. Krauss, J. H. Marsh, and R. M. De La Rue, "Postgrowth control of GaAs/AlGaAs quantum well shapes by impurity free vacancy diffusion", *IEEE J. Quantum Electron.*, Vol. 30, pp. 1189-1195, May 1994.
- [27] P. P. Vasil'ev, "Ultrashort pulse generation in diode lasers", *Optical and Quantum Electron.*, Vol. 24, pp. 801-824, 1992.
- [28] A. E. Siegman, "Lasers", Oxford University Press, 1986.
- [29] P. P. Vasil'ev, "Ultrafast Diode Lasers: Fundamentals and Applications", Artech House Publishers, 1995.
- [30] D. J. Derickson, R. J. Helkey, A. Mar, J. R. Karin, J. G. Wasserbauer and J. E. Bowers, "Short pulse generation using multisegment mode-locked semiconductor lasers", *IEEE J. Quantum Electron.*, Vol. 28, pp. 2186-2202, Oct. 1992.
- [31] D. A. Barrow, J. H. Marsh and E. L. Portnoi, "Q-switching pulses at 16 GHz from two section semiconductor lasers", in *CLEO/Europe*, Amsterdam, The Netherlands, paper CTuE4, pp. 75-76, Aug. 1994.
- [32] P. P. Vasil'ev, "Picosecond injection laser: A new technique for ultrafast Q-switching", *IEEE J. Quantum Electron.*, Vol. 12, pp. 2386-2391, Dec. 1988.
- [33] E. L. Portnoi, G. B. Venus, A. A. Khazan, I. M. Gadjiev, A. Y. Shmarcev, J. Frahm, and D. Kuhl, "Super high power picosecond optical pulses from Q-switched diode laser", in *15th IEEE International Semiconductor Laser Conference*, Haifa, Israel, paper Ch 90, pp. 157-158, Oct. 1996.

- [34] R. Nagarajan, D. Tauber and J. E. Bowers, "High speed semiconductor lasers", Intern. J. High Speed Electron. and Systems, Vol. 5, pp. 1-44, 1994.
- [35] H. F. Liu, M. Fukazawa, Y. Kawai and T. Kamiya, "Gain-switched picosecond pulse (10 ps) generation from $1.3 \mu\text{m}$ InGaAsP laser diodes", IEEE J. Quantum Electron. Vol. 25, pp. 1417-1425, June 1989.
- [36] M. Osinski and M. J. Adams, "Picosecond pulse analysis of gain switched $1.55 \mu\text{m}$ InGaAsP lasers" IEEE J. Quantum Electron., Vol. 21, pp. 1929-1936, Dec. 1985.
- [37] Y. K. Chen and C. W. Ming, "Monolithic colliding pulse mode-locked quantum well lasers", IEEE J. Quantum Electron., Vol. 28, pp. 2177-2185, Oct. 1992.
- [38] D. J. Bradley, and G. H. C. New, "Ultrashort pulse measurements", IEEE Proc., Vol. 62, pp. 313-345, 1974.
- [39] E. P. Ippen, and C. V. Shank, "Techniques for measurements", Ultra-short Light Pulses, S. L. Shapiro, Ed., New York: Springer, pp. 83-122, 1977.
- [40] K. Naganuma, K. Mogi, and H. Yamada, "General method for ultra-short light pulse chirp measurement", IEEE J. Quantum Electron., Vol. 25, pp. 1225-1233, 1989.
- [41] Photodiodes Catalogue, CA: New Focus, Inc.
- [42] Y. Chen, S. Williamson, T. Brock, F. W. Smith, and A. R. Calawa, "375-GHz bandwidth photoconductive detector" Appl. Phys. Lett., Vol. 59, pp. 1984-1986, 1991.
- [43] E. K. Zavoiskii, S. D. Fanchenko, "Physical fundamental of electron-optical chronography", Soviet Physics-Doklady, Vol. 1, pp. 285-288, 1956.
- [44] E. K. Zavoiskii, S. D. Fanchenko, "Image converter high speed photography with 10^{-9} to 10^{-14} sec. time resolution", Appl. Optics, Vol. 4, pp. 1155-1167, 1965.
- [45] Hamamatsu Photonics K. K., "Universal Streak Camera C5680", specification catalogue, 1994.

Chapter 2

Theory of Optical Properties of Semiconductors

2.1 Introduction

It is almost four decades since the invention of the laser sparked off a renewed interest in optical physics. Optics is playing an ever-increasing role in telecommunications systems due to the high potential bandwidth. As communication speeds increase, conventional electronic devices are not fast enough to respond and alternative devices must be found. One promising approach is to utilise non-linear optics to do the signal processing.

Interaction of light with matter is usually characterised by several phenomena, such as light absorption, refraction, scattering and luminescence. All of these were regarded as properties of a material dependent on wavelength, but independent of light intensity. The invention of the laser allowed the production of previously unobtainable light intensities. The high intensities are such that the electro-magnetic field of the light can alter the optical properties of matter. Thus, the characteristic optical properties of a material also become a function of intensity. The study of these properties is known as *Non-linear Optics*.

2.2 The classical Non-linear Optics Theory

It is necessary first to establish some definitions pertaining to the non-linear properties of optical materials. On applying an electric field in an insulating dielectric medium, the positive and negative charge distributions in the material are displaced in opposite directions and a dipole moment is induced. The dipole moment per unit volume, or polarisation, P , is proportional to a small applied field $E(\omega, k)$ of frequency ω and wavevector k and can be expressed as:

$$P = \epsilon_0 \chi^{(1)} E(\omega, k) \quad (2.1)$$

where ϵ_0 is the permittivity of a vacuum, $\chi^{(1)}$ is the linear susceptibility of the material, and E is the applied electric field. The linear susceptibility is related to the linear refractive index through:

$$n = \sqrt{\text{Re}(1 + \chi_{\omega}^{(1)})} \quad (2.2)$$

and the imaginary part of the linear susceptibility, $\chi^{(1)}$, corresponds to linear absorption.

When the optical field driving the dipole is sinusoidal, therefore, for small incident fields, the induced polarisation varies similarly. However, by using an intense optical field and overdriving the dipoles, it is possible to obtain a non-sinusoidally varying polarisation. When this is the case, higher optical harmonics are introduced in the polarisation field produced by the oscillating dipoles. The energy of the incident electric field has therefore been coupled to fields of different frequency by the non-linear response of the dipoles. Under these conditions, equation 2.1 is no longer valid and has to be modified to include the higher frequency terms. The equation can then be rewritten as:

$$P = \epsilon_0 \left(\chi^{(1)} E_{(\omega, k)} + \chi^{(2)} E_{(\omega, k)}^2 + \chi^{(3)} E_{(\omega, k)}^3 + \dots \right) \quad (2.3)$$

where $\chi^{(2)}$ and $\chi^{(3)}$ are the second—and third—order non-linear susceptibilities. There are many non-linear optical effects which have been observed in many different materials, and their strengths in each material are determined by the values of each non-linear susceptibility $\chi^{(n)}$. Because the non-linear susceptibilities $\chi^{(2)}$, $\chi^{(3)}$, etc. are much smaller than their counterpart $\chi^{(1)}$, non-linear effects are not seen unless laser light is used. In order to observe a non-linear response, an optical electric field is needed of the order of 1 kV/cm, corresponding to an intensity of about 2.5 kW/cm², to compensate for the small non-linear susceptibility [1], and this intensity is generally only obtainable from lasers.

The second term in equation 2.3 represents a second order effect. This is responsible for second harmonic generation, optical rectification and optical parametric generation, and the Pockel's electro-optic effect [2]. As a result of its E^2 dependence, second order nonlinearities only exist for materials which are non-centrosymmetric and non-crystalline materials such as glasses, liquids and gases [1].

When an electric field is applied to a symmetrical molecule, a polarisation is induced in the same direction as the applied field. If the field direction is now reversed the polarisation is also reversed and, because the crystal is centrosymmetric, the magnitude of the polarisation must be the same in both directions (i.e. $P(E) = -P(-E)$). From equation 2.3 it is clear that the only way for this to hold true is if $\chi^{(2)} = 0$.

In a non-linear medium with non-zero $\chi^{(2)}$, the frequency of the light beam mixes with itself due to the nonlinearity. Because of this, as well as a strong component in the polarisation at frequency ω , there are also two other weaker components induced, one at frequency 2ω and the other DC. This is the mechanism for second harmonic generation ($\omega + \omega = 2\omega$) and optical rectification ($\omega - \omega = 0$). When an optical input, at frequency ω , is combined with a DC electric field the second-order susceptibility also gives rise to the electro-optic effect ($\omega + 0 = \omega$). Note that in all cases energy conservation:

$$\hbar\omega = \hbar\omega_1 + \hbar\omega_2 + \dots \quad (2.4)$$

and momentum conservation (called phase-matching):

$$\hbar k_1 + \hbar k_2 + \dots = 0 \quad (2.5)$$

must be observed.

The third-order non-linear susceptibility, $\chi^{(3)}$, is non-zero for all materials. This term is responsible for third-harmonic generation, four-wave mixing, optical phase conjugation, the Kerr electro-optic effect, two photon absorption (which is of

particular relevance to the subject matter of this thesis), the Raman effect and the intensity-dependent refractive index change [2, 3]. Again, the real part is associated with refraction and the imaginary part with absorption, but now these are non-linear contributions.

When the third-order susceptibility is included in the expansion for the polarisation, the refractive index of the medium becomes intensity dependent and is given by:

$$n = n_0 + n_2 I \quad (2.6)$$

where n_0 is the linear refractive index, I is the intensity of the incident light and n_2 is the non-linear refractive index which is defined as [4]:

$$n_2(\text{S. I.}) = \frac{\chi^{(3)}}{2cn_0^2\epsilon_0} \quad (2.7)$$

where c is the velocity of light and ϵ_0 is the permittivity of free space, both in S.I. units. So if a material has a non-zero third-order susceptibility, there will be a change in the refractive index under the application of intense light. The value of n_2 is often quoted instead of $\chi^{(3)}$ when qualifying third order nonlinearities in materials.

2.3 Nonlinearities in Optics

Optical nonlinearities in semiconductors generally fall into one of two categories: resonant and nonresonant. When photons of energy close to, or larger than the band gap are incident on a semiconductor, a photoexcited carrier population is induced. The presence of these carriers modifies the dielectric constant and consequently alters the material's refractive index. Carrier effects tend to be resonant because of their dependence on the photon energy of the incident radiation. For this reason, the carrier effects are described as resonant effects. Examples of resonant nonlinearities are band filling [5], plasma effects [6], and optothermal effects [7].

Because resonant effects depend on carrier population density, the relaxation time of the nonlinearity is determined by the relaxation time of the excited carriers, which is normally in the region of at least nanoseconds. Nonresonant optical nonlinearities are in general much smaller than resonant ones, however they are less wavelength sensitive (the wavelength of the input light does not correspond to an optical resonance of the material). Their main advantage is that they are directly due to the incident optical field, and hence their effects are essentially instantaneous.

It should be mentioned that the nature of the laser excitation and the relaxation time of the nonlinearity play an important role in determining the character of the nonlinear effect. Assuming that the non-linear material is subjected to a pulsed laser source, if the relaxation time of the nonlinearity is larger than the pulse width, then the effect is integrated over the duration of the pulse so that the size of the net effect depends on the energy of the pulse. If, however, the relaxation time of the nonlinearity is much less than the pulse width, then the effect is proportional to the instantaneous intensity of the pulse. It is thus possible to make a distinction between energy dependent and intensity dependent effects.

2.4 Semiconductor Bandgap Physics

Semiconductor materials are characterised by having a continuum of valence band states separated from a conduction band continuum at an energy gap [8]. For many semiconductors the energy gap is of the order of 1.5—2 eV i. e. optical photon energies, thus allowing optical excitation of electrons from valence to conduction bands. Electrons excited into a conduction band decay rapidly to the bottom of the conduction band. This process, known as intraband relaxation, occurs typically on a time scale of 10 fs—100 ps. Decay from the conduction band to the valence band, known as interband relaxation, takes longer, typically 100 ps—1 μ s.

We consider transitions in which an electron is excited from the valence band to the conduction band with absorption of a photon of energy approximately equal to

ΔE , the energy of the forbidden gap. Such absorption is called the fundamental absorption. Here we must distinguish two types of transition, those involving only one photon and those involving also lattice energy in the form of phonons. Transitions involving no phonons we call *direct* transitions, shown in Fig. 2.1, and those involving phonons *indirect* transitions, Fig. 2.2.

In direct semiconductors, such as GaAs, the bottom of the conduction band lies at the same k value as the top of the valence band. This means that the momentum of the electron in the initial energy state is equal to that in the final energy state, and so both energy and momentum are conserved when a photon excites an electron from the valence to the conduction band.

For indirect semiconductors, such as Si and Ge, the momentum of the electron in the initial energy state is not equal to that in the final energy state, and so compensating momentum must be provided in order that momentum is conserved in the transition. This compensating momentum cannot be provided by photons, because the photon momentum is negligible at wavelengths around the absorption edge. It must therefore be provided by another source, for example phonons. Thus, in order for a transition to take place in an indirect semiconductor, a phonon must be either absorbed or emitted when the photon is absorbed. Absorption and emission of photons in indirect semiconductors is therefore a three-particle process, and so the probability of its occurrence is reduced. Phonons are quantized lattice vibrations in solids. They are the dominant scattering mechanism at room temperature but their effect decreases as the temperature is lowered, until impurity scattering takes over. The motion of the lattice ions due to phonons induces electric (and magnetic) field fluctuations that affect the motion of the electrons and scatter them.

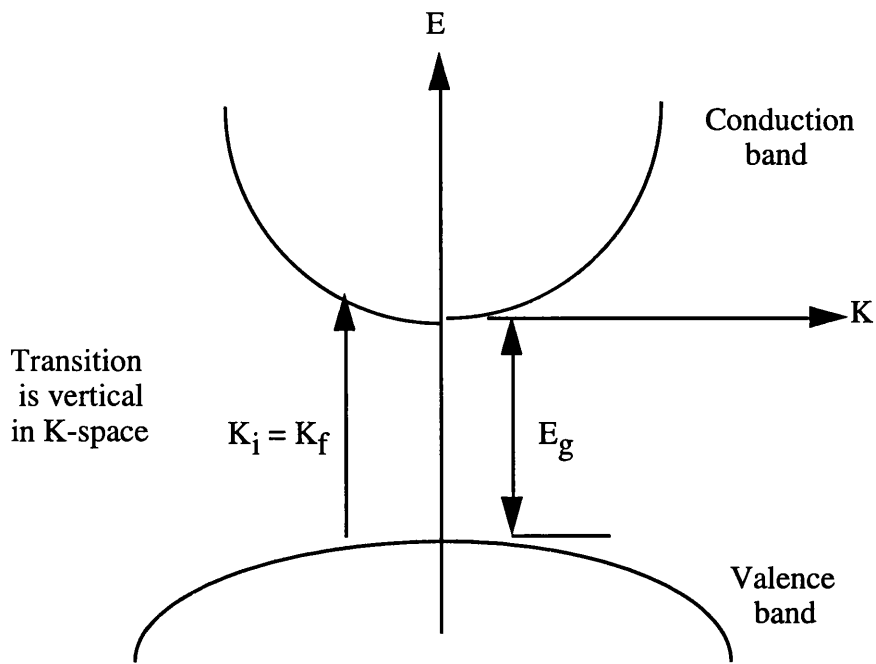


Fig. 2.1: The E-K diagram for direct transitions

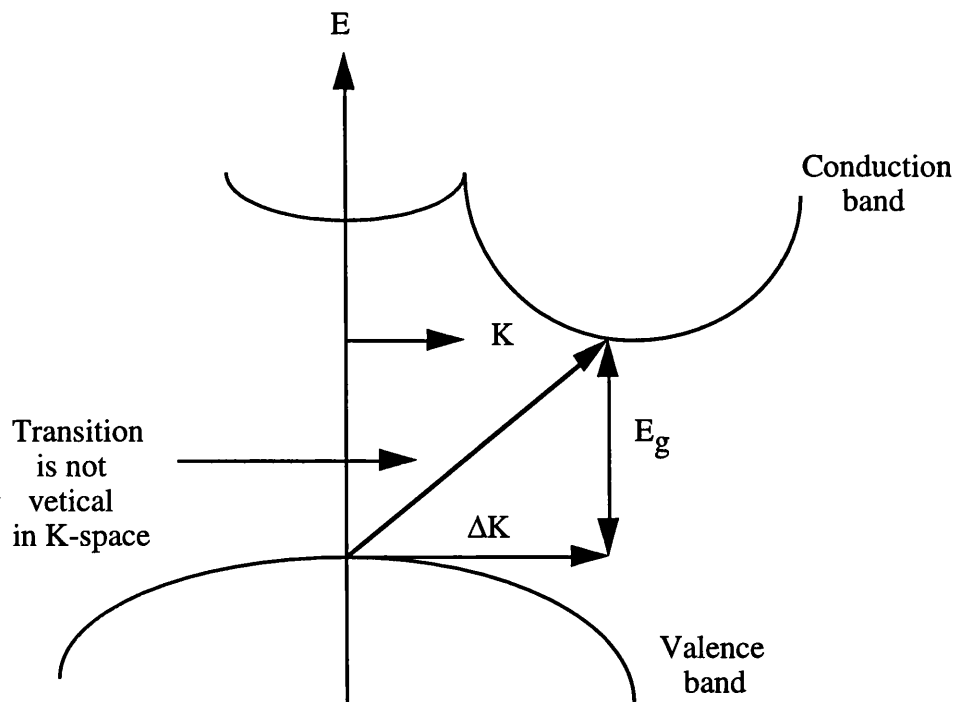


Fig. 2.2: The E-K diagram for indirect transitions

2.4.1 Exciton Absorption

An electron may combine with a hole to form a hydrogen-like state, known as an exciton. Excitons are unstable with respect to radiative recombination in which the electron drops into the hole in the valence band, accompanied by the emission of a photon. The threshold energy for creating an exciton is $\hbar\omega < E_g$ in a direct bandgap semiconductor. In bulk material, the ground state excitonic binding energy, R_{3D} , and Bohr radius a_{3D} are given in S.I. units by [3]:

$$R_{3D} = \frac{e^4 \mu_r}{2\epsilon_0^2 \hbar^2} \quad (2.8)$$

$$a_{3D} = \frac{\epsilon_0 \hbar^2}{\mu_r e^2} \quad (2.9)$$

where $\hbar = h/2\pi$ (h is Planck's constant), e is the electron charge, ϵ_0 is the dielectric constant and μ_r is the reduced electron-hole mass, defined as:

$$\frac{1}{\mu_r} = \frac{1}{m_e} + \frac{1}{m_h} \quad (2.10)$$

where m_e and m_h are the electron and hole masses, respectively. There is an infinite series of energy levels for the exciton, just as for the hydrogen atom, and the energy of the n_{th} level is given by:

$$E_n^{3D} = E_g - \frac{R_{3D}}{n^2} \quad (2.11)$$

where E_g is the bandgap energy and n is an integer. For GaAs the binding energy of the ground state and the Bohr radius are 4.2 meV and 14 nm respectively[9]. At low temperature, excitons usually have energies just below the bandgap energy (Fig. 2.3). At room temperature, however, the linewidth of excitons is broadened by the large concentration of phonons and the exciton levels merge into the continuum absorption spectrum. As a result, the absorption spectrum from excitons can hardly be separated from the continuum absorption spectrum and is not seen at room temperature. Excitons also tend to disappear in the presence of a high concentration of

free electrons and holes, which screen the excitons. The effect of screening is thus to 'ionise' the exciton, causing the sharp resonance lines in the absorption spectrum to vanish and so produce a large optical nonlinearity. This will occur when the screening length is comparable to the Bohr radius a_{3D} exciton (about 14 nm for Gallium Arsenide at room temperature).

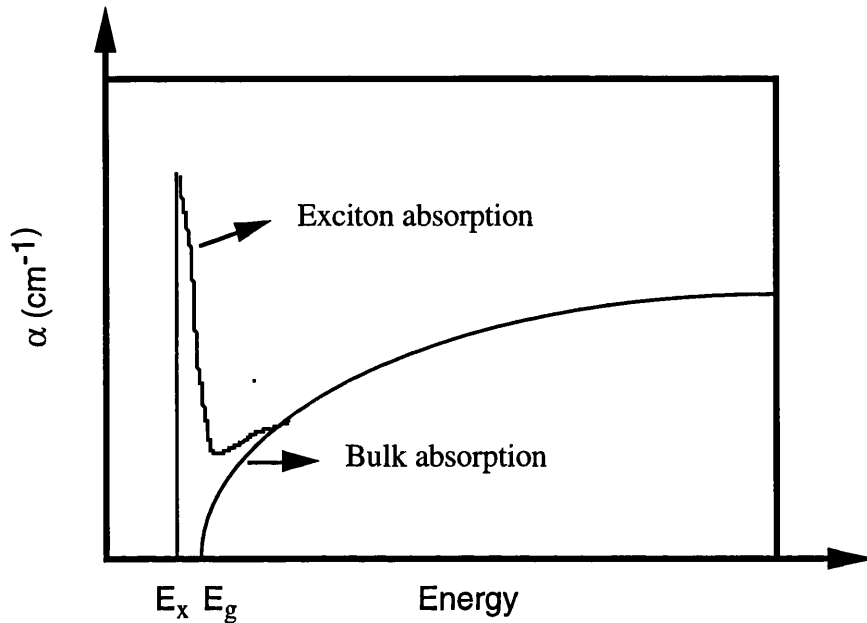


Fig. 2 3: The absorption edge spectrum of GaAs including exciton effects and the bulk (3D) density of state at low temperature (after ref. [10]).

Photons can also be absorbed by QWs, and electrons are excited from the valence band to the conduction band, just as for bulk material, except for the condition that transition can only take place between discrete energy levels with equal quantum numbers 'n'. Because the lowest conduction level lies above the level of the bottom of the bulk conduction band and the highest valence level lies below the level of the top of the bulk valence band, the effective bandgap of the QW structure is greater than that of bulk.

Fig. 2.4 shows the density of states spectra for bulk and QW material. The bulk density of states varies as $(E - E_g)^{1/2}$ [11]. The QW density of states in the direction perpendicular to the plane of the wells is a staircase shape, due to the quantisation of

the energy levels. It can be seen that, as the well width increases, the QW energy levels become closer together, so that the density of states spectrum approaches that of the 3D case. Similarly, as the well width becomes smaller, the QW energy levels become further apart, so that the density of states spectrum approaches that of the 2D case, which is $n_{2D}(E) = m/\pi\hbar^2$ [12]. This is a constant for $E > 0$, and the band edge is a step.

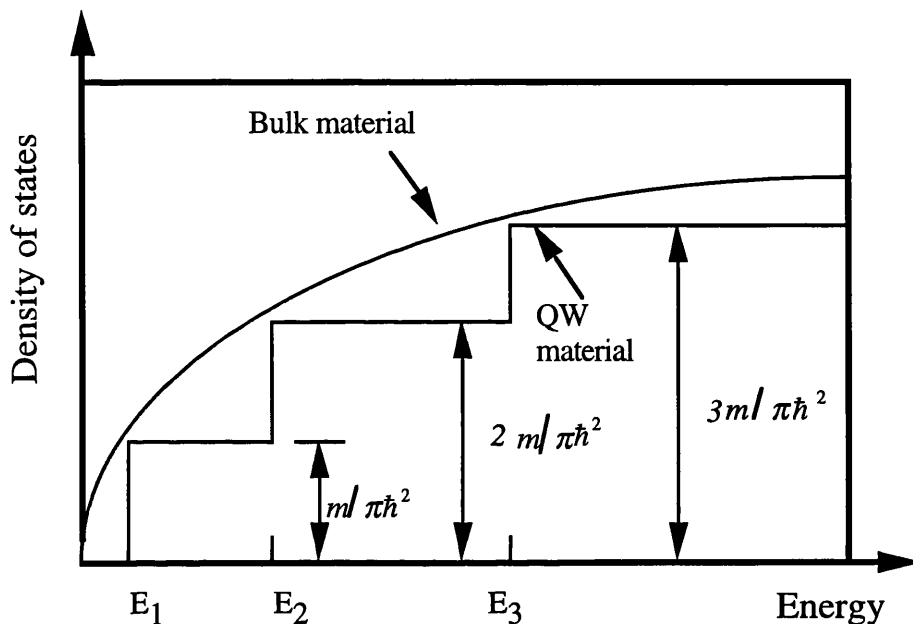


Fig. 2.4: Density of states (DOS) spectra for bulk and QW material.

Therefore, QWs have properties intermediate between those of 3D and 2D systems, and the properties of excitons in them are very different to those in bulk material. In the case of a bulk semiconductor, there is only one exciton below the band-edge, but with quantum wells there are two observable excitons. These arise from the lifting of the degeneracy of the heavy and light hole bands due to the confinement. Furthermore, excitons are associated with every level in the step-like joint density of states in quantum well structures, resulting in two excitons below each absorption level in the QW absorption spectrum.

Unlike bulk semiconductor excitons, QW excitons are in general observable at room temperature. This is due to two important factors related to the confinement of

the exciton in the well structure. The reduced dimensionality has the effect of compressing the exciton and increasing the overlap between the electron and hole wavefunctions, leading to an increase in the binding energy of the system. Because of the increase in binding energy, the exciton resonances are further away in energy from the continuum. The contrast between the exciton resonances and the continuum is also greater, while the interaction between excitons and phonons remains about the same as in bulk material. However, because the LO phonon energy of 36 meV is so much greater than the excitonic binding energy of about 10 meV, excitons are still very easily ionised, so that their lifetime at room temperature in GaAs/AlGaAs QWs is about 400 fs [13]. The effect of excitons on the absorbance spectrum can be seen in Fig. 2.5.

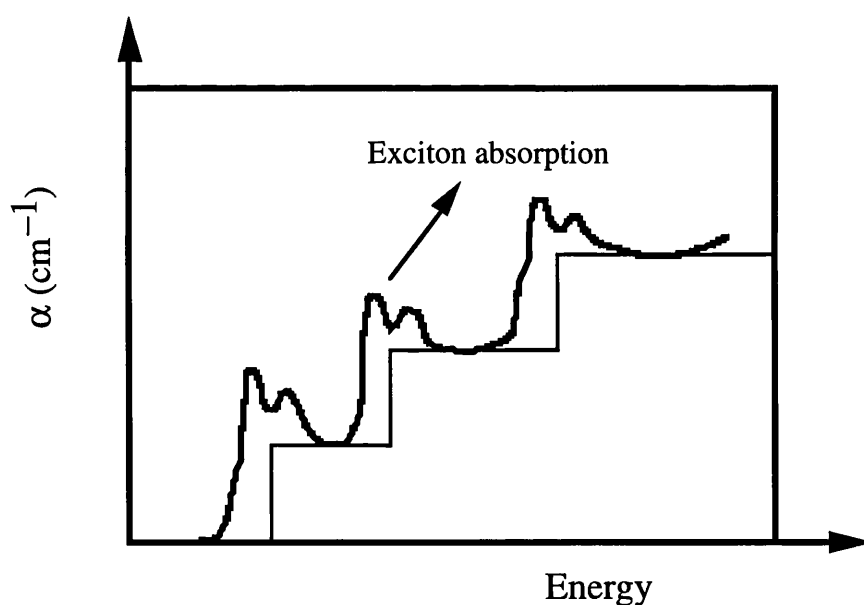


Fig. 2.5: The absorption edge spectrum predicted for a quantum well material with a step function density of states.

The excitons are seen as peaks just below the quantum well band to band absorptions.

2.4.2 The Electric Field Effects

Electroabsorptive effects in both bulk semiconductor heterostructures and quantum wells have received much attention in recent years. When a D.C. electric

field is applied to a semiconductor, a change in the optical absorption spectrum may result. The electroabsorption exhibited by bulk semiconductors is due to the Franz-Keldysh effect [14]. It states that there is a small shift of the absorption edge to lower frequencies in the presence of an electric field. The excitons play little part in this phenomenon because they are ionised by the field. In quantum wells, however, for fields parallel to the growth direction (i. e., perpendicular to the layers) the quantum confinement is strong enough to prevent significant ionisation. The field produces a considerable red shift of the exciton peak. This phenomenon is known as the quantum-confined Stark effect [15], and may be employed in number of optical devices, including modulators and low energy switches [16]. The bandgap of the modulator material is larger than the photon energy of the light source to be modulated. Under zero external electric field the material is transparent so the light can pass with very little loss. When an external electric field is applied the bandgap narrows so that the material becomes highly absorptive and the light is absorbed. For the case of electroabsorption with fields perpendicular to the growth direction (i. e., parallel to the layers) the situation is similar to that in bulk material because the same physical processes are operating.

2.4.3 Refractive Index

The electronic band structure of a semiconductor plays an important role in determining its optical properties. The fundamental electronic excitation spectrum of a material is generally described in terms of a frequency-dependent complex dielectric function:

$$\epsilon(\omega) = \epsilon_1(\omega) + i \epsilon_2(\omega) \quad (2.12)$$

$\epsilon_1(\omega)$ and $\epsilon_2(\omega)$ are interdependent according to the Kramers-Krönig relationships [3], so that $\epsilon_1(\omega)$ can be calculated if $\epsilon_2(\omega)$ is known, and vice versa. The relation between them is dealt with in the next section.

The complex refractive index $n^*(\omega)$ is given by [17]:

$$n^*(\omega) = n(\omega) - i k(\omega) = \varepsilon(\omega)^{1/2} \quad (2.13)$$

where $n(\omega)$ is the real refractive index and $k(\omega)$ is the extinction coefficient. The extinction coefficient is related to the absorption coefficient α through [17]

$$\alpha = \frac{4\pi k}{\lambda} \quad (2.14)$$

The optical constants $n(\omega)$ and $k(\omega)$ are functions of $\varepsilon_1(\omega)$ and $\varepsilon_2(\omega)$. In the wavelength region below the bandgap, absorption can be neglected, so $\varepsilon_2(\omega)$ may be taken as zero. Thus, the refractive index can be expressed by:

$$n(\omega) \approx \varepsilon_1(\omega)^{1/2} \quad (2.15)$$

2.4.4 Kramers-Kronig Relations

The real and imaginary parts of a response function can be shown to be related through a set of integrals known as the Kramers-Krönig integrals. They are based on the principle of causality, i.e. that the effect can not precede the cause. This relationship is of particular importance when applied to an optical system, where the dielectric function is the linear response function and the real and imaginary parts of this give rise to the refractive index and the absorption respectively. In this case the Kramers-Krönig integrals take the form [18]:

$$\varepsilon_1(\omega) - 1 = \frac{2}{\pi} P \int_0^\infty \frac{\omega'}{(\omega')^2 - \omega^2} \varepsilon_2(\omega') d\omega' \quad (2.16)$$

$$\varepsilon_2(\omega) = -\frac{2}{\pi} P \int_0^\infty \frac{\varepsilon_1(\omega')}{(\omega')^2 - \omega^2} d\omega' \quad (2.17)$$

where $\varepsilon_1(\omega)$ is the real part of the dielectric constant, and $\varepsilon_2(\omega)$ is the imaginary part. P denotes the principal part of the integral, which means that the integral is evaluated over all values ω' of between 0 and ∞ , except for at the singularity, i.e. when $\omega' = \omega$.

It is important to note that the relationship is only valid for a linear response function. Also, it is seen from these relations that, if the real part of the dielectric constant is known at all frequencies ω' , then the imaginary part at any individual frequency ω can be calculated, and vice versa. The real part of the dielectric constant is related to the refractive index, and the imaginary part to the absorption coefficient. So, by substituting the relations between them into the Kramers-Krönig relations, a new set of relations may be obtained. The change in refractive index Δn associated with a change in absorption $\Delta\alpha$ can therefore be expressed as [19]:

$$\Delta n(\omega) = \frac{c}{\pi} P \int_0^\infty \frac{\Delta\alpha(\omega')}{(\omega')^2 - \omega^2} d\omega' \quad (2.18)$$

It is therefore possible to extract information on the refractive index change in a semiconductor from measured absorption change by transforming it through the Kramers-Krönig relation. A corresponding relation can be derived relating the absorption to the refractive index over all frequencies, but this is seldom used as refractive index changes are usually quite extensive in frequency.

2.5 Linear Absorption in Bulk Semiconductors

Absorption occurs when photons of energy $\hbar\omega$ are used to excite electrons or holes with energy E_i to a higher energy state E_f , so that:

$$E_f = E_i + \hbar\omega \quad (2.19)$$

The absorption coefficient depends on the transition rate of electrons from one energy state to another due to photons of various energies, and this rate can be calculated using *Fermi's Golden Rule* [20]. This shows that the energy of the final state must be the same as the energy of the initial state, as expected for the conservation of energy. This rule is derived using perturbation theory, and states that the transition rate from an initial state 'i' to a final state 'f' due to a perturbation of the form $V \exp(-i\omega t)$, which could represent photons, phonons or another form of excitation, is given by [12]:

$$\text{Transition Rate} = \frac{2\pi}{\hbar} |V_{fi}|^2 N(E_f) \quad (2.20)$$

where $E_f = E_i + \hbar\omega$, $V_{fi} = \int \Psi_f^* V(t) \Psi_i$, and $N(E_f)$ is the density of states at energy E_f . It is noted that ψ_i and ψ_f are the initial and final wave-functions and V_{fi} is known as the matrix element or overlap integral between two energy states, and is extremely important in optical processes, as its magnitude determines the strength and selection rules of optical processes.

Figs. 2.6 and 2.7 show typical absorption spectra for a semiconductor over a very large range of photon energies. The most important part of the spectra for the study of semiconductors is the absorption edge at about $1 \mu\text{m}$ (i.e. about 1 eV), and this is the region in which the absorption of photons results in the transition of electrons from the top of the valence band to the bottom of the conduction band. For photon energies $h\nu$ just greater than the band gap E_g the density of states (and so, by Fermi's Golden Rule, the absorption coefficient) is proportional to $(h\nu - E_g)^{1/2}$ [11].

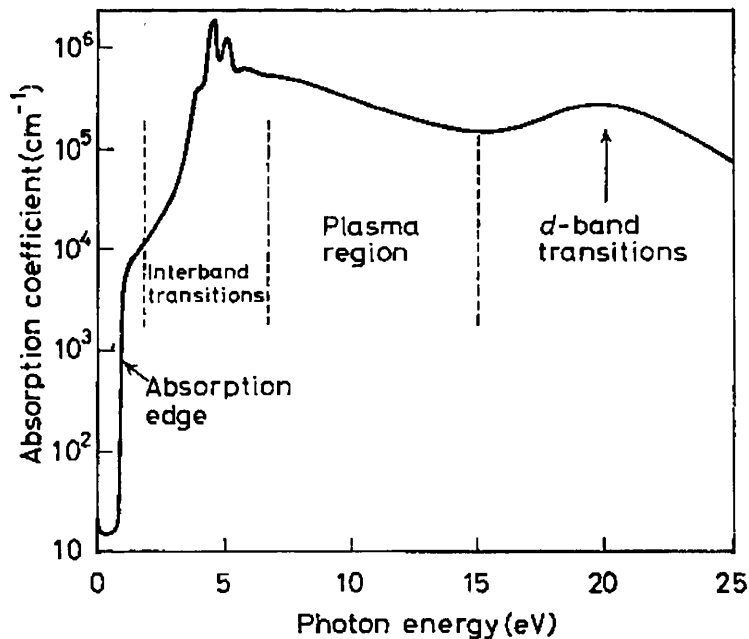


Fig. 2.6: Typical semiconductor ultraviolet absorption spectrum (after ref. [21]).

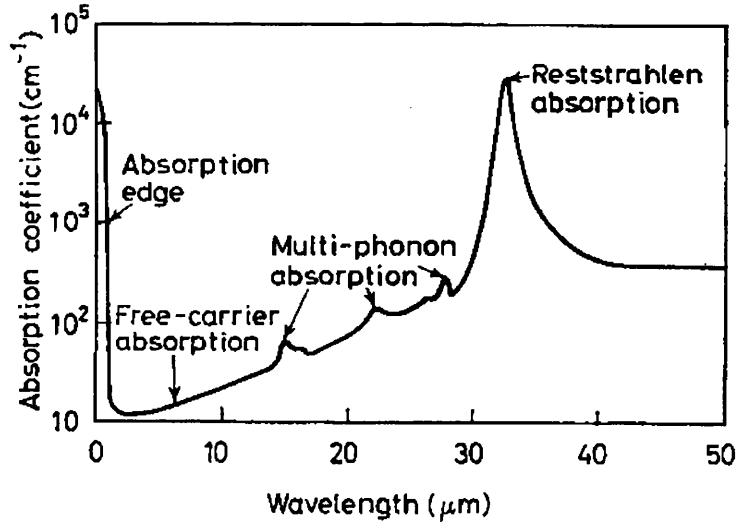


Fig. 2.7: Typical semiconductor infrared absorption spectrum (after ref. [21]).

Absorption of photons of higher energy, up to about 5 eV, results in electron transitions from deeper in the valence band into higher energies in the conduction band. Further into the ultra-violet spectrum, i.e. at still higher energies, plasma effects are seen due to the valence band electrons behaving like a plasma of free particles, and photon energies greater than about 15 eV can cause the inner-shell electrons to be excited into the conduction band [22].

In theory, the absorption edge would be infinitely steep due to the direct band-to-band transition, but in practice it falls off exponentially, as shown in Fig. 2.7. This additional absorption can occur for several reasons. The existence of shallow impurity bands in the forbidden gap can lead to a tail in the density of states which extends into the forbidden gap. The final important cause of the absorption tail is inelastic phonon scattering, which is described by Urbach's Rule [23]:

$$\frac{d(\ln\alpha)}{d(h\nu)} = \frac{-1}{K_B T} \quad (2.21)$$

where α is the absorption coefficient, $h\nu$ is the photon energy, K_B is Boltzmann's constant and T is the temperature.

On the long wavelength side of the absorption edge, an increase in absorption is seen due to free carrier absorption, that is transition of free electrons and holes within the conduction band, as in metals. At still longer wavelengths, there are features in the absorption spectrum due to lattice vibrations and phonons [11].

The region of the spectrum of interest in this thesis is at energies at or below the absorption edge. Providing that the incident photon energy is comparable to that of the energy gap, electrons can be excited from the valence to the conduction band. Both energy and momentum must be conserved in this process.

2.6 Free Carrier Absorption

Electrons in the conduction band or holes in the valence band can absorb photons of energy less than the exciton resonance, and make transitions higher into their bands. Such a process is usually referred to as an *intraband transition*. An expression for the absorption coefficient α_{fc} due to free carrier absorption can be derived from classical electromagnetic theory.

The motion of an electron in the presence of an applied field $E_o \exp(i\omega t)$ is given by [17]:

$$m^* \frac{d^2 x}{dt^2} + m^* g \frac{dx}{dt} = -eE_o e^{i\omega t} \quad (2.22)$$

where m^* is the effective mass of the electrons (since the electrons are not completely free as in a vacuum), g is a damping coefficient and x is the displacement. The first term in (2.22) is the familiar force term; the second term represents a linear damping of the electron motion by interaction with the lattice, and the term to the right of the equals sign is the applied force. The steady state solution of (2.22) is:

$$x = \frac{(eE_o)/m^*}{\omega^2 - i\omega g} e^{i\omega t} \quad (2.23)$$

The dielectric constant of a material is given , in general, by:

$$K = \frac{\epsilon}{\epsilon_0} = 1 + \frac{P}{\epsilon_0 E} \quad (2.24)$$

where P is the polarisation. In the presence of free carriers

$$P = P_0 + P_1 \quad (2.25)$$

where P_0 is the component present without carriers, i.e. the polarisation of the dielectric, and P_1 is the additional polarisation due to the shift of the electron cloud in the field. Thus,

$$K = \frac{\epsilon}{\epsilon_0} = 1 + \frac{P_0}{\epsilon_0 E} + \frac{P_1}{\epsilon_0 E} \quad (2.26)$$

or

$$K = n_0^2 + \frac{P_1}{\epsilon_0 E} \quad (2.27)$$

where n_0 is the index of refraction of the material without carriers present. Assuming an isotropic material, in which P and E are in the same direction,

$$P_1 = -Nex \quad (2.28)$$

where N is the free carrier concentration per cm^3 and x is the displacement already given in (2.23). Substituting (2.28) and (2.23) into (2.27), we get

$$K = n_0^2 - \frac{(Ne^2)/(m^* \epsilon_0)}{\omega^2 - i\omega g} \quad (2.29)$$

Separating the real and imaginary parts of K , we find

$$K_r = n_0^2 - \frac{(Ne^2)/(m^* \epsilon_0)}{\omega^2 + g^2} \quad (2.30)$$

and

$$K_i = \frac{(Ne^2 g)/(m^* \omega \epsilon_0)}{\omega^2 + g^2} \quad (2.31)$$

The damping coefficient g can be evaluated from the known steady-state solution of (2.22), since, in the steady-state, $d^2x/dt^2 = 0$,

$$m^*g \frac{dx}{dt} = eE \quad (2.32)$$

Mobility, μ , is defined by:

$$\frac{dx}{dt} = \mu E \quad (2.33)$$

which yields

$$g = \frac{e}{\mu m^*} \quad (2.34)$$

At optical frequencies, g can most certainly be neglected in the denominator of (2.30) and (2.31). Making this approximation, and also substituting for g from (2.34), we obtain:

$$K_r = n_0^2 - \frac{Ne^2}{m^* \epsilon_0 \omega^2} \quad (2.35)$$

and

$$K_i = \frac{Ne^3}{(m^*)^2 \epsilon_0 \omega^3 \mu} \quad (2.36)$$

The exponential loss coefficient α is related to the imaginary part of the dielectric constant by:

$$\alpha = \frac{kK_i}{n} \quad (2.37)$$

where n is the index of refraction and k is the magnitude of the wavevector. Hence, for the case of free carrier absorption,

$$\alpha_{fc} = \frac{kK_i}{n} = \frac{Ne^3}{(m^*)^2 n \epsilon_0 \omega^2 \mu c} \quad (2.38)$$

where $k \equiv \omega/c$ has been used. Since $c = v\lambda_0$ and $\omega = 2\pi\nu$, (2.38) can be rewritten as:

$$\alpha_{fc} = \frac{Ne^3\lambda_0^2}{4\pi^2n(m^*)^2\mu\epsilon_0c^3} \quad (2.39)$$

In many guided wave devices, the major loss due to free carrier absorption occurs from the overlap of the evanescent tail of guided modes with heavily doped substrate or confining layers.

It is clear from Equation (2.35), the change in index of refraction is $-(Ne^2)/(m^*\epsilon_0\omega^2)$ due to the presence of the carriers.

The classical expression for α_{fc} given in (2.39) exhibits a λ_0^2 dependence. However, this is rarely exactly observed in practical situations, because the model on which Equation (2.39) is based assumes a constant, wavelength independent, damping coefficient g . In reality, the damping that occurs because of interaction with the lattice is a varying quantity, which depends on whether acoustic phonons, optical phonons, or ionised impurities are involved. In general, all three will be involved to some extent. It has been shown that α_{fc} varies as $\lambda_0^{1.5}$ for acoustic mode scattering of the carriers and as $\lambda_0^{2.5}$ for optical mode scattering, while for impurity scattering α_{fc} varies between λ_0^3 and $\lambda_0^{3.5}$ [17].

The diagrams of Figs. 2.1 and 2.2 show only interband transitions, between valence and conduction bands; however, both direct and indirect transitions also can take place within a band (*intraband*) or between energy states introduced by dopant atoms and/or defects. In all cases, the principles of conservation of energy and momentum (wavevector) apply. Free carrier absorption is usually taken to include transitions of electrons from shallow donor states to the conduction band and transitions of holes from shallow acceptor states to the valence band.

It can be shown that the free carrier absorption in a semiconductor is a function of the photon energy, the concentration of free carriers and the temperature [22]. Note that free-carrier absorption takes place even when $h\nu < E_g$, and frequently this absorption dominates the spectrum below the fundamental edge. For $h\nu > E_g$, of course, both types of absorption—fundamental and free-carrier—occur simultaneously.

2.7 Two Photon Absorption

The dominant contribution to non-linear absorption in the frequency range $\frac{E_g}{2} < \hbar\omega < E_g$ is two-photon absorption (TPA) where the simultaneous absorption of two photons gives rise to a non-linear absorption proportional to irradiance. TPA in semiconductors is of interest as it provides a non-linear spectroscopic technique, in addition to having important consequences for all-optical switching. Because the TPA coefficient is proportional to the intensity, it was not observed until the invention of the laser [24], despite having been first predicted thirty years earlier.

TPA occurs when an electron is excited from the valence band into the conduction band through an intermediate state [25], by absorbing two photons whose individual energies are lower than the bandgap, but the combined energy is greater than the bandgap, as shown in Fig. 2.8. This intermediate state can be any state in the valence band, the conduction band, or anywhere within the semiconductor band structure, provided that momentum is conserved in the transition. It is known that the transition probability is highest when the energy difference between the state is smallest, i.e. when the intermediate state lies closest to the upper valence band or lowest conduction band (because of the energy difference between the initial and intermediate states which occurs in the denominator of the transition probability) [26]. During the first transition to the intermediate state, energy is not conserved and the electron can only remain in the intermediate state for a time governed by the Uncertainty Principle [27]:

$$\Delta E \Delta t \approx \hbar \quad (2.40)$$

If the second photon is absorbed within the time, Δt , the electron undergoes a second transition to reach the final energy state. For the entire TPA process both energy and momentum are conserved.

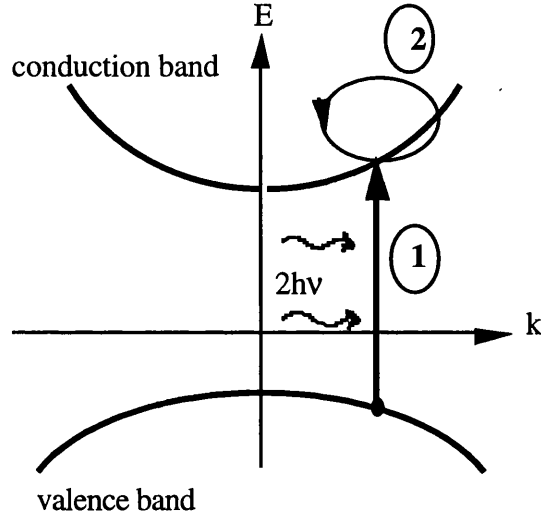


Fig. 2.8: E-k diagram of two-photon absorption.

The attenuation of the light as it propagates through the medium can be described by:

$$\frac{dI}{dz} = -\alpha I - \beta I^2 \quad (2.41)$$

where α is the linear absorption coefficient, I is the light intensity, β is the two-photon absorption coefficient and z is the propagation distance through the material. The intensity as a function of distance is given by [28]:

$$I(z) = \frac{I(0) \alpha e^{-\alpha z}}{\alpha + \beta I(0) (1 - e^{-\alpha z})} \quad (2.42)$$

One of the easiest ways of measuring β is therefore measuring the sample transmission for a beam of varying input intensities, with an input beam possessing photons with energy less than the bandgap E_g but greater than $E_g/2$. For a wide variety of semiconductors β was measured, and was found to be given by [29]:

$$\beta = \frac{K\sqrt{E_p}}{n^2 E_g^3} f\left(\frac{2\hbar\omega}{E_g}\right) \quad (2.43)$$

where K is a material independent constant, n is the linear refractive index, E_p is the Kane momentum energy, which is nearly material independent, and the function f depends on the band structure. To a good approximation, β is found to be proportional to E_g^{-3} .

Earlier calculations and measurements of β in semiconductors have concentrated on the linearly polarised single beam case (i.e. ignoring any polarisation dependence) [29]. But it has been shown that there is a variation in the two-photon absorption coefficient which depends on the relative orientation of the optical polarisation with the crystalline axes for two beam experiments [30]. This point will be discussed in more details in Chapter 4.

2.8 Conclusions

In this chapter the basic concepts of optical nonlinearity and semiconductor bandgap physics have been briefly reviewed, followed by a survey of the concept of excitons in bulk and quantum well materials. The Kramers-Krönig relations have been stated, together with the conditions for their use.

Bulk semiconductor absorption spectra over a very large range of photon energies were discussed and the causes of their significant features identified, followed by a description of free carrier absorption. Finally, the non-linear optical process of two-photon absorption was addressed.

2.9 References

- [1] Y. R. Shen, "Principle of Non-linear Optics", J. Wiley, New York, 1984.
- [2] P. Horan and W. Blau, "Optical nonlinearity near the bandgap in semiconductor " Contemp. Phys. Vol. 28, pp. 59-68, 1987.
- [3] P. N. Butcher and D. Cotter, "The Elements of Non-linear Optics", Cambridge University Press, 1990.
- [4] B. S. Bhumbra, "Non-linear optical waveguide devices in GaAs/AlGaAs", Ph.D. thesis, Dept. of Electronics and Electrical Engineering, Glasgow University, 1990.
- [5] D. A. B. Miller, C. T. Seaton, M. E. Prise and S. D. Smith, "Band-gap resonant nonlinear refraction in III-V semiconductors", Phys. Rev. Lett., Vol. 47, pp. 197-200, 1981.
- [6] D. A. B. Miller, S. D. Smith and B. S. Wherrett, "The microscopic mechanism of third order nonlinearity in InSb", Opt. Commun., Vol. 35, pp. 221-226, 1980.
- [7] H. Kawai, K. Kaneko, and N. Watanabe, "Photoluminescence of GaAs-AlGaAs quantum wells grown by metal organic chemical vapour deposition", J. Appl. Phys., Vol. 56, pp. 463-467, 1984.
- [8] K. Seeger, "Semiconductor Physics", Spriger Verlag, 1982.
- [9] N. Peyghambarian and H. M. Gibbs, "Optical nonlinearity, bistability and signal processing in semiconductors", J. Opt. Soc. Am., B 2, pp. 1215-1227, 1985.
- [10] M. Jaros, "Physics and Application of Semiconductor micro structures", Oxford University Press, 1989.
- [11] M. A. Omar, "Elementary Solid State Physics", Addison-Wesley, 1975.
- [12] J. H. Davies, "Quantum mechanics course given to postgraduate students", Dept. of Electronics and Electrical Engineering, University of Glasgow, 1994.
- [13] S. Schmitt-Rink, D. S. Chemla and D. A. B. Miller, "Linear and nonlinear optical properties of semiconductor quantum wells", Advances in Physics, Vol. 38, pp. 89-188, 1989.

- [14] L. V Keldysh, "The effect of a strong electric field on the optical properties of insulating crystals", *Sov. Phys. Jépt.*, Vol. 34, pp. 788-790, 1958.
- [15] D. A. B. Miller, D. S. Chemla, T. C. Damen, A. C. Gossard, W. Wiegmann, T. H. Wood, C. A. Burrus, "Band-edge absorption in quantum well structures: The Quantum Confined Stark Effect", *Phys. Rev. Lett.*, Vol. 53, pp. 2173-2176, 1984.
- [16] D. A. B. Miller, D. S. Chemla and S. Schmitt-Rink, "Optical Nonlinearities and Instabilities in Semiconductors", Academic Press, pp. 325-359, 1988.
- [17] R. A. Smith, "Semiconductors", Cambridge University Press, 1986.
- [18] F. Stern, "Elementary Theory of the Optical Properties of Solids", *Solid State Physics*, Vol. 15, p. 299, 1963.
- [19] D. J. Westland, A. M. Fox, A. C. Maciel, J. F. Ryan, "Optical studies of excitons in GaInAs/InP multiple quantum wells", *Appl. Phys. Letts.* Vol. 50, pp. 839-841, 1987.
- [20] R. M. Eisberg, "Fundamentals of Modern Physics", John Wiley and Sons, 1964.
- [21] T. S. Moss, G. J. Burrell and B. Ellis, "Semiconductor Optoelectronics", Butterworths, 1973.
- [22] J. N. Hodgson, "Optical Absorption and Dispersion in Solids", Chapman and Hall, 1970.
- [23] F. Urbach, "The long wavelength edge of photographic sensitivity and of the electronic absorption of solids", *Phys. Rev.*, Vol. 92, p. 1324, 1953.
- [24] W. Kaiser and C. G. B. Garrett, "Two-photon excitation in $\text{CaF}_2:\text{Eu}^{2+}$ ", *Phys. Rev. Lett.*, Vol. 7, pp.229-231, 1961.
- [25] C. C. Lee and H. Y. Fan, "Two-photon absorption with exciton effect for degenerate valence bands", *Phys. Rev. B*, Vol. 9, pp. 3502-3516, 1974.
- [26] H. N. Spector, "Two-photon absorption in semiconducting quantum-well structures", *Phys. Rev. B*, Vol. 35, pp. 5876-5879, 1987.
- [27] A. Miller, D. A. B. Miller and S. D. Smith, "Dynamic nonlinear optical processes in semiconductor", *Advances in Phys.*, Vol. 30, pp. 697-800, 1981.

[28] F. R. Laughton, J. H. Marsh and J. S. Roberts, "Intuitive model to include the effect of free-carrier absorption in calculating the two-photon absorption coefficient", *Appl. Phys. Lett.*, Vol. 60, pp. 166-168, Jan. 1992.

[29] E. W. Van Stryland, H. Vanherzeele, M. A. Woodland, M. J. Soileau, A. L. Smirl, S. Gula and T. F. Boggess, "Two photon absorption, nonlinear refraction, and optical limiting in semiconductors", *Opt. Eng.*, Vol. 24, pp. 613-623, 1985.

[30] D. C. Hutchings and B. S. Wherrett, "Theory of anisotropy of two photon absorption in zinc-blende semiconductor", *Phys. Rev. B*, Vol. 49, pp. 2418-2426, 1994.

Chapter 3

Waveguide Design and Fabrication

This chapter outlines the methods used to design and fabricate the waveguide of the device to be used in linear and non-linear optical experiments.

In this chapter an introduction to waveguide theory will be given, followed by a brief description of the two programs used to design the waveguides. The two computer programs used are called Fourlay and F-Wave. Fourlay is a program written by B. Bhumbra of this Department, which calculates the mode depth and slab refractive index in a structure containing up to four layers. Fourlay can also be used to model two dimensional confinement using the effective index method. F-Wave, written by M. R. S. Taylor also of this Department, uses a finite difference model to solve the vector electromagnetic equations of ridge structures containing multiple layers.

3.1 The Slab Waveguide

This section gives a brief introduction to a waveguide theory for slab waveguides. For a more detailed treatment, the reader should refer to the references [1, 2]. The slab structure is very important in the realisation of optoelectronics devices: it is from a slab that many different devices are fabricated.

We first consider the conditions necessary for slab guiding to occur. The planar slab guide in Fig. 3.1. consists of a substrate of refractive index n_3 , a film of refractive index n_1 and a cover of refractive index n_2 such that $n_1 > n_2 \geq n_3$. We assume that the light is monochromatic and coherent, and that the dielectrics are lossless and isotropic.

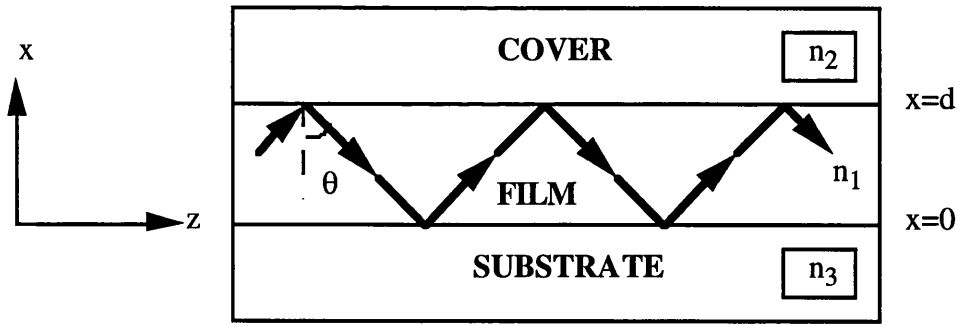


Fig. 3.1: Cross section of a planar slab waveguide (after ref. 1).

2-D waveguides can be sub-divided into two groups depending on the relative value of the refractive index difference between the cladding layers. If the cladding layers have the same permittivity, the structure is termed a symmetrical slab waveguide, whereas if they are different, the structure is an asymmetrical slab waveguide. These two structures have different dispersion relations which, in the case of the symmetrical slab waveguides, lifts the restrictions on guide thickness with respect to cut-off of the zero-order guided mode. Consider, for instance, the case of a three layer slab waveguide as described above. Let the refractive index of the guide layer be n_1 , and the refractive indices of the upper and lower cladding layers n_2 and n_3 respectively. This structure will act as a guide for the light in the middle layer only if $n_1 > n_2, n_3$. The waveguide is symmetrical if $n_2 = n_3$ and asymmetrical if $n_2 \neq n_3$. The waveguiding condition and dispersion relation of this structure can be evaluated both from a ray treatment approach and as a solution derived from Maxwell's equation in an electromagnetic field approach.

In order for the light to be guided, it must experience total internal reflection at the film-substrate and film-cover layer. Consider a light beam in the film material impinging on the interface with the substrate material. By Snell's Law, total internal reflection of the light will occur if the angle of incidence of the light is greater than the critical angle defined as:

$$\theta_c = \sin^{-1}(n_2/n_1) \quad (1)$$

The propagation constant β of a guided mode in the film in the Z-direction is defined as:

$$\beta = k n_1 \sin \theta = k n_e \quad (2)$$

where $k (=2\pi/\lambda)$ is the transverse propagation constant, n_e is the refractive index in the film region, and so the propagation constant can be seen to be bounded by the conditions:

$$kn_3 < \beta < kn_1 \quad (3)$$

The transverse propagation constants can be defined for the three sections of the slab waveguide as

$$k_2 = (\beta^2 - n_2^2 k^2)^{1/2} \quad (4)$$

$$k_1 = (n_1^2 k^2 - \beta^2)^{1/2} \quad (5)$$

$$k_3 = (\beta^2 - n_3^2 k^2)^{1/2}. \quad (6)$$

The fields in the three regions are assumed to be of the forms:

$$E_{y2}(x, z) = E_2 \exp[-k_2(x-d)] \exp[-j\beta z] \quad (x > d) \quad (7)$$

$$E_{y1}(x, z) = E_1 \cos[k_1 x - \psi] \exp[-j\beta z] \quad (0 < x < d) \quad (8)$$

$$E_{y3}(x, z) = E_3 \exp[k_3 x] \exp[-j\beta z] \quad (x < 0) \quad (9)$$

where ψ is a phase constant defined by the boundary conditions. Since both E_y and dE_y/dx must be continuous across the boundaries at $x = 0$ and $x = d$, we find that for TE polarisation i.e. E field parallel to interfaces:

$$\tan \psi = k_3/k_1 \quad (10)$$

$$\tan(k_1 d - \psi) = k_2/k_1 \quad (11)$$

and so, since $\tan(x) = \tan(x \pm m\pi)$, the dispersion relation may be found to be:

$$k_1 d = \tan^{-1}(k_2/k_1) + \tan^{-1}(k_3/k_1) \pm m\pi \quad (12)$$

where $m = 0, 1, 2, \dots$

The bounds on β have already been shown to be $kn_3 < \beta < kn_1$ and, as β tends to kn_3 , that is as k_3 tends to zero, guiding cuts off. We can therefore find the cut off wavelength for a given mode by setting k_3 to zero in Equation 12, and by setting m to the number of the appropriate mode. This leads to the relation that, at cut off of the m -th order mode:

$$k_1 d = \tan^{-1}(k_2/k_1) \pm m\pi \quad (13)$$

The analogous equation to Equation 12 can be found for TM polarised light by using the condition that H_y and $n^{-2} dH_y/dx$ must be continuous across the boundaries at $x = 0$ and $x = d$. The dispersion relation for TM polarised light is thus found to be:

$$k_1 d = \tan^{-1}(n_1^2 k_2 / n_2^2 k_1) + \tan^{-1}(n_1^2 k_3 / n_3^2 k_1) \pm m\pi \quad (14)$$

3.2 Three Dimensional Waveguide

A three dimensional dielectric waveguide is one where propagating modes are bound in both transverse directions, because this confinement makes it necessary to consider field variations in all three orthogonal directions. In other words, the optical fields are confined in both x and y -directions for a wave travelling in the z -direction. Examples of these types of guides, in which the light is confined laterally as well as vertically are shown below in Fig. 3.2.

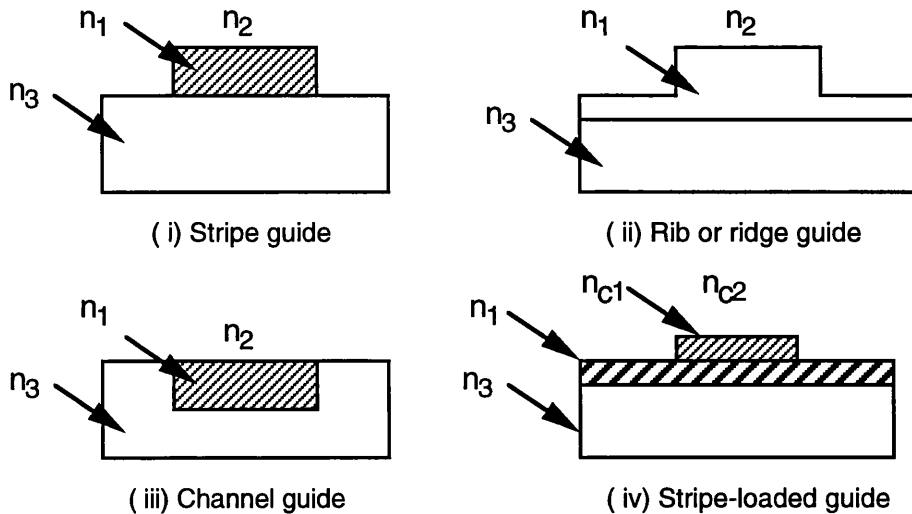


Fig. 3.2: Examples of different geometries used to confine light both vertically and laterally.

The three dimensional waveguides are of particular importance for optical integrated circuits (OIC) due to their ability to maintain high optical irradiances over relatively long distances and because they facilitate a method to obtain single mode guiding through the proper choice of the confinement parameters. Numerical calculations can be performed by a number of methods to analyse the stripe waveguide structure.

3.3 Numerical Methods

In the above treatment of the slab or 2-D waveguide, one of the basic assumptions made was that there was no variation of the electric or magnetic fields in the transverse direction. For the 3-D waveguide this is not the case, and exact analytic solution is no longer possible. Below is a short description of some of the methods applicable to the semiconductor waveguide system.

3.3.1 Effective Index Method

The effective index method (EIM) [3] is an approximate method which converts a complicated two dimensional (i.e. rib) waveguide problem, into several easily solved one dimensional (i.e. slab) problems. In designing the material structure

various parameters, such as the fraction of aluminium in cladding and the thickness of the layers, should be adjusted in order to determine which combination leads to optimum confinement of the light. The simplicity, and hence the speed, of the effective index method is a great advantage in doing this, so this method was used for the preliminary material design, which was then checked and adjusted using the more accurate, but slower, numerical method described in Section 3.3.2.

The basic concept of the method is to divide the 3-D waveguide into three sections; one each for the regions either side of the guide region, and one for the guide region itself. Consider a rib waveguide made in this structure, as shown in Fig. 3.3.

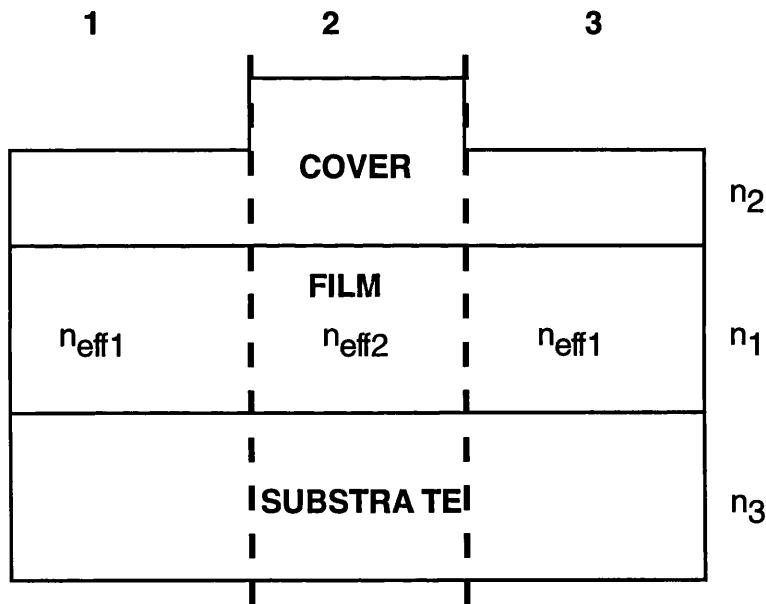


Fig. 3.3: Cross section of a three layer rib waveguide.

It can be seen from Equation 12 that the effective index $n_e = \beta/k$ of the slab structure depends on the thickness of the guiding region. When a rib guide is used, the guiding layer is thicker under the rib, and so the effective index is different in regions 1 and 3 (n_{eff1}) from that in region 2 (n_{eff2}). The effective index and mode size for each section is then deduced using either ray optics, or electromagnetic analysis. The next step is to combine the effective indices for each of these sections into a singular slab waveguide. This "sandwich" can then be analysed similarly to the previous slabs, but in the orthogonal plane (i. e. the opposite polarisation) due to the theoretical "turning"

of the waveguide, during the conversion to a single slab. The core thickness and index of this new slab are set by the width of the waveguide rib and the effective index calculated for the middle slab. The structure is bound either side by cladding layers of indices given by the effective (slab) indices found for the side regions as explained above.

The material for the waveguides used in this thesis is a four layer structure, rather than the three layer structure considered in section 3.3.1, but the method used to solve this is almost identical to that described. The computer program used for this method was Fourlay, which was written by Bindi Bhumbra, formerly of this Department [4].

3.3.2 Vector Finite Difference Method

The finite difference method of solving the vector electromagnetic wave equation for a waveguiding structure is more accurate, but uses more computer time. The program F-Wave, written by Michael Taylor of this Department, was used to analyse the waveguide material structure after Fourlay had been used to design the structure roughly. The program splits the structure, which can consist of up to 100 layers of different refractive index, into a fine mesh. In order to speed up the program, the effective index method is used at first to gain an estimate of the initial field distribution. The second differentials in the wave equation are then approximated by a Taylor series expansion for each section of the mesh, and the resulting equations solved iteratively.

3.4 Refractive Index of Bulk AlGaAs

In order to design the material structure for optimum confinement of the light, it is necessary to obtain accurate values for the refractive indices of the different layers involved. There are many reports in the literature of refractive index calculations and measurements for GaAs and AlGaAs bulk material (Adachi 1985, Casey, et. al.

1974, Afromowitz 1974 and Aspen 1986). There is some disagreement between the values quoted in these various publications, and it is not always easy to choose which values to use. As some students of this Department had found that the refractive index values found by using Adachi's model [5] correlated most closely with their measurements, it was decided to use Adachi's model.

Assuming the AlGaAs compound has a direct bandgap, the real part of the dielectric constant can be expressed as [5] :

$$\varepsilon(\omega) = A_o \left\{ g(\chi) + \frac{1}{2} \left[\frac{E_o}{E_o + \Delta_o} \right]^{\frac{3}{2}} g(\chi_{so}) \right\} + B_o \quad (15)$$

Where the following functions are defined:

$$g(\chi) = \chi^{-2} \left[2 - \sqrt{(1+\chi)} - \sqrt{(1-\chi)} \right] \quad (16)$$

$$\chi = \frac{\hbar\omega}{E_o} \quad (17)$$

$$\chi_{so} = \frac{\hbar\omega}{(E_o + \Delta_o)} \quad (18)$$

Where $\hbar = h/2\pi$ (h is Planck's constant) and ω is the angular frequency. E_o and Δ_o are critical point energies and are defined as:

$$E_o = 1.425 + 1.55 x + 0.37 x^2 \quad (19)$$

$$E_o + \Delta_o = 1.765 + 1.115 x + 0.37 x^2 \quad (20)$$

The constants A_o and B_o are determined empirically by fitting to experimental data:

$$A_o(x) = 6.3 + 19.0 x \quad (21)$$

$$B_0(x) = 9.4 - 10.2 x \quad (22)$$

Finally, it is well known that the dielectric constant and refractive index are related through the relationship:

$$n(\omega) = \sqrt{\epsilon_r(\omega)} \quad (23)$$

It is therefore possible to calculate the spectral dependence of the refractive index of AlGaAs, for various concentrations of aluminium. Figure 3.4 shows the spectral dependence of AlGaAs for 20 and 30 % aluminium concentrations.

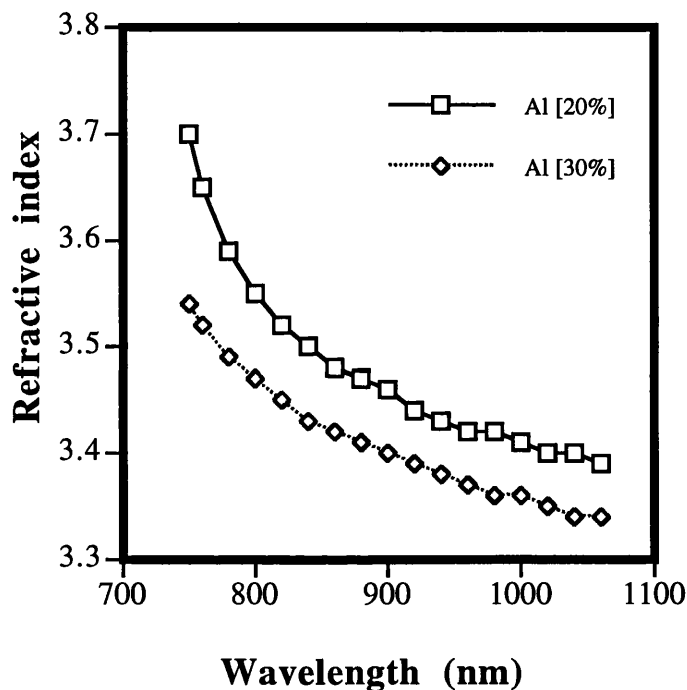


Fig. 3.4: Spectral dependence of the refractive index of AlGaAs for two aluminium concentrations.

3.5 Waveguide Design

After the calculation of the refractive indices, the material was designed to be single moded vertically at both 750 nm and 1.06 μm . This was because it had been hoped to carry out experiments using a Ti:Sapphire laser for the range of wavelengths, 700 to 1000 nm, as well as to use a Nd³⁺:YAG laser operating at

1.06 μm and Nd^{3+} :YLF laser operating at 1.047 μm . Also, the waveguide can be used to measure laser pulse widths with wavelengths greater than 850 nm.

The optimum slab structure found when Fourlay was used initially is shown in Fig. 3.5.

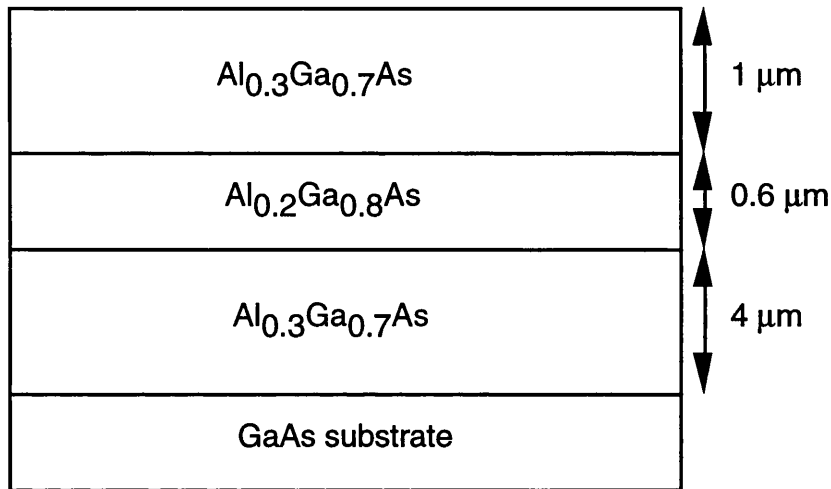


Fig. 3.5: Design for waveguide material.

The waveguide structure with a $\text{Al}_{0.2}\text{Ga}_{0.8}\text{As}$ (740 nm bandgap wavelength) guide region was designed for measuring pulse widths with wavelengths greater than 850 nm. and the thickness of the guide was initially chosen to be equal to the wavelength of the light to be used.

Fourlay gives an exact solution for the vertical confinement of the light, and predicted this structure to be single moded vertically, with a vertical mode thickness of about 1.2 μm at 860 nm. The 4 μm layer of AlGaAs is present in order to minimise the leakage of the light from the guided mode into the substrate.

Once Fourlay had been used to design the slab structure shown in Fig. 3.5, F-Wave was used to calculate the etch depth to give the best combination of the maximum rib width for which the guide is single moded and the minimum mode thickness. The etch depth was found to be about 0.8 μm and Fig. 3.6 shows an example of an output plot from F-Wave for a structure with this etch depth.

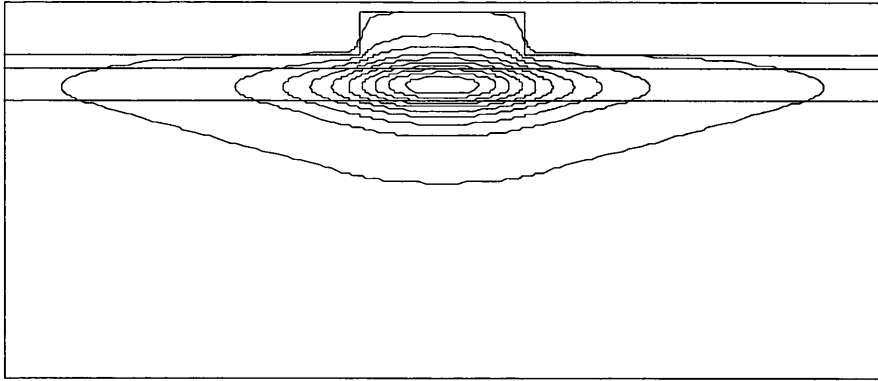


Fig. 3.6: Electric field contour plot of the lowest order TE mode for a 3 μm wide rib and an etch depth of 0.8 μm at wavelength 920 nm. Contours are at 10 % intervals.

The zeroth-order mode has a modal refractive index of 3.454863 according to F-Wave, but 3.45628 with Fourlay, the difference being due to the approximations inherent in the EIM. Due to the length of time required to run F-Wave, it has been found that the best way to use the program is to find approximately the design of waveguide from Fourlay and then, if further accuracy is required, use F-Wave.

3.6 Waveguide Structure

A p-i-n waveguide structure, consisting of an $\text{Al}_{0.2}\text{Ga}_{0.8}\text{As}$ waveguide core surrounded by $\text{Al}_{0.3}\text{Ga}_{0.7}\text{As}$ cladding regions, is shown in Fig. 3.7. The upper and lower cladding layer thicknesses in the structure are 1 μm and 4 μm respectively, both sufficiently thick to ensure only a small optical leakage into the cap and substrate. Those parts of the cladding regions with which there was expected to be significant overlap of the optical mode were left undoped, in order to reduce losses due to free carrier absorption.

p ⁺	GaAs	5x10 ¹⁸	200 Å
p	Al _{0.30} Ga _{0.70} As	5x10 ¹⁷	0.6 μm
i	Al _{0.30} Ga _{0.70} As		0.4 μm
i	Al _{0.2} Ga _{0.8} As		0.6 μm
i	Al _{0.30} Ga _{0.70} As		0.4 μm
n	Al _{0.30} Ga _{0.70} As	5x10 ¹⁷	4 μm
n ⁺	GaAs	substrate	

Fig. 3.7: Structure of p-i-n waveguide material.

3.7 Photoluminescence Spectroscopy

Photoluminescence Spectroscopy measurements provide a quick and easy method to characterise the bandgap of materials. When a semiconductor material is excited by photons possessing energy greater than the bandgap, some electrons are excited from the valence band to the conduction band and hot carriers will be formed. These carriers will emit phonons and relax down through the band until recombination occurs, and a photon is emitted at an energy equal to the bandgap [6].

To increase the accuracy of the photoluminescence technique, measurements were generally taken at liquid nitrogen (77 K) temperatures, since this reduces thermal broadening of the photoluminescence peaks. Fig. 3.8 details the experimental set-up.

The 514.5 nm line from an argon ion laser was coupled into one arm of optical fiber coupler, and the sample was placed on to the protective metal ferrule at the end of one arm using an extremely weak adhesive solution. The sample was then completely submerged in a beaker containing liquid nitrogen. The other end of the fiber coupler was connected to the entrance of a monochromator.

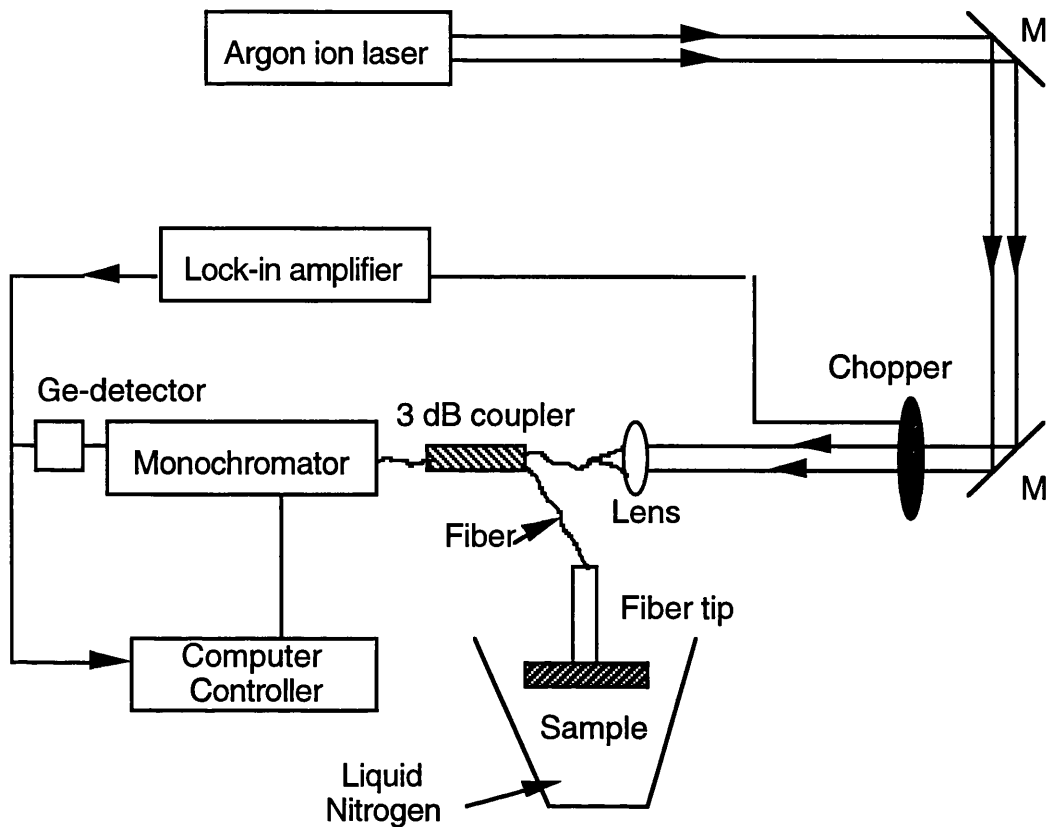


Fig. 3.8: The experimental set-up for PL measurement.

Photoluminescence from the sample travels along the fiber, and is directed toward the monochromator via a directional coupler. The monochromator is stepped through the various wavelengths of interest, and at each point the lock-in amplifier reads the intensity of the photoluminescence signal from the germanium detector. The detector is liquid nitrogen cooled to improve the noise performance [7], and thus optimise the system performance. The set-up is completely automated and the computer can control the scan wavelengths, read the lock-in, step the monochromator, display and record the results. Fig. 3.9 shows a typical photoluminescence measurement from the waveguide material.

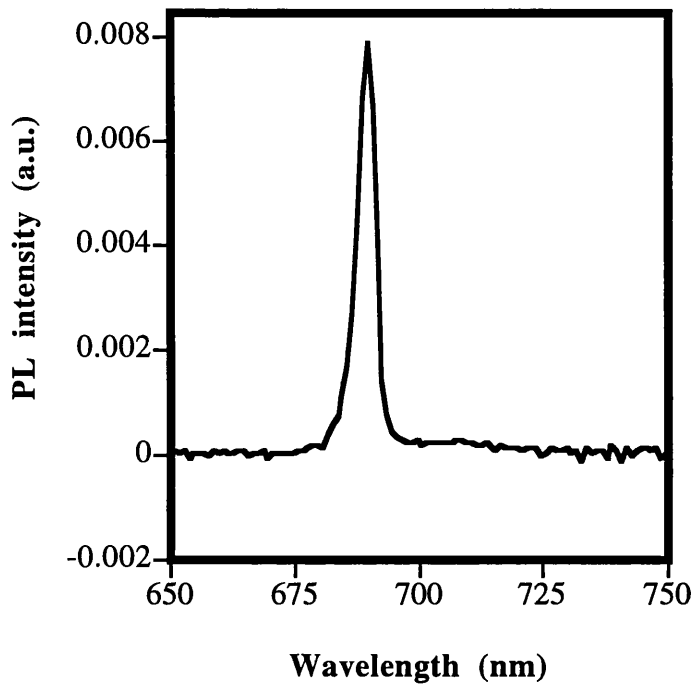


Fig. 3.9: PL plot at 77 K.

3.8 Waveguide Fabrication

The waveguide structure of Fig. 3.7 was grown by MOVPE at the EPSRC Central Facility for III-V Semiconductors at Sheffield University and by MBE at Glasgow University.

The ribs were defined by photolithography, and the material around them was etched away. Samples of about $7 \times 7 \text{ mm}^2$ were used. The processing steps are as follows:

- (1) The sample was first cleaned thoroughly by soaking in an ultrasonic bath in turn in opticlear, methanol, acetone and deionised water, each for five minutes. This stage is very important in order to remove dirt and dust, which might otherwise degrade the transfer of the pattern on the mask onto the resist.

(2) Positive photoresist (Shipley S1400-31) was spun onto the material for 40 s at a speed of 4000 rev/min. This was found to give a uniform layer of resist about 1.8 μm thick.

(3) The sample was baked in an oven at about 90 °C for 30 mins. in order for the solvents in the resist to evaporate, and to harden the photoresist.

(4) A mask with 3, 4 and 5 μm stripes and separated by 100 μm was aligned to and placed in contact with the sample using a mask aligner, and the sample was exposed to UV light. An exposure time of about 12 s was found to give the best definition. It is also very important when fabricating waveguides to ensure that the mask is aligned so that the waveguides are perpendicular to the crystal cleavage planes.

(5) The sample was placed in a beaker of 1:1 micro developer: deionised water for 75 s to remove the exposed photoresist.

(6) Reactive Ion Etching (RIE) using silicon tetrachloride (SiCl_4) was used for dry etching the side walls of the ribs of the optical waveguides. Laser reflectometry [8] was used to measure the real time etch rate of the layers. The final etch depth was 0.8 μm and the typical etch rate was 150 nm/min.

(7) A new layer of photoresist (S1400-31) was spun onto the sample and baked at 90 °C for 20 minutes. Then the sample was soaked in chlorobenzene for 15 minutes and baked at 90 °C for another 20 minutes. The use of thicker resist and chlorobenzene facilitate the lift-off of thick layers of metal. The sample was aligned and exposed for 12 seconds and then developed and washed. Before the p-type contact was deposited, the sample was etched in ammonia solution for one minute to remove any surface oxidation of the P^+ GaAs contact layer. A Ni/Au (70 nm of nickel and 150 nm gold) contact layer was evaporated onto the sample at a vacuum pressure of 2×10^{-6} torr. The sample was then soaked in acetone until all the metal on top of the photoresist had lifted off.

(8) Photolithography: Repeat step 2

(9) The second mask, which was used to protect the ridges from etching, was aligned and placed in contact with the sample using mask aligner, and the sample was exposed to UV light and then developed to remove the exposed photoresist.

(10) Wet etching with a solution of 1:8:1 sulphuric acid: hydrogen peroxide: water was used to mesa between ribs to isolate individual devices. Rinse sample in R. O. water afterward and blown dry.

(12) The sample was mounted on a block with wax and thinned to 200 μm using 9 μm alumina grit (Al_2O_3). The backside of the sample was thinned down using 3 μm alumina grit to reduce the substrate thickness to about 150 μm . This stage facilitate device cleaving and improve characteristics (reduce series resistance and improve heat sinking).

(13) The sample was immersed in organic solvents: trichloroethane for 30 minutes, methanol for 10 minutes, acetone for 10 minutes in this order to remove any wax deposits. This process was done in refluxing condenser with boiling solvents. It was followed by R. O. water and then blown dry. Cleaning in an ultrasonic bath is not advisable for metallised and thinned samples since it deteriorates the metal adhesion and it may also break the samples.

(14) The sample was mounted on a glass slide with resist for easy handling during etching and subsequent metal evaporation, and to protect the top from the etchant. The sample was etched with ammonia diluted in water (NH_3 —1, H_2O —2) for one minute. Then, the n-type contact was deposited using a standard "mike ohm" recipe (14 nm of gold, 14 nm of germanium, 14 nm of gold, 11 nm of nickel and 200 nm of gold) at a vacuum pressure of 2×10^{-6} torr.

(15) Sample cleaning: as step 13.

(16) The contacts were annealed in a Rapid Thermal Annealer (RTA) at 360 °C for 60 s to obtain a good ohmic contact. During processing, the RTA chamber was evacuated and purged with N₂ to prevent contamination.

(17) The waveguides could then be cleaved. This was done by making a small nick in the sample in the desired cleavage direction using a diamond stylus, and then carefully applying pressure to the sample so that it cleaved along the crystal planes, to achieved a mirror-like facet.

Fig. 3.10 shows Scanning Electron Micrographs of the waveguides used for the experiments in this thesis, and it can be seen that the sidewalls are vertical.

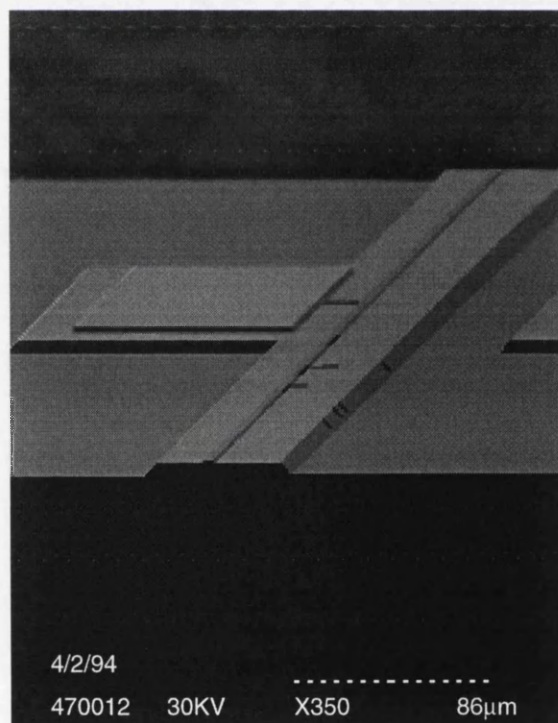


Fig. 3.10: S.E.M. of waveguide.

3.9 Conclusions

Single moded waveguides have been designed using Fourlay with the effective index method, and with F-Wave using a more accurate but much slower, finite difference technique for solving the vector electromagnetic equations. Also, fabrication methods used for the production of AlGaAs optical waveguides have been outlined.

3.10 References

- [1] H. Kogelnik, "Theory of dielectric waveguides" in Integrated Optics, ed. T. Tamir, Topics in Applied Physics, Springer-Verlag, 1979
- [2] D. L. Lee, "Electromagnetic principles of integrated optics", John Wiley & Sons, 1986.
- [3] J. J. G. M. Van Der Tol, N. H. G. Baken, "Correction to refractive index methods for rectangular dielectric waveguides", Electron. Lett., Vol. 24, pp. 208-209, 1988.
- [4] B. S. Bhumbra, "Non-linear optical waveguide devices in GaAs/AlGaAs", Ph.D. thesis, Dept. of Electronics and Electrical Engineering University of Glasgow, 1990.
- [5] S. Adachi, "GaAs, AlAs, and $\text{Al}_x\text{Ga}_{1-x}\text{As}$: Material parameters for use in research and device applications", J. Appl. Phys., Vol. 58, pp. 62-89, 1985.
- [6] J. Wilson and J. F. B. Hawkes, "Optoelectronics: An introduction", Prentice-Hall International Series in Optoelectronics, 1983.
- [7] A. Yariv, "Optical electronics", Fourth Edition, Saunders College Publishing, 1991.
- [8] S. E. Hicks, W. Parks, J. A. H. Wilkinson and C. D. W. Wilkinson, "Reflectance modelling for In-situ dry etch monitoring of SiO_2 and III-V multilayer structures", J. Vac. Sci. Technol. B, Vol. 12, pp. 3306-3310, Dec. 1994.

Chapter 4

Two Photon Absorption Waveguide Autocorrelator and Photodetector

This chapter initially presents indirect optical pulse width measurements, i.e. intensity and interferometric autocorrelations, carried out using the waveguide autocorrelator. The TPC autocorrelator was initially used to observe an interferometric autocorrelation of a mode-locked Nd³⁺:YAG laser. Intensity and interferometric autocorrelations were then taken of a mode-locked Nd³⁺:YLF laser, for the first time using a waveguide autocorrelator. The polarisation dependence of two photon absorption in the waveguide autocorrelator is then discussed. Finally ultra-fast optical thresholding based on waveguide photodetectors is described.

4.1 Introduction

In order to measure the duration of ultra-short laser pulses, various autocorrelation techniques have been developed [1, 2]. Measurements have been made by means of second harmonic generation (SHG) [3], two photon fluorescence [4] and, also, two photon conductivity (TPC) in commercial photodiodes [5]. The efficiency is substantially improved by employing the photodiode in a waveguide geometry [6]. Such a device has a number of advantages over conventional second harmonic autocorrelation: (1) two photon absorption has a much broader wavelength response than the phase-matching necessary for SHG, (2) the detection and non-linear response functions are integrated into a single device, (3) increases the sensitivity of the measurement due to the increase non-linear interaction length, (4) semiconductor photodiodes are relatively inexpensive and (5) a waveguide device is particularly suited for an optical fibre input. Using a waveguide, however, may have the disadvantage that some temporal resolution is lost due to dispersion.

The simplest and most direct method of recording the temporal intensity profile of a laser pulse is provided by the photodetector-oscilloscope combination, which has the advantage of being able to measure any pulse train without the need of a triggering source. The main disadvantage of this technique, however, is its time resolution, which is determined by the detection bandwidth of the photodetector and the rise time of the sampling oscilloscope, and is at best of the order of 10 ps. If a better time resolution is required, an electron-optical streak camera may be used. Although, streak cameras are versatile tools, capable of measuring laser pulses with subpicosecond time resolution, they are quite expensive. So indirect optical pulse width measurements, i.e. intensity and interferometric autocorrelations, have been developed. These techniques are simple, inexpensive and can provide extremely high time resolution, down to tens of femtoseconds. In interferometric autocorrelation, the envelope of constructive interference has a peak to background ratio of 8:1 (against 2:1 for conventional intensity autocorrelations), because the intensity of the second harmonic is related to the fourth power of the electric field amplitude [7]. Therefore, interferometric autocorrelations are very sensitive to the exact pulse shape, unlike intensity autocorrelations where all phase information is averaged out [8]. Since the waveguide autcorrelator allows for both the intensity and interferometric autocorrelation measurements to be carried simply in one device, it would be possible to totally recreate the pulse if a measurement of the optical spectrum is taken [9].

However, we must first examine the structure of ultra-short pulses before looking at pulse measurement techniques.

4.2 The Structure of Ultra-short Pulses

We consider first the mathematical description of optical pulses and define the terms involved to form a basis to understand how to measure ultra-short pulses.

The magnitude of the electric field vector of a plane wave optical pulse at a fixed point in space may be expressed as the Fourier integral [10]:

$$E(t) = \frac{1}{\sqrt{2\pi}} \int_{-\infty}^{+\infty} e(\omega) \exp(-i\omega t) d\omega \quad (4.1)$$

The Fourier inversion yields:

$$e(\omega) = \frac{1}{\sqrt{2\pi}} \int_{-\infty}^{+\infty} E(t) \exp(+i\omega t) dt \quad (4.2)$$

In most applications of wave theory, it is convenient to integrate over positive frequency components only. To do this a complex function $V(t)$ is defined such that $E(t) = \text{Re}[V(t)]$. This leads to:

$$\begin{aligned} V(t) &= \frac{1}{\sqrt{2\pi}} \int_0^{+\infty} 2 e(\omega) \exp(-i\omega t) d\omega \\ V(t) &= \frac{1}{\sqrt{2\pi}} \int_{-\infty}^{+\infty} v(\omega) \exp(-i\omega t) d\omega \end{aligned} \quad (4.3)$$

where V is the amplitude of the electric field vector and $v(\omega)$ is:

$$\begin{aligned} v(\omega) &= \frac{1}{\sqrt{2\pi}} \int_{-\infty}^{+\infty} V(t) \exp(i\omega t) dt \\ &= 2 e(\omega) \quad (\omega > 0) \\ &= 0 \quad (\omega < 0) \end{aligned} \quad (4.4)$$

Note since $E(t)$ is real, $e(-\omega) = e^*(\omega)$.

The complex functions $V(t)$ and $v(\omega)$ define an optical pulse in the time and frequency domains, respectively. These functions can be simply expressed in terms of their modulus and argument and we therefore write for $v(\omega)$:

$$v(\omega) = a(\omega) \exp(i\phi(\omega)) \quad (4.5)$$

where $a(\omega)$ and $\phi(\omega)$ are called the spectral amplitude and spectral phase respectively. Optical pulses normally satisfy the quasi-monochromatic condition that $a(\omega)$ is significant only in a frequency band $\Delta\omega$ which is narrow compared with the mean frequency ω_0 . In this case it is appropriate to write the equations in the time domain

$$V(t) = v(t) \exp(-i\omega_0 t) \quad (4.6)$$

where

$$v(t) = A(t) \exp(i\phi(t)) \quad (4.7)$$

The modulus and argument of v are the temporal amplitude and phase respectively. In the quasi-monochromatic case, both $A(t)$ and $\phi(t)$ are slowly varying functions of time and represent the amplitude and phase of the carrier wave [11].

The instantaneous intensity $I(t)$ can be defined as :

$$I(t) = V(t) V^*(t) = A^2(t) \quad (4.8)$$

Note that, in general, $I(t)$ is not strictly proportional to the square of the real field $E(t)$, but in the quasi-monochromatic case, over a few optical cycles[12]:

$$\frac{1}{2} I(t) = \langle E^2(t) \rangle_{\text{time}} \quad (4.9)$$

Similarly the spectral intensity $i(\omega)$ is given by:

$$i(\omega) = v(\omega) v^*(\omega) = a^2(\omega) \quad (4.10)$$

From Parseval's theorem, the total energy of the pulse is proportional to the area under either the temporal or spectral intensity profile.

$$\int_{-\infty}^{+\infty} I(t) dt = \int_0^{+\infty} i(\omega) d\omega \quad (4.11)$$

Thus the structure of a pulse is completely defined by a phase and an amplitude.

Whilst these can be referred to the time or frequency domain and inter-related by Fourier transformation, there is not a one to one correspondence between the two intensity profiles $I(t)$ and $i(\omega)$ since each depends not only on the other but also on the associated phase function. There is a general relationship between the FWHM values of $I(t)$ and $i(\omega)$, i.e. Δt and $\Delta\omega$, which are related by the inequality:

$$\frac{\Delta\omega \Delta t}{2\pi} (\equiv P) \geq K \quad (4.12)$$

or $\Delta\nu \Delta t (\equiv P) \geq K \quad (4.13)$

where K is a constant of the order of unity and depends on the shape of the spectral intensity distribution. The shortest pulse obtainable for a given spectral bandwidth is therefore:

$$\Delta t_{\min} = \frac{2\pi K}{\Delta\omega} \quad (4.14)$$

Such a pulse is said to be bandwidth or transform limited. The parameter P in (4.12) is called the time-bandwidth product and represents the extent to which the duration of a pulse exceeds the minimum value given by (4.13).

4.3 Methods of Detection and Measurement

Nanosecond (10^{-9} s) pulses can be measured by electronic means. The combination of a fast photodiode and sampling oscilloscope can measure pulses of the picosecond duration, but pulses of subpicosecond duration require optical measurement methods. Direct methods of pulse width measurement were discussed in Chapter one. Here, indirect methods will be discussed. One indirect method, which is commonly used to measure ultra-short pulses, is concerned with the study of the temporal intensity profile through its correlation functions.

4.4 Autocorrelation Techniques

The most commonly used method for measuring ultra-short pulse widths in high repetition rate pulsed laser systems is to use the correlation of two pulses. Correlations may be carried out in a variety of ways, each producing a distinctive correlation function. These functions may include background levels from uncorrelated signals, or be background free. The correlation technique employed may react slowly to the fast optical changes taking place during the correlation. All

information regarding phase is lost as a consequence. In order to retain phase information, the technique employed must be able to resolve fast optical variations. In practice this means the spatial variation during correlation must be resolved to about one tenth of the shortest wavelength involved [7].

The auto-correlation of two pulses is often carried out within a second harmonic generating crystal. This is necessary if an accurate measurement of pulse width is to be obtained. Any linear interferometer applied in pulse measurement records the auto-correlation function of the pulse amplitude [13]. The power density spectrum and the amplitude correlation function form a Fourier transform pair. Thus complete knowledge of one completely specifies the other. A spectrometer may be used to measure the power density spectrum. An instrument such as the Michelson interferometer may be used to measure the amplitude correlation function.

The linear interferometer can also be used to measure the coherence length and coherence time for a pulse. The coherence length is the difference in interferometer path lengths, over which the interference pattern is visible. The coherence time and the spectral bandwidth are related by the following:

$$\Delta\omega \Delta\tau_c \geq 2\pi \quad (4.15)$$

As was indicated earlier, this represents the lower limit of the possible measurement of pulse duration. One concludes that a measurement taken with a linear optical system can provide information establishing a lower limit to the pulse duration. In order to measure pulse widths accurately, a non-linear device such as an intensity autocorrelator may be used. However, even in this case, the measured pulse width depends to a degree on an assumption of pulse shape [8].

4.4.1 Linear Autocorrelation of Two Pulses

In this application the input pulse is split into two pulses of approximately equal amplitude by a beam splitter. Each pulse traverses one arm of a Michelson

interferometer which introduces a phase shift between the pulse pair proportional to the path difference in the arms. The pulses are directed to a square law detector, such as a photodiode, along a collinear path where they are recombined. The detector records the intensity of the combined signal which changes as the path difference between the arms is varied. A Michelson interferometer configuration is illustrated in Fig. 4.1.

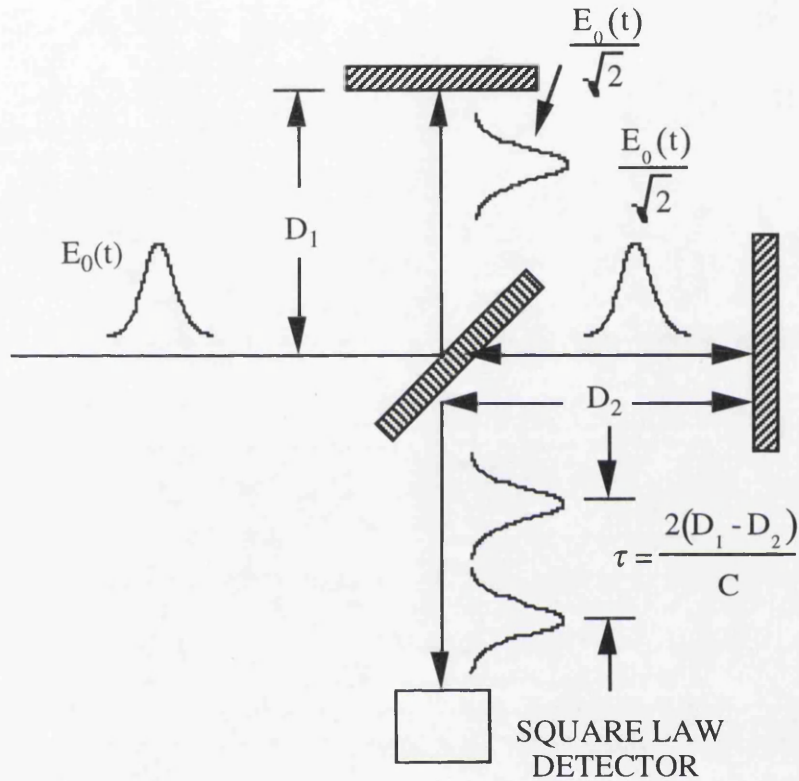


Fig. 4.1: Schematic diagram of a linear autocorrelation (after ref. [13])

Consider a pulse of amplitude $E(t)$ which is split into two pulses of equal amplitude $\frac{E(t)}{\sqrt{2}}$. Assuming a delay in time of τ between pulses, they may be represented by:

$$E_1(t) = \frac{E_0(t)}{\sqrt{2}} e^{i\omega t} \quad ; \quad E_2(t) = \frac{E_0(t - \tau)}{\sqrt{2}} e^{i\omega(t - \tau)} \quad (4.16)$$

It is assumed that $E_0(t)$ is a slowly varying pulse envelope with respect to the frequency ω . The detector records the intensity of the combined signal as follows:

$$I(t, \tau) = \frac{1}{2} [E_0(t) + E_0(t - \tau)]^2 \quad (4.17)$$

If the response of the detector is assumed to be slow in comparison to τ , the time delay, or $\Delta\tau$, the pulse width, the output from the detector is given by:

$$\begin{aligned} S(\tau) &= \int_{-\infty}^{+\infty} I(t, \tau) dt \\ &= W [1 + G(\tau)] \end{aligned} \quad (4.18)$$

where W is the pulse energy and $G(\tau)$ is the amplitude correlation function. In the above expression

$$W = \int_{-\infty}^{+\infty} E_0^2(t) dt \quad (4.19)$$

and

$$G(\tau) = \frac{\int_{-\infty}^{+\infty} E_0(t) E_0(t - \tau) dt}{\int_{-\infty}^{+\infty} E_0^2(t) dt} \quad (4.20)$$

When the time delay $\tau = 0$, $G(\tau) = 1$ and $S(\tau) = 2W$ and when the time delay τ is such that no overlap occurs then $S(\tau) = W$. Thus the signal to background ratio becomes 2:1.

4.4.2 Non-linear Autocorrelation—Slow Correlation

To carry out a slow correlation of two pulses, the above technique is modified as follows. The two pulses from each arm of the interferometer are rendered parallel but not collinear. They are then focused into a second harmonic generating crystal at a suitable phase matching angle. The second harmonic signal is then detected while the fundamental signal is filtered out. In the following analysis, it is assumed that the phase matching condition in the non-linear crystal is maintained over the entire bandwidth of the laser pulse and there is no inter-pulse radiation.

Let the two output pulses from the interferometer be $E_1(t)$ and $E_2(t)$. The second harmonic output field will be given by:

$${}^{2\omega}E(t) = [E_1(t) + E_2(t - \tau)]^2 \quad (4.21)$$

The output from a slow detector is given by:

$$\begin{aligned} S(\tau) &= \int_{-\infty}^{+\infty} |{}^{2\omega}E(t)|^2 dt \\ &= {}^{2\omega}W [1 + 2G(\tau)] \end{aligned} \quad (4.22)$$

Here ${}^{2\omega}W$ is the second harmonic pulse energy given by:

$${}^{2\omega}W = \int_{-\infty}^{+\infty} E^4(t) dt \quad (4.23)$$

$G(\tau)$ is the autocorrelation function of the pulse intensity given by:

$$G(\tau) = \frac{\int_{-\infty}^{+\infty} E^2(t) E^2(t - \tau) dt}{\int_{-\infty}^{+\infty} E^4(t) dt} \quad (4.24)$$

When the time delay $\tau = 0$, $G(\tau) = 1$, and the ratio $S(\tau):{}^{2\omega}W = 3:1$ and when the time delay is such that no overlap occurs, then the ratio $S(\tau):{}^{2\omega}W = 1:1$. Thus the signal to background ratio becomes 3:1. The duration of the pulse is obtained by measuring the duration of the autocorrelation function and dividing it by a factor, k , which depends on the assumed pulse shape. The validity of this assumed pulse shape can be checked by measuring the bandwidth of the pulse spectrum and comparing the duration-bandwidth product with the calculated value for the chosen pulse profile. This comparison is only valid for pulses having no frequency chirp. Calculated values for the Fourier transform-limited duration-bandwidth product $\Delta\tau_p\Delta\nu$, and the factor k for some common pulse shapes are presented in Table 4.1:

Pulse profile	I(t)	$\Delta\tau_p\Delta\nu$	τ_p/τ_G
sech ²	sech ² (t/τ)	0.3148	0.6482
Gaussian	exp (t ² /T ²)	0.4413	0.7071
Single-sided exponential	exp (-t/T) ; t≥0 0 ; t≤0	0.1103	0.5
Lorentzian	1/1+x ²	0.2206	0.5

Table 4.1: Transform-limited duration-bandwidth products and pulse width/autocorrelated width for some common pulse shapes [after ref. 14].

Unfortunately, since the autocorrelation function is symmetric, the information relating to the temporal profile of the pulse is lost. This makes the exact duration of the pulse ambiguous since it depends upon the pulse shape. There is also a lack of chirp information. The interferometric autocorrelation goes some way to solve the problem.

4.4.3 Non-linear Interferometric Autocorrelation-Fast Correlation

To reveal the fine structure in an ultra-short pulse, a more sensitive instrument than the intensity autocorrelator, which does not provide phase information, is required. If the correlation is carried out with interferometric accuracy, it may be possible, with the additional information provided by the intensity correlation and spectral analysis, to move closer to the true structure of the pulse [7, 8].

For a measurement carried out with interferometric accuracy, i.e. a fast correlation as described above, the output from the second harmonic generating crystal is produced by parallel and collinear pulse trains from the arms of the interferometer. The output in this case is given by [14]:

$$I(t) = \int_{-\infty}^{+\infty} \left| \left\{ E(t) e^{i[\omega t + \phi(t)]} + E(t - \tau) e^{i[\omega(t - \tau) + \phi(t - \tau)]} \right\}^2 \right|^2 dt \quad (4.25)$$

At zero delay, coherent superposition of the fields gives:

$$I(0) = 2^4 \int_{-\infty}^{+\infty} E^4(t) dt \quad (4.26)$$

The quadratic dependence of the autocorrelation on the electric field results in an increased contrast ratio of 8:1. Since this autocorrelation resolves individual optical cycles, it is sensitive to frequency chirp. Interferometric autocorrelation can detect frequency chirp in the pulse because changes in instantaneous phase (and hence carrier frequency) over the duration of the pulse will reduce the visibility of the fringes in the wings of the autocorrelation [15]. The shape of the interferometric autocorrelation function is very sensitive to the pulse shape and chirp. The pulse shape—in amplitude and phase—can be determined by simultaneously fitting the intensity autocorrelation, interferometric autocorrelation, and optical spectrum [8].

4.4.4 Interferometric Correlation and Pulse Shape

It has been suggested that an autocorrelation carried out with interferometric accuracy, can yield information regarding the fundamental nature of an ultra-short pulse train [8, 9]. In particular it can reveal the presence of 'chirp', i.e. frequency changing with time within the pulse. The upper envelope described by the interferometric maxima is much more sensitive to the incident pulse shape than a conventional autocorrelation since it depends on the fourth power of the electric field and on the phase of the combining fields. The form of the interferometric envelope can be related to the type of chirp within the pulse [7]. Interferometric autocorrelations can therefore provide information on the frequency and phase structure within a pulse.

4.5 Experiments

In this section the use of TPC in a reverse-biased AlGaAs waveguide is demonstrated as an autocorrelator detector. This waveguide was initially used to obtain the interferometric trace of pulses from a mode-locked Nd³⁺:YAG laser.

Intensity and interferometric autocorrelation measurements were then taken of pulses from a mode-locked Nd³⁺:YLF laser.

4.5.1 Nd³⁺:YAG Laser

The above laser is an yttrium aluminium garnet crystal doped with trivalent neodymium atoms. Its strongest line is in the infra-red at a wavelength of 1.06 μm . If it is run in the continuous wave (CW) mode, the output is essentially a random wave which fluctuates up and down due to the interference between the various modes of light vibration in the laser cavity. For the purposes of the experiment however, it was necessary to have the light arriving at the waveguide in short pulses so that we could measure their lengths.

Short pulses are produced by modelocking the laser, locking the phases of the different modes so that they have fixed phase relationships and interfere to produce pulses of high intensity at regular intervals. These pulses are emitted from the laser with a frequency that corresponds to the round-cavity trip time of the light, i.e. the time it takes the light to travel from one end of the laser to the other and back. In the particular Nd:YAG used here, laser they are produced at 76 MHz which corresponds to a spacing of 13 ns between them. Most arc-lamp pumped mode-locked Nd:YAG lasers are mode locked using an intracavity acousto-optic amplitude modulator and produce pulses whose length is in the region of 80-100 ps [16].

The laser was operated at a DC current of 31 A which corresponded to a maximum time averaged power output at the end of the laser of 8 W.

4.5.2 Device Fabrication

A p-i-n waveguide structure which consisted of an Al_{0.2}Ga_{0.8}As waveguide core surrounded by Al_{0.3}Ga_{0.7}As cladding regions, was grown by metal-organic vapour phase epitaxy (MOVPE). The upper and lower cladding layer thicknesses were 1 μm and 4 μm respectively, both sufficiently thick to ensure only a small

optical leakage into the cap and substrate. In order to reduce losses due to free carrier absorption, those parts of the cladding which were expected to have significant overlap with the optical mode were left undoped. Ridge waveguides 3 μm wide, 1 mm long, and separated by 100 μm were fabricated by dry etching; a wet etch was used to mesa between the ribs and isolate the individual devices electrically, as shown in Fig. 4.2. The individual devices were etched to a depth of about 5 μm , which reduced the dark current to about -40 pA at -5 V. The dark current is the reverse saturation current that flows at a specified reverse bias without incident light (it is important that the dark current is as small as possible in order to increase the sensitivity of the autocorrelator, i.e. decreasing the dark current improves the noise performance). The square pad attached to the side of the waveguide is an extension of the p-type ohmic contact on the top of the waveguide, necessary because it is impossible to probe the ohmic strip contact.

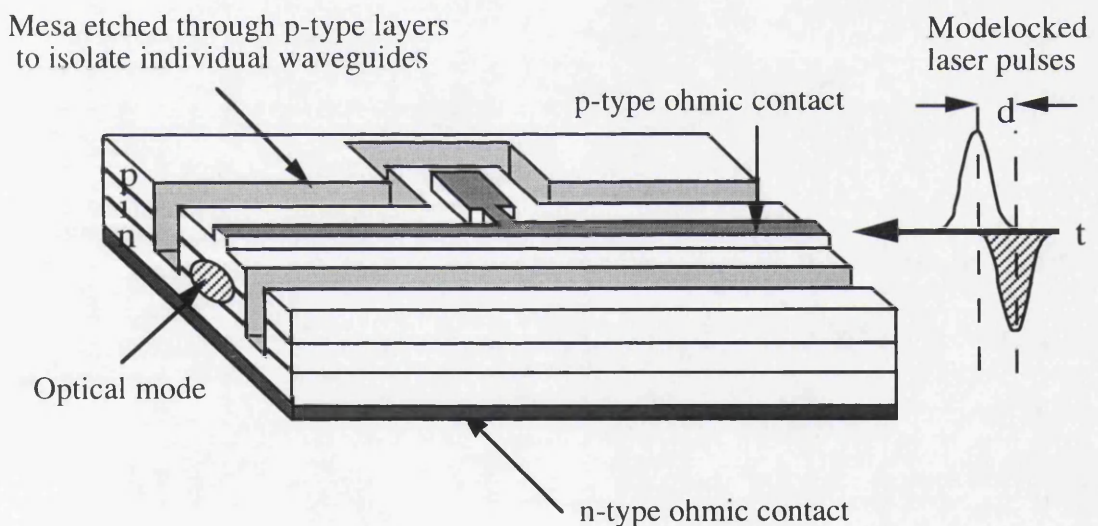


Fig. 4.2: Schematic of a TPA waveguide autocorrelator

4.5.3 Testing the Waveguides

Laser light was end-fired coupled into the waveguides using a microscope objective. In order to optimise the coupling efficiency into the waveguide mode, the overlap integral between the mode profile of laser beam and that of the waveguide must be maximised. The output from the waveguide was collected by another

microscope objective. The coupling efficiency is extremely sensitive to the position of the lenses, and so the lenses were mounted on translation stages with differential drives whose resolution was about $0.1 \mu\text{m}$. Both the input and output lenses could be independently adjusted to optimise focusing and alignment, and the sample could also be translated and rotated independently of the lenses. When aligning a waveguide, the output light was sent to an infra-red camera. With this particular experimental arrangement it is easy to monitor the intensity in the waveguide and hence to optimise the coupling efficiency, and also the mode profile.

The waveguide had been designed to be a single moded to ensure interferometric autocorrelation is possible, to eliminate intermodal dispersion, to ensure good optical overlap between pulses from interferometer, and to maximise the peak intensity under the ribs. The order of transverse mode depends on the rib width and Fig. 4.3 shows examples of a single- moded and a double- moded waveguide.

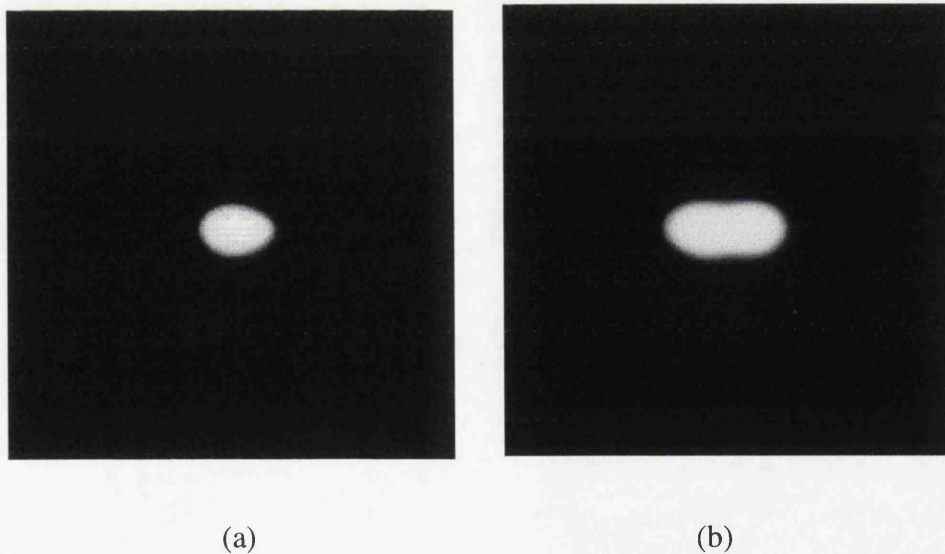


Fig. 4.3: Photographs of the output beam from (a) a single-moded and (b) a double-moded waveguide.

4.5.4 Single Beam Measurements of a Nd³⁺:YAG Laser Pulses

To test the correct operation of the device, single beam experiments were carried out initially. A single beam from the mode-locked Nd³⁺:YAG laser was end-fire coupled into the waveguide, which was reverse-biased by 4.5 V. The photocurrent produced was found by measuring the voltage across a 1 k Ω resistor, which was placed in series with the waveguide, using a lock-in amplifier. The photocurrent was found to be extremely sensitive to the degree of coupling of the laser beam into the guided mode, and to the quality of mode locking. Using both mode-locked and CW laser beams in turn, the average photocurrent was measured as a function of the average input power of the beam, and the resulting graph is shown in Fig. 4.4.

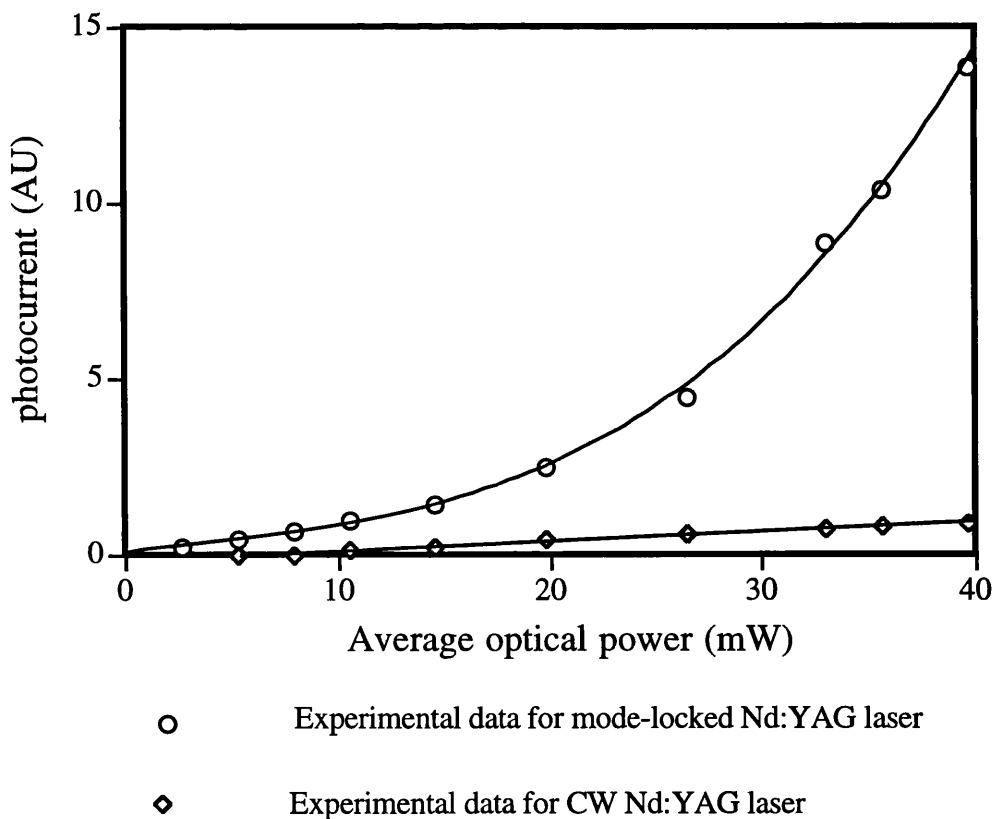


Fig. 4.4 : Optical power dependence of the photoconductivity of the waveguide.

For the CW case, the photocurrent is directly proportional to the optical power. This is because there is still some residual one photon absorption. The photocurrent for the mode locked case is, however, greater due to the higher peak power in the waveguide, making TPA the dominant effect. Because the conductivity is governed by a two photon effect, there is now a quadratic relationship between the photocurrent and the average optical power in the waveguide.

4.5.5 Interferometric Autocorrelation of a Nd:YAG Laser Pulses

The arrangement that was first used for the interferometric autocorrelator is shown in Fig. 4.5. The input pulse is split into two pulses of equal amplitude by a beam splitter. Each pulse tranverses one arm of a Michelson interferometer and a phase shift is introduced between the pulse pair proportional to the time delay in the arms. Then, both beams are recombined and made incident on the waveguide. In order to carry out the interferometer measurements, both beams have to be parallel and collinear. As the speaker is vibrated, the time delay between the pulses in each arm of the autocorrelator changes. The magnitude of the two photon absorption in the waveguide is dependent on the instantaneous peak intensity present, and will be greater when the two pulses exactly overlap. Since the number of free carriers in the waveguide is dependent on the amount of two photon absorption, the photocurrent measured by a lock-in amplifier will also vary depending on the time delay between the pulses in each arm. The acquisition time of the lock-in amplifier was not fast enough to measure the changing photocurrent from the p-i-n waveguide so it was replaced with a amplifier. The signal from the amplifier was applied directly to the Y-axis of the oscilloscope and the X-scan of the oscilloscope was connected to the oscillator used to vibrate the speaker so that, as the speaker was vibrated, a set of interference fringes could be displayed on the oscilloscope.

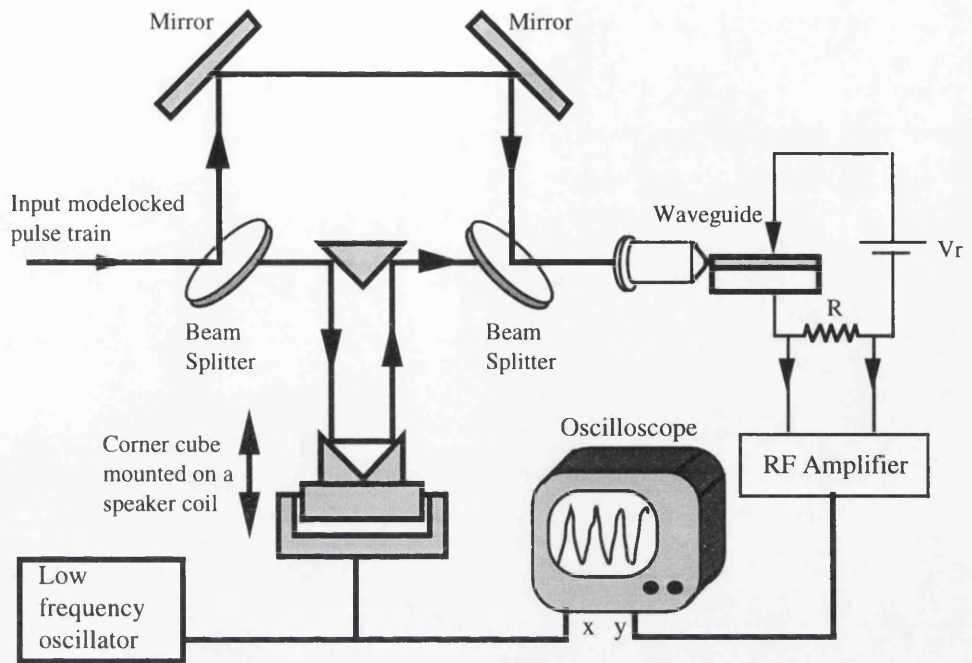


Fig. 4.5: Interferometric autocorrelation arrangement.

The 12 cm diameter speaker was driven by an sine wave generator at frequency of 20 Hz. The maximum stroke obtainable with this particular speaker was 2 mm (peak-to-peak travel) which corresponds to a maximum dynamic range of 13 ps, Fig. 4.6 (a)

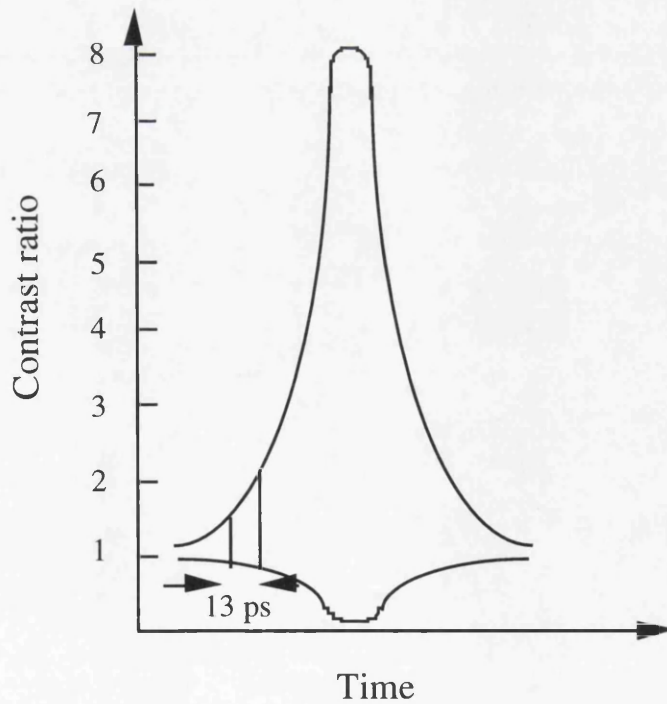


Fig. 4.6 (a): Fast autocorrelation trace with indication of 13 ps of pulse width.

This meant that only a small portion of the interferometric autocorrelation from the mode-locked Nd:YAG laser was observed. Fig. 4.6 (b) shows an interferometric autocorrelation trace of the central part of the optical pulse.

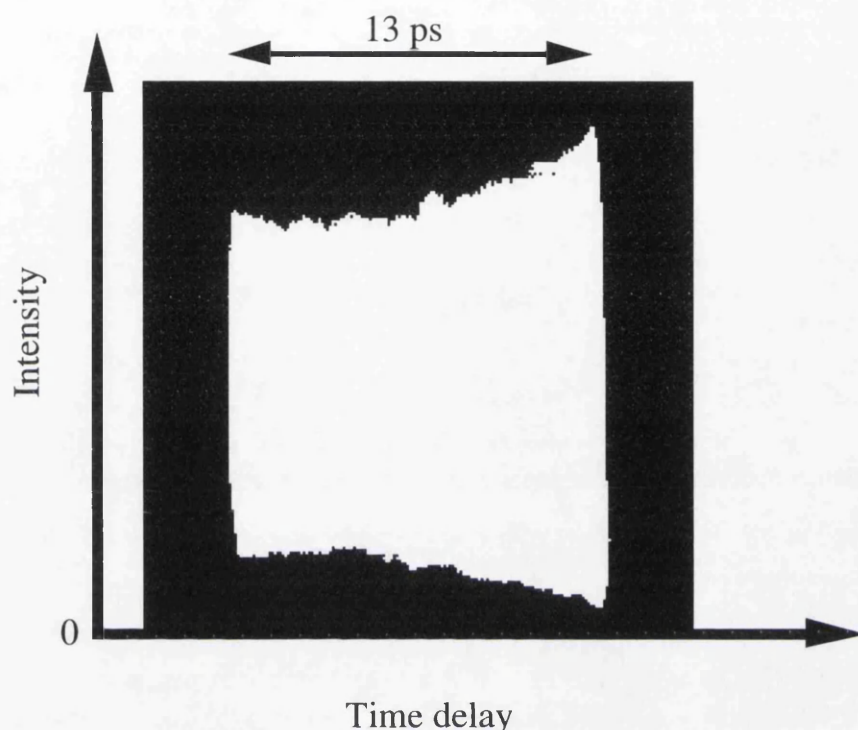


Fig. 4.6 (b): An interferometric autocorrelation trace of a Nd:YAG laser pulse train.

4.6 Autocorrelation Measurements of Nd:YLF Laser Pulses

Yttrium lithium fluoride (YLF) is the best known alternative to YAG as a neodymium lattice host. The Nd³⁺:YLF laser is an attractive medium for a mode-locked diode—pumped laser as it offers high efficiency combined with a relatively large gain bandwidth, more than twice that of the Nd³⁺:YAG laser, therefore yielding shorter pulses [17].

Both intensity and interferometric autocorrelation trace of a mode-locked diode-pumped Nd³⁺:YLF laser operating at 1.047 μm were successfully obtained by using an AlGaAs optical waveguide as the non-linear detection element of an autocorrelator.

4.6.1 Single Beam Measurements of a Nd³⁺:YLF Laser Pulses

Single beam measurements were made initially to check the operation of the device. Mode-locked pulses with a full width at half maximum of 16.3 ps from a Nd³⁺:YLF laser were end-fire coupled into the ridge waveguide, which was reverse-biased by 4.5 V. As before 1 kΩ resistor was placed in series with the waveguide, and the photocurrent was found by measuring the voltage across the resistor using a lock-in amplifier. Using both mode-locked and CW laser beams in turn, the average photocurrent was measured as a function of the average input intensity of the beam, and the resulting graph is shown in Fig. 4.7.

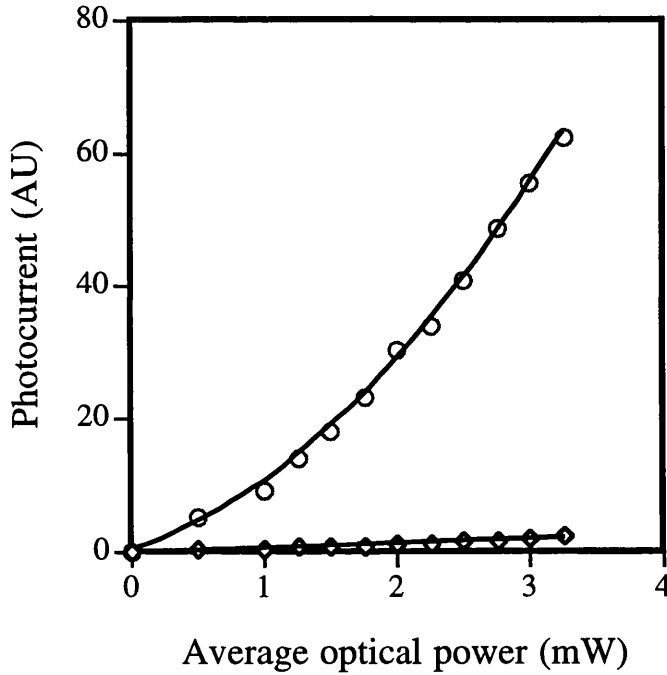


Fig. 4.7: Optical power dependence of the photoconductivity of the waveguide
The open points ◇ are experimental data for a CW Nd:YLF laser and the open points ○ are for the same laser mode-locked. The solid line and a parabola are fitted to the experimental points for CW and mode-locked cases, respectively.

The shape of these plots can be easily explained. For a single CW beam, the average photocurrent is given by [6]:

$$(J_{ph})_{CW} = e\Omega \left(\frac{\alpha}{h\nu} I_{ave} + \frac{\beta}{2h\nu} I_{ave}^2 \right) \quad (4.27)$$

where e is the electronic charge, Ω is the volume in which the photogenerated carriers are created, $h\nu$ is the photon energy, I_{ave} is the intensity of the beam, β is the two photon absorption coefficient, and α is the one photon absorption coefficient, which is that fraction of the total waveguide propagation loss resulting from the generation of electron-hole pairs by single photons.

The average photocurrent for the mode-locked beam is given by:

$$(J_{ph})_{ml} = e\Omega \left(\frac{\alpha}{h\nu} I_{ave} + \frac{\beta t_p}{2\sqrt{\pi} h\nu T} I_{ave}^2 \right) \quad (4.28)$$

where t_p is the time between mode-locked pulses, and T is the duration of the laser pulses. It is clear that the linear terms in the expressions for the photocurrent are identical for both the CW and mode-locked laser beams. However, the quadratic terms are seen to vary by a constant factor determined by the laser pulse mark to space ratio.

An experimental fit was obtained from equations (4.27) and (4.28). The values used being $\alpha = 0.038 \text{ cm}^{-1}$, $\beta = 1.6 \times 10^{-10} \text{ m/W}$, $t_p = 12.86 \text{ ns}$, $T = 17.7 \text{ ps}$, and $\Omega = 4.2 \times 10^{-15} \text{ m}^3$. It can be seen that, as expected, the photocurrent for a CW beam is a linear function of the intensity, and that the relationship is quadratic for a mode-locked beam.

4.6.2 Intensity Autocorrelation of a Nd³⁺:YLF Laser Pulses

The experimental set up for the intensity autocorrelation measurements is shown in Fig. 4.8. Optical pulses were generated by a mode-locked diode-pumped Nd³⁺:YLF laser operating at a wavelength of 1.047 μm and a repetition rate of 78 MHz. The full width half maximum (FWHM) duration of the optical pulses were measured using a conventional SHG autocorrelator to be 16.3 ps (assuming a Gaussian intensity profile). The average power transmitted through the waveguide was approximately 20 μW .

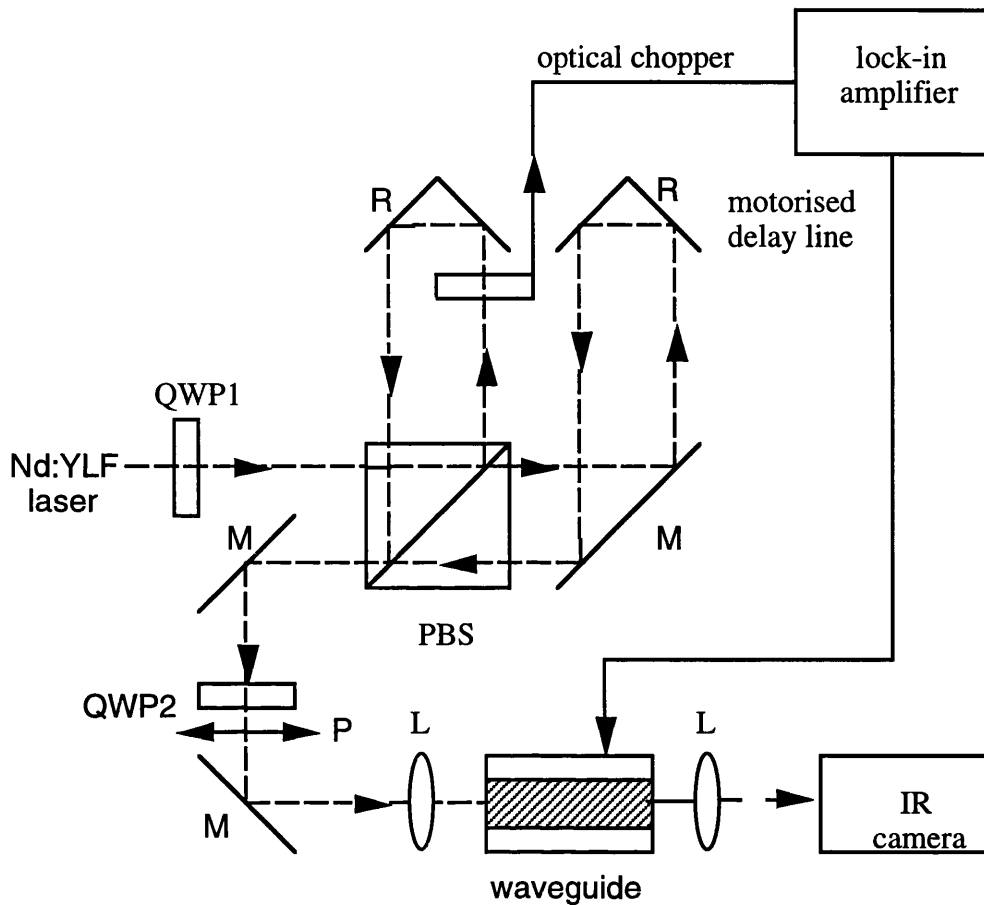


Fig. 4.8: Experimental set-up.

Keys: M: mirror, R: retroreflector, PBS: polarising beamsplitter, QWP: quarter wave plate, P: polariser, L: objective lens

The second quarter wave plate (QWP 2) and polariser were only used in the interferometric measurement.

The quarter wave plate in Fig. 4.8 made the pulses circularly polarised, thus enabling the polarising beamsplitter to divide the pulses equally into two orthogonal polarisations. The two orthogonally polarised pulses were recombined after one was delayed with respect to the other by the motorised variable delay line. The beam was then end-fire coupled into a reverse biased p-i-n waveguide, where the corresponding photocurrent was measured by a lock-in amplifier and hence the pulse width measured. An infra-red camera was placed at the end of the waveguide to aid alignment and to ensure that the light guided through the waveguide was in the zeroth order mode.

The intensity autocorrelation trace is shown in Fig. 4.9. The average autocorrelation photocurrent as a function of time delay between pulses is given by [6]:

$$I_{\text{ph}}(t_d) = e\Omega \left\{ \frac{2\alpha_{\text{SPA}}}{h\nu} I_{\text{ave}} + \frac{\beta t_p I_{\text{ave}}^2}{\sqrt{\pi} h\nu T} \left[1 + \exp\left(-\frac{t_d^2}{T^2}\right) \right] \right\} \quad (4.29)$$

where t_d is the time delay between the two pulses in the waveguide. It can be seen from the expression that, for Gaussian pulses, the average photocurrent has the same Gaussian dependence on the time delay between the two beams as a conventional SHG autocorrelator. Therefore any autocorrelation trace obtained from this method should be divided by $\sqrt{2}$ to obtain the true pulse width. An theoretical fit was obtained from equation 4.29 assuming a Gaussian pulse shape ($\alpha_{\text{SPA}} = 0.038 \text{ cm}^{-1}$ [18], $\beta = 1.57 \times 10^{-10} \text{ m/W}$), for which the FWHM of the mode-locked Nd³⁺:YLF laser pulses was calculated to be about 17.7 ps. Furthermore, the pulse peak power was less than 14 mW. This result is in close agreement with SHG autocorrelation measurement of the optical pulse of this laser (16.3 ps), the discrepancy being 8 % is within the experimental accuracy ($\pm 10 \%$). The TPA waveguide detector is, however, considerably more sensitive.

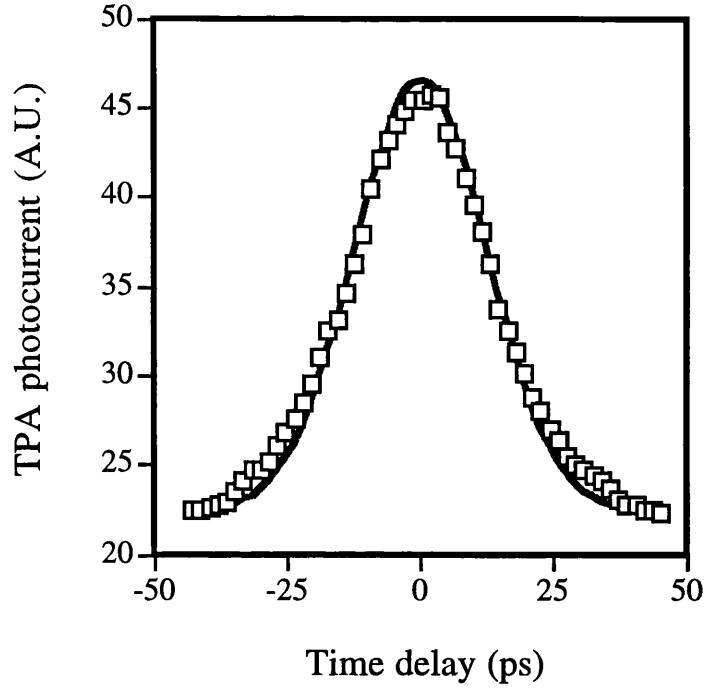


Fig. 4.9: Intensity autocorrelation trace of a Nd:YLF laser pulse train. The solid line is a theoretical fit assuming a Gaussian pulse shape.

Dispersion can degenerate the time resolution of these waveguide devices, and a useful parameter for indicating the length at which the effects of group velocity dispersion become important is the dispersion length given by [19]:

$$L_D = \frac{T_0^2}{|\beta_2|} \quad (4.30)$$

where β_2 is the group velocity dispersion with a value of $1.48 \text{ ps}^2/\text{m}$ [20], and T_0 is the $1/e$ duration of the pulse, which is related to the full width at half maximum duration by $T_{\text{FWHM}} = 1.655 T_0$ for a Gaussian pulse shape. If a Gaussian pulse is propagated through a waveguide of length z , it retains its shape but is broadened to:

$$T_{\text{out}} = T_{\text{in}} \left[1 + \left(\frac{z}{L_D} \right)^2 \right]^{1/2} \quad (4.31)$$

By using equations (4.30) and (4.31), it is calculated that the dispersion contribution from the waveguide could be discounted as the pulse dispersion length ($\approx 77 \text{ m}$) is far greater than the length of the waveguide (1 mm). The effects of dispersion are much

larger in the femtosecond regime, and the lower pulse width limit for a waveguide of this length is approximately 70 fs. However, by reducing the waveguide length the measurement accuracy can be kept high and, since pulses in the femtosecond regime typically have large peak powers there should be little reduction in sensitivity. Pulse broadening due to optical nonlinearities can also be discounted since the peak powers needed to observe these non-linear effects are extremely high (>10 W), and therefore non-linear self phase modulation would not be a problem if the input beam peak powers were limited appropriately.

4.6.3 Interferometric Autocorrelation of Nd³⁺:YLF Laser Pulses

Interferometric autocorrelation measurements, which provide phase information otherwise not available [8], were also made of the mode-locked pulses from the Nd³⁺:YLF laser using the TPA waveguide autocorrelator. In order to carry out the interferometric measurements, both beams have to be parallel and collinear. Therefore, the quarter wave plate 2, QWP 2, and a polariser were placed as shown in Fig. 4.8 to ensure that both beams had the same polarisations before being incident on the waveguide. To measure the interference effects between the two pulses, the movement of the translation stage has to be controllable to within at least 0.1 μm . The resolution of the translation stage was not adequate to move in such small increments and so, instead of the translation stage, the corner cube prism was attached to the cone of an audio speaker as before. This time a 20 cm diameter speaker was driven by a sine wave generator at a frequency of 60 Hz, and the maximum stroke obtainable with this particular speaker was 13 mm (peak-to-peak travel) which corresponds to a maximum dynamic range of 87 ps. Again the lock-in amplifier was replaced with a simple amplifier. The interferometric autocorrelation from the mode-locked Nd³⁺:YLF laser is shown in Fig. 4.10. As expected for an interferometric autocorrelation trace, a peak-to-background ratio of 8:1 was measured. The pulse duration was measured to be 17.7 ps (assuming a Gaussian intensity profile) which is in close agreement with the result using a conventional

SHG autocorrelator. Some weak frequency chirp on the pulses is also evident in the interferometric autocorrelation trace (Fig. 4.10) where the fringe visibility at the wings is reduced from what would be expected.

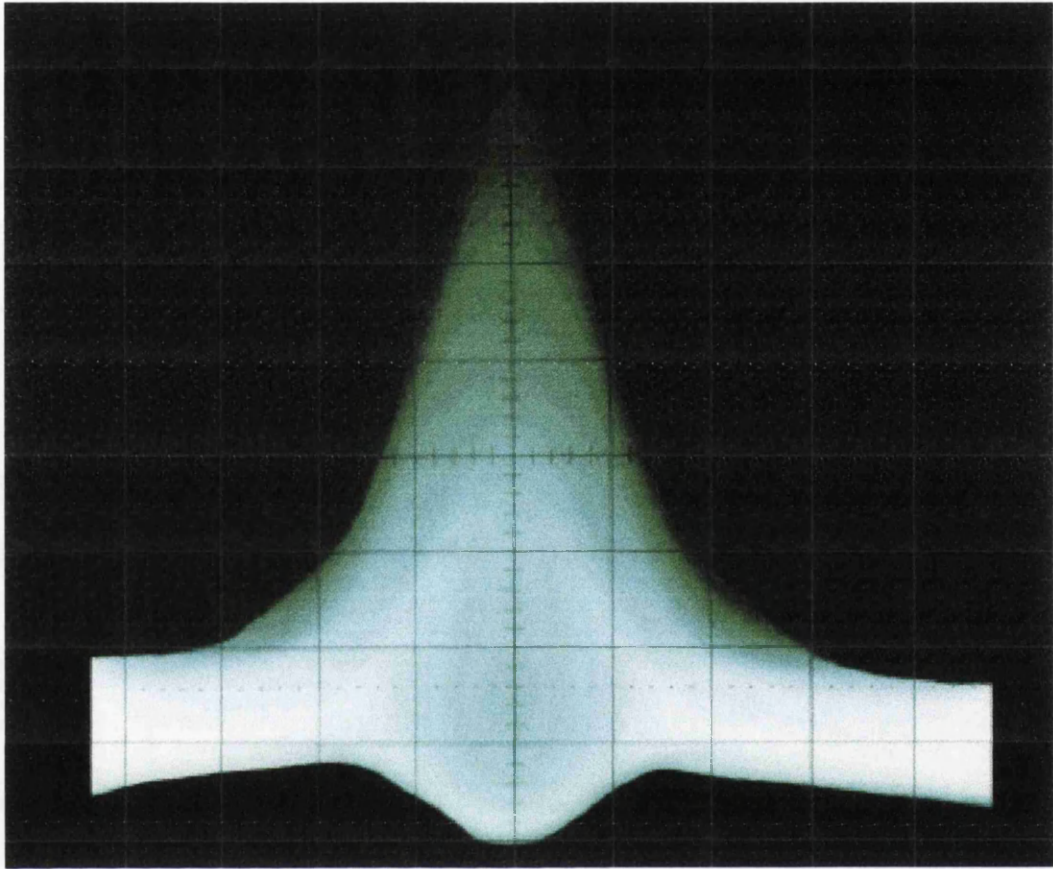


Fig. 4.10: Interferometric autocorrelation trace of a Nd:YLF laser pulse train. One horizontal division represents 9.6 ps.

4.7 The Polarisation Dependence of Two Photon Absorption Coefficient in a Waveguide Autocorrelator

4.7.1 Introduction

The importance of the anisotropy of the non-linear optical susceptibility tensors of materials has been recognised since the earliest investigations of intense laser radiation with matter. There has been much interest in the study of two photon absorption in semiconductor materials as non-linear elements in optical communication and information processing systems. Two photon absorption (TPA)

is widely acknowledged to degrade the performance of ultra-fast all optical switching devices [21-23].

Earlier calculations and measurements of TPA in zinc-blende semiconductor have concentrated on the linearly polarised single beam case (i.e. ignoring any polarisation dependence) [24]. It was, however, shown that there is a variation in the TPA coefficient depending on the relative orientation of the optical polarisation with crystalline axes for two beam experiments [25].

In this section, the complete polarisation dependence of the two photon absorption coefficient, β , has been obtained by measuring the orientational dependence and the contrast ratio of the photocurrent in a waveguide autocorrelator at an optical frequency far above the half-bandgap.

A TPA autocorrelator has two possible modes of operation. An interferometric autocorrelator requires that both the reference and time-delayed pulse are coherent and have the same polarisation (see section 4.4.3). Alternatively, an incoherent autocorrelation (often termed "slow") can easily be performed by launching the two pulses in orthogonal polarisations in the waveguide autocorrelator (see section 4.4.2). In such a geometry it is important to take account of the polarisation dependence of two photon absorption coefficient.

In semiconductor with cubic symmetry (zinc-blende), the polarisation dependence of degenerate (single wavelength) two photon absorption requires a total of three coefficients [26]

These are taken to be the TPA coefficient for linearly polarised light parallel to a crystal axis, $\beta^L[001]$ which is defined as:

$$\beta^L[001] = \frac{3}{2} \frac{\omega}{\epsilon_0 n_0^2 c^2} \text{Im} \chi_{xxxx}^{(3)} \quad (4.32)$$

where $\beta^L[001]$ is the TPA coefficient for radiation linearly polarised along the [001] orientation, c is the speed of light in vacuum, ϵ_0 is the permittivity of free space, n_0 is the linear refractive index, and $\text{Im } \chi_{xxxx}^3$ is the imaginary part of the third order susceptibility.

The anisotropy parameter σ'' which provides a variation with crystal orientation, is conventionally defined as:

$$\sigma'' = 2 \frac{\beta^L[001] - \beta^L[011]}{\beta^L[001]} \quad (4.33)$$

And the incremental dichroism parameter δ'' which provides a variation between linearly and circularly polarised light defined as:

$$\delta'' = \frac{\beta^L[001] - \beta^c(\theta_k = 0)}{\beta^L[001]} \quad (4.34)$$

where β^c is the circularly polarised TPA coefficient, θ_k is the corresponding angle which defines the radiation propagation direction K and $\theta_k = 0$ means that δ'' is defined parallel to crystal axis. The non-linear TPA coefficient for any polarisation orientation can be written in terms of these parameters. The TE and TM polarised beams and cross correlation beam were considered here, the TPA changes for which are given by:

$$\beta^L[110] = \beta^L[001] \left[1 + \sigma'' \left(\sum_i |e_i|^4 - 1 \right) \right] \quad (4.35)$$

$$\beta_x = \beta^L[001] \left[1 - \delta'' + \sigma'' \left(2 \sum_i |e_i|^2 |p_i|^2 - \frac{1}{2} \right) \right] \quad (4.36)$$

where e_i and p_i are the direction cosines along each crystalline axis of the unit polarisation vectors, and the summations take place over the crystal axes x , y , and z .

The normal orientation for a semiconductor waveguide has the TM mode polarised parallel to [001] and the TE mode polarised parallel to [110] crystalline directions. As a consequence the summation in equation 4.35 is equal to 1 for TM

and 1/2 for TE polarisation. The summation in equation 4.36 is zero for both orientations.

The optical loss for each component in this geometry is given by:

$$\begin{aligned}\frac{d I_{\text{TM}}}{d z} &= -\alpha I_{\text{TM}} - \beta^{\text{L}}[001] \left\{ I_{\text{TM}}^2 + \left(1 - \delta'' - \frac{\sigma''}{2} \right) I_{\text{TM}} I_{\text{TE}} \right\} \\ \frac{d I_{\text{TE}}}{d z} &= -\alpha I_{\text{TE}} - \beta^{\text{L}}[001] \left\{ \left(1 - \frac{\sigma''}{2} \right) I_{\text{TE}}^2 + \left(1 - \delta'' - \frac{\sigma''}{2} \right) I_{\text{TM}} I_{\text{TE}} \right\}\end{aligned}\quad (4.37)$$

where I_{TE} and I_{TM} are the irradiances for the TE and TM modes respectively and α is the total linear absorption coefficient. The total carrier generation rate is therefore,

$$\frac{d N}{d t} = \frac{\alpha_{\text{B}}}{\hbar \omega} (I_{\text{TE}} + I_{\text{TM}}) + \frac{\beta^{\text{L}}[001]}{2\hbar \omega} \left[I_{\text{TM}}^2 + \left(1 - \frac{\sigma''}{2} \right) I_{\text{TE}}^2 + 2 \left(1 - \delta'' - \frac{\sigma''}{2} \right) I_{\text{TM}} I_{\text{TE}} \right]\quad (4.38)$$

where α_{B} is the interband contribution to the linear absorption coefficient. Hence, by comparison of the carrier generation (i.e. photocurrent) for an input pulse launched in the TE and TM modes alone and an overlapping pulse launched in both TE and TM modes, the TPA ratios σ'' and δ'' can be determined.

4.7.2 Experiments

Measurements were performed on a p-i-n waveguide whose structure was explained in section 4.5.2. The optical source was a mode-locked diode-pumped Nd³⁺:YLF laser operating at a wavelength of 1.047 μm and a repetition rate of 78 MHz. The optical pulses were end-fire coupled into the reverse-biased p-i-n waveguide and the corresponding photocurrent was measured using a lock-in amplifier (see Fig. 4.8). The total optical loss at this wavelength was measured by Fabry-Perot technique and was found to be $\alpha = 1.76 \text{ cm}^{-1}$ [18]. By measuring the photocurrent at low irradiances the interband component of this was estimated to be $\alpha_{\text{B}} = 0.038 \text{ cm}^{-1}$ [18].

The anisotropy in the TPA coefficient was obtained by comparison of the photocurrent for equal irradiances launched in the TE or TM mode alone. Fig. 11 shows the power dependence of the photocurrent in both cases; the TPA coefficient is obtained from the second derivative of these curves.

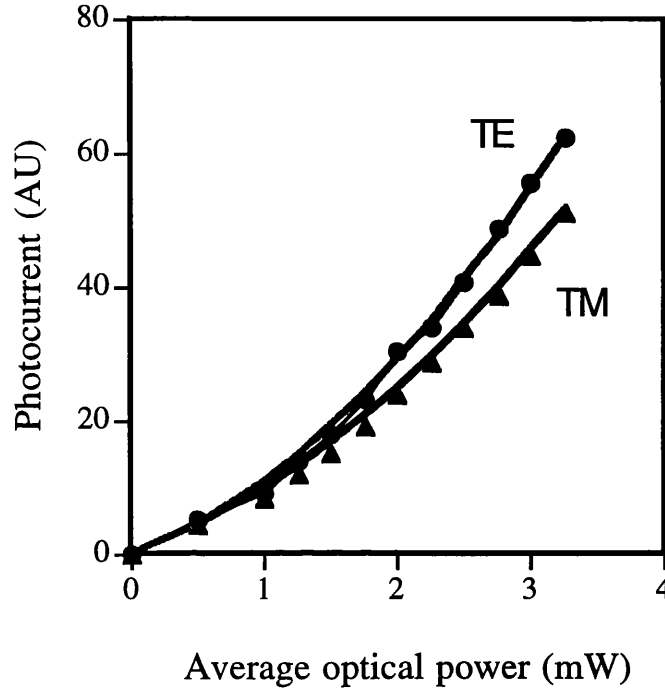


Fig. 4.11: Optical power (immediately before coupling into the waveguide) dependence of the photocurrent response for both TE and TM modes. The solid lines are a best fit to the data.

By taking the ratio of these values, a TPA anisotropy parameter $\sigma'' = -0.75$ is deduced. This compares well with picosecond nonlinear transmission measurements, $\sigma'' = -0.76$ [27], and $\sigma'' = -0.74$ [28], of GaAs at around the same wavelength, and with theoretical predictions, $\sigma'' = -0.9$, using a seven band model [26]. It should be noted that this calculation is based on band-structure data obtained at low temperatures, whereas the experimental values correspond to room temperature. Many early measurements of two photon absorption in semiconductors were inaccurate due to the influence of free carrier absorption [29]. One of the exceptions was the anisotropy measurement of van der Ziel [30] who used two photon excited fluorescence. The present measurement is similar in that it is also insensitive to free carrier absorption. However, the present technique also allows a value to be obtained

for the two photon absorption coefficient itself which is estimated at $\beta L_{[001]} = 1.2 \times 10^{-10}$ m/W. Note that the uncertainty in this figure is larger than in the ratios as the coupling efficiency cannot be determined to an accuracy better than a factor of 1.5.

The autocorrelation function of the waveguide photodiode was obtained by splitting the laser pulse into two arms and recombining them with a variable time delay and a rotation of the polarisation of 90° in one arm (Fig. 4.8). Figure 4.12 shows the measured dependence of the photocurrent against time delay. We adjusted the input optical power in each case and measured the transmitted power levels to be the same, to eliminate any differences in the input coupling efficiency between TE and TM modes.

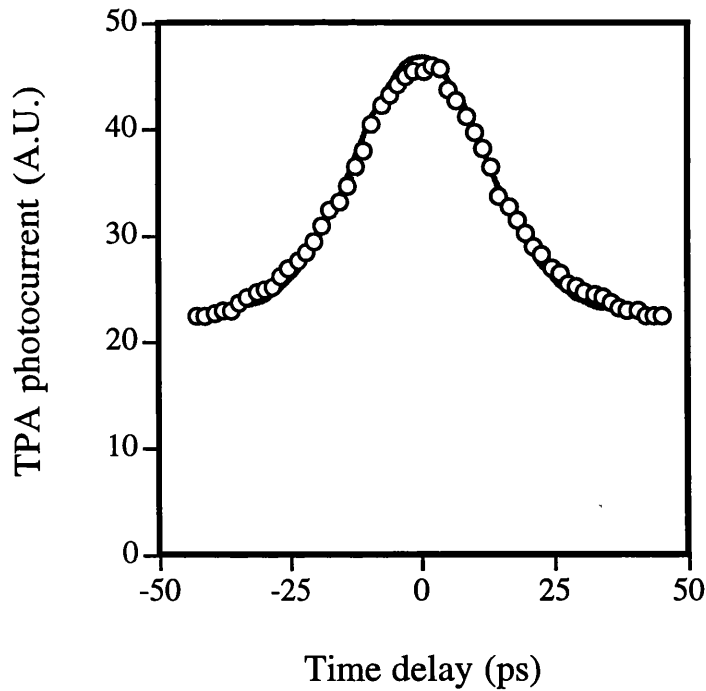


Fig. 4.12: Autocorrelation response of a Nd:YLF pulse train. The solid line is a theoretical fit assuming a Gaussian pulse shape

In calculating the theoretical photocurrent as a function of the time delay, The mode-locked pulses are assumed to have a Gaussian intensity profile, given by:

$$I(t) = I_0 \exp\left(\frac{-2t^2}{T^2}\right) \quad (4.39)$$

where I_0 is the peak intensity of the mode-locked pulse, related to the average intensity by:

$$I_0 = I_{\text{ave}} \sqrt{\frac{2}{\pi}} \frac{t_p}{T} \quad (4.40)$$

Because the beams are orthogonally polarised in the autocorrelation, there are no interference effects, and so the instantaneous intensity in the waveguide is given by:

$$I(t) = I_0 \exp\left(\frac{-2t^2}{T^2}\right) + I_0 \exp\left(\frac{-2(t-t_d)^2}{T^2}\right) \quad (4.41)$$

Hence, equation 4.38 can be integrated to obtain the number of carriers generated per pulse per unit length,

$$\frac{I_{\text{ph}}}{eL\nu_L} = \frac{\alpha_B}{\hbar\omega} (E_{\text{TM}} + E_{\text{TE}}) + \frac{\beta^L[001]}{2\sqrt{\pi}\hbar\omega\Gamma A_{\text{eff}}} \cdot \left[E_{\text{TM}}^2 + \left(1 - \frac{\sigma''}{2}\right) E_{\text{TE}}^2 + 2\left(1 - \delta'' - \frac{\sigma''}{2}\right) E_{\text{TM}} E_{\text{TE}} \exp\left(\frac{-t_d^2}{T^2}\right) \right] \quad (4.42)$$

where I_{ph} is the time-averaged photocurrent, L is the waveguide length, ν_L is the laser pulse repetition frequency, E_{TE} and E_{TM} are the pulse energies for the TE and TM polarisations respectively, A_{eff} is the effective area of the waveguide [31] and t_d is the time delay between the orthogonally polarised pulses. By fitting figure 4.12 to the experimental data, a pulse width of $T = 17.7$ ps is obtained for the mode-locked Nd:YLF laser pulses. Taking the pulse energies in both polarisations to be equal ($E_{\text{TE}} = E_{\text{TM}} = E$), the contrast ratio is then:

$$C = \frac{a + 4 - 2\delta'' - 3\sigma''/2}{a + 2 - \sigma''/2} \quad (4.43)$$

where $a = 4\sqrt{\pi}\alpha_B A_{\text{eff}} T / (\beta^L[001])$. Fig. 4.12 provides $C = 2.1$ which allows the incremental dichroism parameter to be determined, $\delta'' = 0.07$. This ratio is also consistent to equivalent values, $\delta'' = 0.1$, provided by theory [26], and non-linear transmission experiments, $\delta'' = 0.08$, in GaAs [27]. For comparison, an isotropic nonlinearity which obeys Kleinmann symmetry provides $\sigma'' = 0$ and $\delta'' = 1/3$. For

sufficiently intense pulses that the linear interband absorption is negligible ($a \approx 0$), this would give a maximum contrast ratio of $C = 2 - \delta'' = 5/3$. Hence the anisotropy of the cubic polarisation dependence of the nonlinearity increases the observed contrast ratio.

4.8 Ultra-fast Optical Thresholding based on Two-Photon Absorption GaAs Waveguide Photodetectors

In this section the measurements of the pulse width dependence of the two-photon absorption photocurrent in GaAs p-i-n photodetectors using subpicosecond optical pulses at 1.5 μm are discussed. We fabricated the waveguide detectors in Glasgow University and the experiments were done by Dr. Z. Zheng and Prof. A. M. Weiner in Purdue University in the U.S.A.

4.8.1 Introduction

All-optical signal processing can potentially be used for pattern matching applications in broad band optical networks. For example, in proposed coherent ultra-short pulse code division multiple-access (CDMA) systems [32], multiplexing would be achieved by assigning different, minimally interfering spectral phase codes to different transmitter-receiver pairs. The spectral coding process would stretch coherent femtosecond input pulses into picosecond duration pseudonoise bursts by using a pulse shaper to transfer a pseudorandom phase pattern from a spatial mask onto the spatially dispersed spectrum [33]. The receiver must then detect waveforms corresponding to the desired code while rejecting unwanted multiple-access interference. Code recognition could be accomplished by optical matched filtering followed by a non-linear optical thresholder. The decoding process could be realised by using a pulse shaper containing a phase mask conjugate to that used in the encoder. Correctly coded waveforms would be decoded into short and intense femtosecond pulses, while incorrectly coded waveforms would remain low intensity picosecond pseudonoise bursts (but with the same energy per pulse). The thresholder

would then distinguish between properly and improperly decoded signals using the contrast in their peak intensity. Although the non-linear optical response would need to be very fast, the electrical response of these devices could be as slow as the data per channel (\sim Gbit/s). A similar scheme could potentially be applied for header recognition in ultra-fast time-division networks.

Here we address experiments which demonstrate the feasibility of using two-photon absorption (TPA) in semiconductor waveguides as the nonlinear detector mechanism for such applications. As is well known, TPA is an instantaneous effect in which two photons (usually with energies below the bandgap) are absorbed simultaneously to generate a single electron-hole pair. In recent years TPA has begun to play an important role in ultra-fast guided-wave non-linear optics. As we mentioned earlier (see section 4.7.1), non-linear absorption induced by TPA has been recognised as one of the chief limiting factors in all-optical switching in semiconductor waveguides [21-23], and has also led to break-up of spatial solitons in glass waveguides [34]. In contrast to these deleterious effects, the non-linear photoconductivity associated with TPA has been applied for autocorrelation measurements of ultra-short pulses [6, 35].

Here the TPA-induced photocurrent in GaAs waveguides as a function of optical pulse width for pulses ranging from a few picosecond down to \sim 150 fs is investigated. The experiments reveal a strong pulse-width dependence of the photocurrent which can be used to approximate the desired ultra-fast thresholding function. Furthermore, it was demonstrated for the first time that these non-linear waveguide photodetectors can have sub-nanosecond electrical response times suitable for Gbit/s communications applications.

4.8.2 Waveguide Structure

The TPA waveguide detector used here was similar to those used in earlier experiments. The MOCVD-grown GaAs ridge waveguide was 1 mm long and 3 μ m

wide. It consisted of a p-i-n structure with a 0.6 μm thick GaAs (870 nm bandgap) layer sandwiched between $\text{Al}_{0.15}\text{Ga}_{0.85}\text{As}$ layers. For photons at 1.5 μm , there was little linear absorption but strong two photon absorption. The dark current at a typical -5 V bias was about 90 pA, which was negligible for the experiments.

4.8.3 Experiments

The experimental set-up is shown in Fig. 4.13. The experiments used 150 fs pulses at 1.5 μm wavelength and 80 MHz repetition rate from a Spectra Physics femtosecond optical parametric oscillator synchronously pumped by a mode-locked Ti:Sapphire laser. A polariser was used to set a horizontal input polarisation, and a stepper motor driven variable attenuator wheel was used to adjust the optical power. For some measurements, a mechanical chopper was used to enable lock-in detection. Light was coupled into the waveguide by using a 40 x microscope objective. Fresnel reflection from the uncoated front facet introduced 30% reflection loss of the input light.

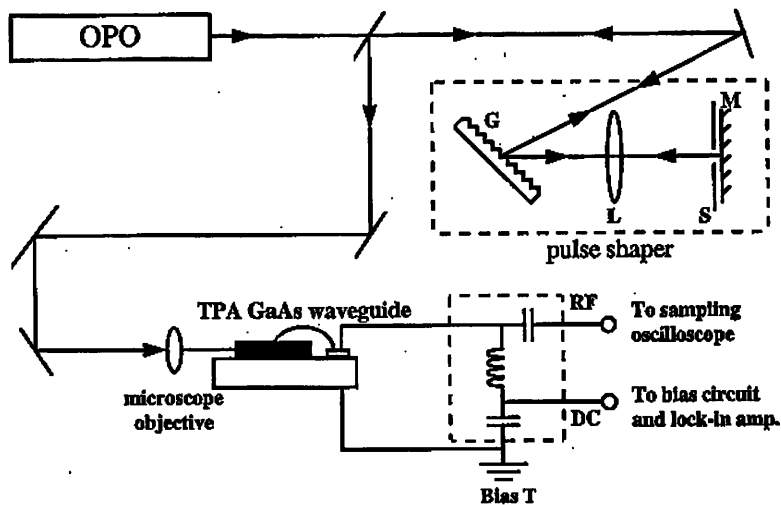


Fig. 4.13: Scheme of two photon absorption thresholding experiment. OPO: Ti:Sapphire laser pumped femtosecond optical parametric oscillator; G: 600 line/mm grating; L: achromatic lens; M: flat mirror.

For pulse width dependent measurements, the beam was sent into a double-pass pulse shaper [33] before it was coupled into the waveguide. The pulse shaper consisted of a 600 line/mm grating, an achromatic lens ($f=190$ mm) and a planar mirror placed in the focal plane of the lens. With the pulse shaper adjusted to the zero dispersion point and a variable slit placed just before the mirror, this worked as an adjustable pulse stretcher [33]. The slit acted as a spectral window, and its width adjusted to change the width of spectrum and hence the pulse width. Pulse width adjustment was accomplished with no spatial movement of the beam. Since the experimental results were very sensitive to any changes of coupling condition, this was crucial to get reliable data. The pulse width was measured by an autocorrelator.

The waveguide was reverse biased by a DC power supply connected through a bias tee. A probe was used to provide the electrical contact to the wire-bonded waveguide. A sampling oscilloscope and a lock-in amplifier were connected to the bias tee to measure the photocurrent time response and the average photocurrent, respectively.

Here it was assumed that the light remains undepleted so that intensity and carrier density are nearly constant throughout the length of the waveguide and also the pulses have a Gaussian shape [Equation (4.39)]. As previously mentioned, the average photocurrent is given by Equation (4.28).

When two photon absorption is the dominant effect and linear absorption is negligible, TPA photocurrent is expected to vary quadratically as the input average power changes. The equation 4.28 also predicts that the current linearly depends on the inverse pulse width

Fig. 4.14 shows a plot of the measured photocurrent as a function of average optical intensity, for a fixed 150 fs pulse width. The data clearly showed a quadratic dependence of the photocurrent to the optical average power, which is consistent both with the theoretical prediction above and with previous experimental results at

1.06 μm (Nd^{3+} :YAG laser wavelength) using ~ 100 ps pulses and 1.047 μm (Nd^{3+} :YLF laser wavelength) using ~ 17 ps pulses. Assuming that roughly 10% of the light was coupled into the waveguide, the corresponding average intensity in the waveguide ranges from 9×10^6 to 1.2×10^8 W/m^2 .

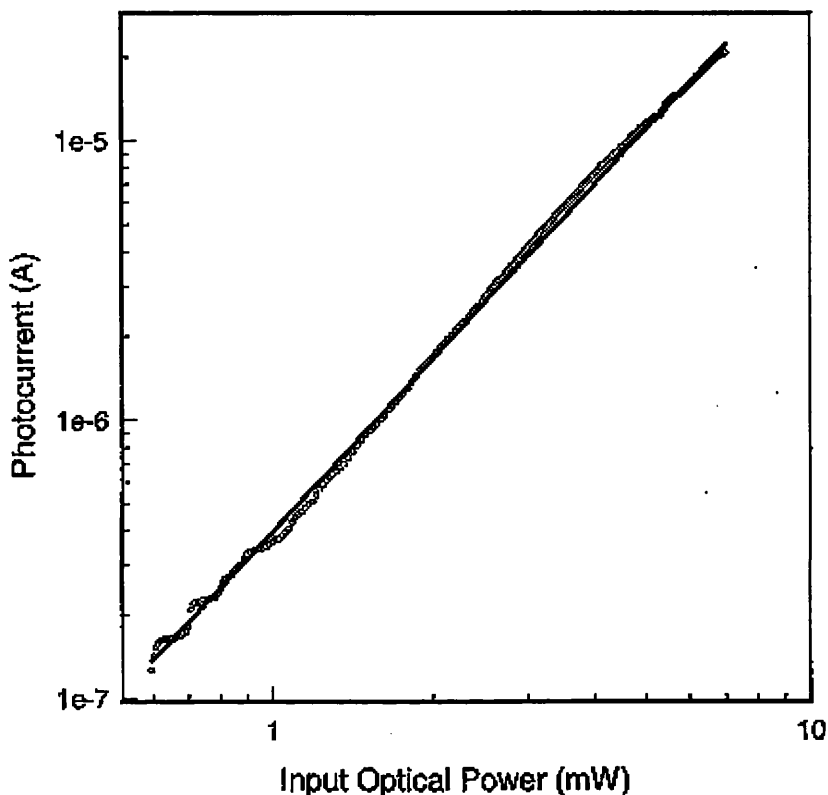


*Fig. 4.14: Intensity dependence of TPA photocurrent of GaAs waveguide.
 o: experimental data for 150 fs OPO.
 —: straight line fitted to experimental points.*

From the magnitude of the measured photocurrent, β is estimated to be $\sim 0.1 \times 10^{-10}$ m/W (assuming 100% collection efficiency for the photogenerated carriers). This is significantly lower than the value $\beta = 2.4 \times 10^{-10}$ m/W measured in [36] for a GaAs waveguide at 1.5 μm , $\beta = 2 \times 10^{-10}$ m/W measured at 1.06 μm [6], and $\beta = 1.2 \times 10^{-10}$ m/W estimated at 1.047 μm for an AlGaAs waveguide in Section 4.7.2, this Chapter, but is close to the value measured for $\text{Al}_{0.18}\text{Ga}_{0.82}\text{As}$ at

1.5 μm ($\beta = 0.09 \times 10^{-10}$ m/W) [37]. Since the waveguide consists of a sandwich of GaAs and $\text{Al}_{0.15}\text{Ga}_{0.85}\text{As}$ layers, the results here are in reasonable agreement with previous measurements. It is noted that there is some uncertainty in our estimation of β due to the difficulty in accurately measuring the power coupled into the waveguide. Experiments with InGaAsP waveguides at 1.5 μm have indicated a substantially larger β compared to the current devices, presumably due to the lower bandgap of InGaAsP [38]. Such an enhancement in β would provide good signal levels at low optical power and for higher pulse repetition rates of ~ 1 Gbit/s and beyond, and would also allow the use of shorter waveguide to reduce the RC time and increase the speed.

Pulse width dependent measurements were also performed to assess the suitability of the TPA GaAs waveguide detector for ultra-fast threshold operation. The idea is that according to equation 4.28, two pulses with equal energies but very different pulse widths (hence different peak intensities) should give correspondingly different photocurrents. A strong contrast in photocurrent as a function of peak intensity would approximate the desired ultra-fast thresholding function. Fig. 4.15 shows data obtained by using the pulse stretcher set-up to broaden the pulses over the range from ~ 180 fs to ~ 4 ps.

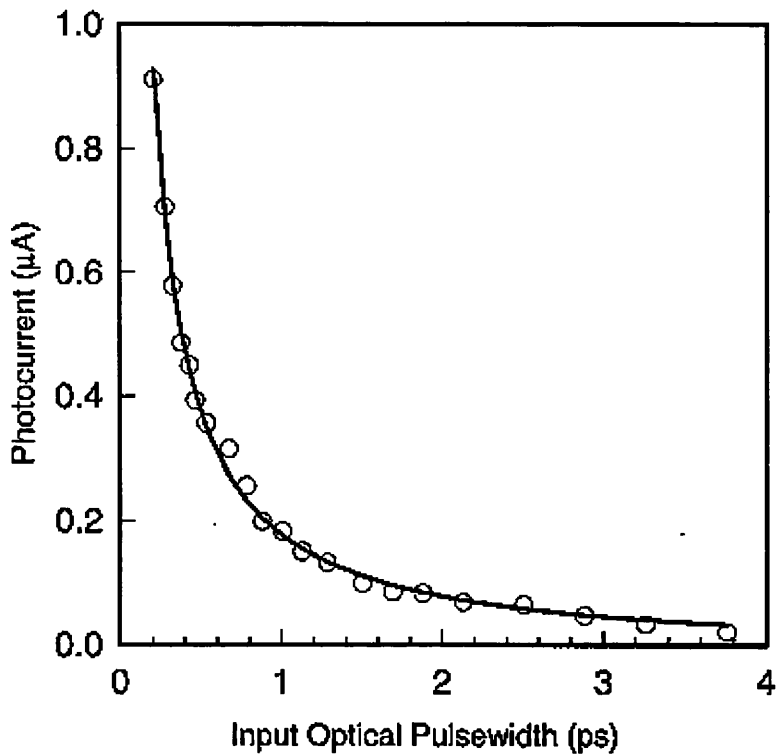


*Fig. 4.15: Pulse width dependence of TPA photocurrent.
 o: experimental data measured for different pulse widths.
 —: $a\tau^{-1}$ curve fitted to the data.*

The average optical power was held constant at 1.4 mW. The average photocurrent decreases by about twenty times as the pulse width increases from ~180 fs to ~4 ps. The data are well fitted by a τ^{-1} curve, in good agreement with theoretical predictions. There are some small deviations from the fitted curve, which may be caused by changes in the pulse shape itself (not just the pulse width) as the slit width is varied. It is believed this is the first experimental verification of the pulse width dependence of TPA on femtosecond time scale.

To show the feasibility of utilising these devices as non-linear detectors for communication applications, the electrical response of the waveguide photodetectors was observed in the time domain by using a sampling oscilloscope. The trace obtained using the 80 MHz mode-locked pulse train is shown in Fig. 4.16.

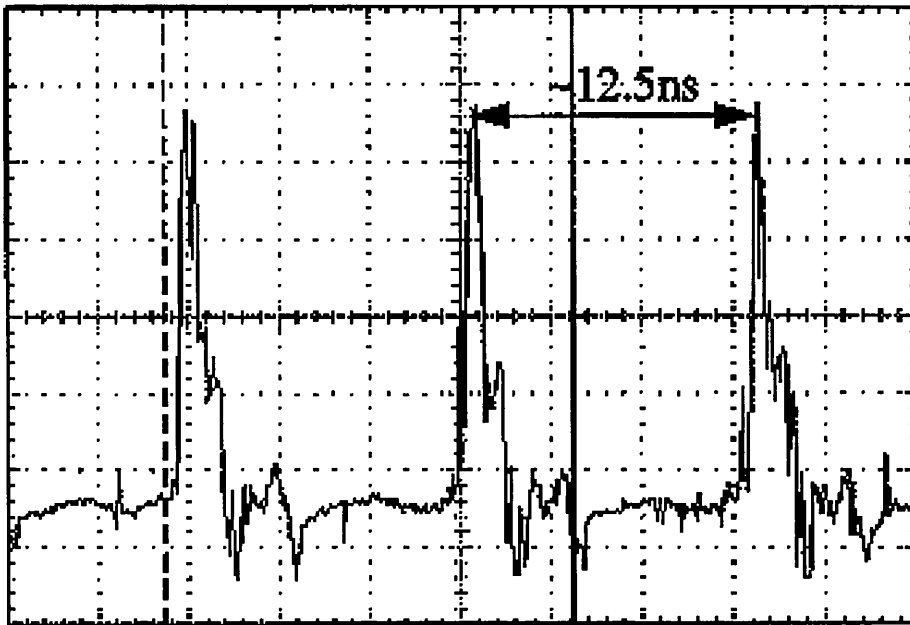


Fig. 4.16: Measured electrical impulse of the waveguide on sampling oscilloscope.

The FWHM width of the current pulse was ~ 400 ps. The extra bumps in the data are reflections due to impedance mismatches in the external circuit. The peak voltage response on the $50\ \Omega$ oscilloscope was > 50 mV at 10 mW average optical input. The non-linear photocurrent observed in the current experiments already shows a sufficiently fast response for applications up to ~ 1 Gbit/s. The response time is almost likely limited either by the RC time of the waveguide photodetector itself or by parasitic associated with rather crude external contacting scheme. It should be possible to obtain faster electrical response by reducing the waveguide length and improving the electrical packaging.

4.9 Conclusions

Methods of detection and measurement of ultra-short pulses have been introduced. A brief theoretical treatment of the structure of an ultra-short pulse has been given which leads to the concept of a bandwidth-limited pulse. The relationship between spectral bandwidth and temporal pulse width was derived, indicating the limits attainable in the production of ultra-short pulses. Correlation techniques used in

high repetition rate pulsed laser systems have been introduced. Linear and non-linear autocorrelation techniques were described in detail. The necessary conditions for obtaining an interferometric correlation have been noted. The relation between interferometric autocorrelations and pulse structure was discussed.

We have characterised the non-linear intensity dependence of the photocurrent for both a CW and mode-locked laser beam in an AlGaAs waveguide detector and then used this device to observe part of the interferometric autocorrelation trace from a mode-locked Nd³⁺:YAG. The device was then used to carry out both intensity and interferometric autocorrelation measurements of mode-locked Nd³⁺:YLF laser pulses.

The anisotropic behaviour of the two photon absorption coefficient was observed from photocurrent measurements at different crystalline orientations for an AlGaAs waveguide autocorrelator at a wavelength of 1.047 μm . It was also shown that, while using TPA for pulse measurement, the contrast ratio of the waveguide autocorrelator is increased.

Finally, the TPA induced photocurrent in a bulk GaAs waveguide photodetector in response to femtosecond pulses at 1.5 μm was characterised. It was shown that the photocurrent varies inversely with optical pulse width. The device also demonstrated a sub-nanosecond electrical response time. These experiments demonstrate the possibility of applying such devices as non-linear detectors to retrieve peak intensity and pulse width related information at communications wavelengths at high speed.

4.10 References

- [1] H. P. Weber, "Method for pulse width measurement of ultra-short light pulses generated by phase-locked lasers using non-linear optics", *J. Appl. Phys.*, pp. 2231-2234, 1967.
- [2] J. A. Armstrong, "Measurement of picosecond laser pulse widths", *Appl. Phys. Lett.*, pp. 16-18, 1967.
- [3] D. Gloge and R. Roldan, "Investigation of low power laser signals with picosecond resolution", *Appl. Phys. Lett.*, pp. 3-4, 1969.
- [4] J. A. Giodmaine, P. M. Rentzepis, S. L. Shapiro and K. W. Wecht, "Two photon excitation of fluorescence by picosecond light pulses", *Appl. Phys. Lett.*, pp. 216-218, 1967.
- [5] Y. Takagi, T. Kobayashi, K. Yoshihira and S. Imamura, "Multiple and single shot autocorrelator based on two photon conductivity in semiconductor", *Optics. Lett.*, Vol. 17, pp. 658-660, 1992.
- [6] F. R. Laughton, J. H. Marsh, D. A. Barrow and E. L. Portnoi, "The two-photon absorption semiconductor waveguide autocorrelator", *IEEE J. Quantum Electron.*, Vol. 30, pp. 838-845, 1994.
- [7] T. Kurobori, Y. Cho, and Y. Matsuo, "Intensity/phase autocorrelator for the use of ultra-short optical pulse measurements", *Optics Communications*, Vol. 40, pp. 156-160, 1981.
- [8] J. C. M. Diels, J. J. Fontaine, I. C. McMichael, and F. Simoni, "Control and measurement of ultra-short pulse shapes (in amplitude and phase) with femtosecond accuracy", *Appl. Optics*, Vol. 24, pp. 1270-1282, May 1985.
- [9] K. Naganuma, K. Mogi, and H. Yamada, "General method for ultra-short light pulse chirp measurement", *IEEE J. Quantum Electron.*, Vol. 25, pp. 1225-1233, 1989.
- [10] D. J. Bradley and G. H. C. New, "Ultra-short pulse measurements", *Proc. IEEE*, Vol. 62, pp. 313-345, March 1974.
- [11] M. Born and e, Wolf, "Principle of Optics", 3rd ed., New York, Pergamon, 1965.

- [12] L. Mandel and E. Wolf, "Coherence properties of optical fields", *Rev. Phys.*, Vol. 37, pp. 231-287, Apr. 1965.
- [13] A. J. De Maria, "Picosecond laser pulses", *Proc. IEEE*, Vol. 57, pp. 2-25, Jan. 1969.
- [14] K. L. Sala, G. A. Kenney-Wallace, and G. E. Hall, "CW autocorrelation measurements of picosecond laser pulses", *IEEE J. Quantum Electron.*, Vol. 16, pp. 990-996, Sep. 1980.
- [15] T. Mindl, P. Hefferle, S. Schneider, and F. Dörr, "Characterisation of a train of subpicosecond laser pulses by fringe resolved autocorrelation measurements", *Appl. Phys. B*, Vol. 31, pp. 201-207, 1983.
- [16] G. T. Maker and A. I. Ferguson, "Frequency-modulation mode locking of a diode-pumped Nd:YAG laser", *Optics Lett.*, Vol. 14, pp. 788-790, 1989.
- [17] G. P. A. Malcolm and A. I. Ferguson, "Self-mode locking of a diode-pumped Nd:YLF laser", *Optics Lett.*, Vol. 16, pp. 1967-1969, 1991.
- [18] Mohammad M. Karkhanehchi, David A. Barrow, A. Catrina Bryce, Craig J. Hamilton, and John H. Marsh, "Influence of single photon absorption on the performance of the two photon waveguide autocorrelator", *IEEE J. Quantum Electron.*, Vol. 33, No. 6, June 1997.
- [19] G. P. Agrawal, "Nonlinear Fiber Optics", Academic Press, Boston, 1989.
- [20] D. R. Heatley and W. J. Firth and C. N. Ironside, "Ultrashort-pulse generation using two-photon gain", *Optics Lett.*, Vol. 18, pp. 628-630, 1993.
- [21] V. Mizrahi, K. W. DeLong, G. I. Stegeman, M. A. Saifi, and M. J. Andrejco, "Two-photon absorption as a limitation to all-optical switching", *Optics Lett.* Vol. 14, pp. 1140-1142, 1989.
- [22] K. W. DeLong, K. B. Rochford, and G. I. Stegeman, "Effect of two-photon absorption on all-optical guided-wave devices", *Appl. Phys. Lett.*, Vol. 55, pp. 1823-1825, 1989.
- [23] J. S. Aitchison, M. K. Oliver, E. Kapon, E. Colas, and P. W. E. Smith, "Role of two-photon absorption in ultrafast semiconductor optical switching devices", *Appl. Phys. Lett.*, Vol. 56, pp. 1305-1307, 1990.

- [24] E. W. Van Stryland, H. Vanherzeele, M. A. Woodall, M. J. Soileau, A. L. Smirl, S. Guha, and T. F. Boggess, "Two-photon absorption, nonlinear refraction, and optical limiting in semiconductors", *Opt. Eng.*, Vol. 24, pp. 613-623, 1985.
- [25] D. C. Hutchings and B. S. Van Stryland, "Nondegenerate two-photon absorption in zinc-blende semiconductors", *J. Opt. Soc. Am. B* 9, pp. 2065-2074, 1992.
- [26] D. C. Hutchings and B. S. Wherret, "Theory of anisotropy of two photon absorption in zinc-blende semiconductor", *Phys. Rev. B* 49, pp. 2418-2426, 1994.
- [27] M. D. Dvorak, W. A. Schroeder, D. R. Andersen, A. L. Smirl and B. S. Wherret, "Measurement of the anisotropy of two-photon absorption coefficients in zinc-blende semiconductors", *IEEE J. Quantum Electron.*, Vol. 30, pp. 256-268, 1994.
- [28] R. DeSalvo, M. Sheik-Bahae, A. A. Said, D. J. Hagan and E. w. Van Stryland, "Z-scan measurements of the anisotropy of nonlinear refraction and absorption in crystals", *Optics Lett.*, Vol. 18, pp. 194-196, 1993.
- [29] S. J. Bepko, "Anisotropy of two-photon absorption in GaAs and CdTe", *Phys. Rev. B* 12, pp. 669-672, 1975.
- [30] J. P. Van Der Ziel, "Two-photon absorption spectra of GaAs with $2\hbar\omega_1$ near the direct band gap", *Phys. Rev. B* 16, pp. 2775-2780, 1977.
- [31] G. I. Stegeman, E. M. Wright, N. Finlayson, R. Zanoni and C. T. Seaton, "Third order nonlinear integrated optics", *J. Light Tech.*, Vol. 6, pp. 953-970, 1988.
- [32] J. A. Salehi, A. M. Weiner and J. P. Heritage, "Coherent ultrashort light pulse code division multiple access communication systems", *J. of Lightwave Tech.*, Vol. 8, pp. 478-491, 1989.
- [33] A. M. Weiner, J. P. Heritage and E. M. Kirschner, "High-resolution femtosecond pulse shaping", *J. Opt. Soc. Am. B* 5, No. 8, pp. 1563-1572, 1988.
- [34] J. S. Aitchison, Y. Silberberg, A. M. Weiner, D. E. Leaird, M. K. Oliver, J. L. Jackel, E. M. Vogel and P. W. E. Smith, "Spatial optical solitons in planar glass waveguides", *J. Opt. Soc. Am. B* 8, No. 6, pp. 1290-1297, 1991.
- [35] M. M. Karkhanehchi, C. J. Hamilton, and J. H. Marsh, "Autocorrelation measurements of mode-locked Nd:YLF laser pulses using two photon absorption

waveguide autocorrelator", IEEE Photonics Tech. Lett., Vol. 9, No. 5, pp. 645-647, May 1997.

[36] A. Villeneuve, C. C. Yang, G. I. Stegeman, C. N. Ironside, G. S. Celsi, and R. M. Osgood, "Nonlinear absorption in a GaAs waveguide just above half the bandgap", IEEE J. Quantum Electron., Vol. 30, pp. 1172-1175, 1994.

[37] A. Villeneuve, C. C. Yang, G. I. Stegeman, C. H. Lin, and H. H. Lin, "Nonlinear refractive-index and two photon absorption near half the bandgap in AlGaAs", Appl. Phys. Lett., Vol. 62, pp. 2465-2467, 1993.

[38] H. K. Tsang, L. Y. Chan, J. B. D. Soole, H. P. LeBlanc, M. A. Koza, and R. Bhat, "High sensitivity autocorrelation using two-photon absorption in InGaAsP waveguides", Electron. Lett., Vol. 31, pp. 1773-1775, 1995.

Chapter 5

The Influence of Single Photon Absorption on the Performance of the Two Photon Waveguide Autocorrelator

This Chapter presents the results of loss measurements performed on the two photon waveguide autocorrelator. The first part of this Chapter is concerned with the Fabry-Perot loss measurement technique, followed by simulation of propagation of light in the cladding layers, the GaAs cap layer, and the substrate of the waveguide. The single photon absorption (SPA) of the autocorrelator waveguide was then measured and it is shown that the effect of SPA on the autocorrelator performance is to reduce the contrast ratio in the manner observed experimentally.

5.1 Introduction

In order to measure the duration of ultra-short laser pulses, various autocorrelation techniques have been addressed in Chapter 4. It was demonstrated that a waveguide photodiode, because of its increased length, is more sensitive than a simple photodiode structure and offers much greater opportunity for integration [1].

Two photon absorption (TPA) is a non-resonant non-linear process that occurs for photons with energy ($h\nu$) less than the semiconductor energy gap E_g , but greater than $E_g/2$. When using TPA for intensity autocorrelation measurements, very little single photon absorption occurs for photons with $h\nu$ less than E_g , but greater than $E_g/2$. It was previously shown that such waveguide autocorrelator detectors, although they work well and have good sensitivities, have constant ratios which are less than the expected ratio of 2:1, and that the contrast ratio becomes worse as the peak power of the pulse is reduced [2]. It is shown in this Chapter that single photon absorption has the effect of reducing the contrast ratio of the two photon waveguide autocorrelator.

Integrated optoelectronic devices made of semiconductors, particularly III-V semiconductor compounds, have considerable interest. Such components may form the basis for integrated optoelectronic circuits in which light sources and detectors, as well as optical waveguide devices and electronic circuitry, are monolithically integrated on the same substrate. In non-linear optics waveguides must possess low losses, so as to ensure that the intensity stays at a level that will ensure the desired effects can be observed. In general, there are three important mechanisms responsible for losses in rib waveguides: scattering, leakage and absorption.

Leakage loss occurs when the waveguide is supported on a substrate, and/or capped with a material which has a refractive index equal to or greater than the waveguide index, so guided light can leak into the substrate or the cap and is lost from the waveguide [3]. In the structure used in this work the substrate and capping layers have the highest refractive index. Therefore, in order to ensure a small optical leakage loss, thick upper and lower AlGaAs cladding layers (1 μm and 4 μm respectively) were included in the design (Fig. 3.7 in Chapter 3).

Absorption losses arise from band edge absorption, absorption by defect states in the bandgap and absorption by the free carriers [4]. The first two of these will contribute to the single photon absorption photocurrent but, by working well away from the band edge and using high quality material, these losses will be small. In order to reduce losses due to free carrier absorption, those parts of the cladding regions which were expected to have significant overlap with the optical mode were left undoped.

Scattering losses in rib waveguides may arise from interface roughness [5] and side wall roughness [6]. For an epitaxially grown III-V structure, the interface roughness can be reduced to an insignificant level. However, side wall roughness, due to both dry and wet etching processes, is still important [7]. It has been suggested that the scattering loss due to sidewall roughness in a single mode waveguide increases with the square of the roughness amplitude [8]. We therefore

believed that the most important loss mechanism in the waveguide autocorrelator is due to scattering by imperfections in the ridge structure, which can be caused by various processes, e.g., imperfect photolithography and etching steps.

Propagation loss measurement of optical waveguides is required before design and fabrication of all guided-wave devices. There are many ways to determine the optical losses of waveguides experimentally; these include the sequential cleaving method [9], and the optimum end-fire coupling (OEC) technique [10]. The most common way of determining the linear losses of semiconductor waveguides is the Fabry-Perot method which was developed by Walker [11].

Two methods were used for the waveguide loss measurements in this thesis. First the Fabry-Perot technique which is based on measurement of the finesse of the Fabry-Perot resonance of the semiconductor waveguide using a narrow linewidth Ti:Sapphire laser. Secondly, transmission measurements were made using a Ti:Sapphire laser over a larger wavelength range and without the linewidth narrowing étalon.

5.2 Waveguides Fabrication

Nominally identical p-i-n waveguide structures were grown by metal-organic vapour phase epitaxy (MOVPE) and molecular beam epitaxy (MBE). The structure consisted of an AlGaAs waveguide core surrounded by AlGaAs cladding regions, as shown in Fig. 3.7 in Chapter 3. Again, ridge waveguides 3 μm wide, 5 mm long, and separated by 100 μm were fabricated by dry etching. Wet etching was subsequently used to mesa between the ribs to isolate individual devices [2].

5.3 Theory of Fabry-Perot Technique

The system used to establish the transmission of an optical waveguide is shown in Fig. 5.1. The waveguide consists of a medium with a facet at either end [12]. The facets act as reflectors due to the abrupt change of refractive index from the guiding

medium within the cavity to air outside the cavity. Starting on the left hand side of the diagram, a normally incident optical wave with amplitude E_i arrives at the facet. The amount of light entering the structure is equal to $t_1 E_i$ where t_1 is the electric field transmission coefficient of facet 1. By the time the wave has reach facet 2 it has been attenuated by a factor $e^{-\alpha l}$ and has undergone a phase shift of e^{-ikl} . The light is then split into two components: a fraction t_2 is transmitted through the facet and a fraction r_2 is reflected back into the cavity.

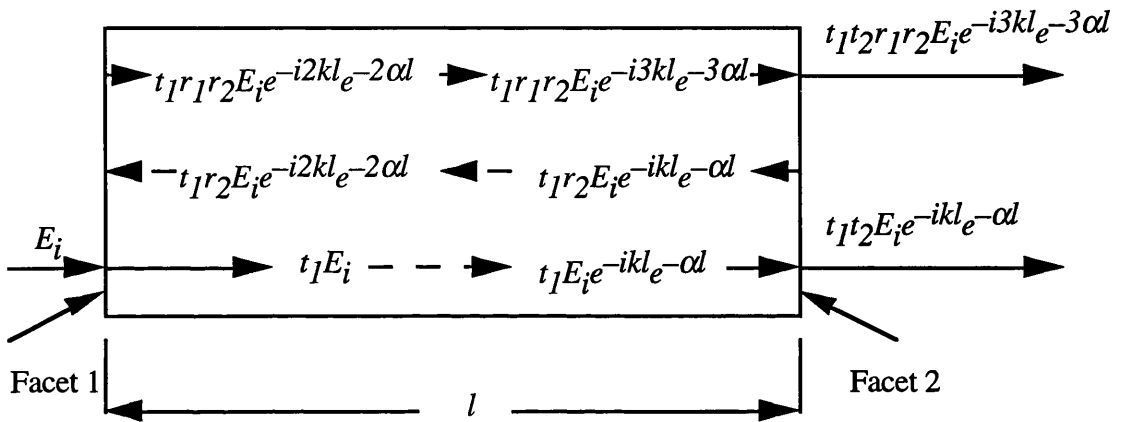


Fig. 5.1: Schematic of an optical waveguide used to drive the transmission coefficient of the Fabry-Perot structure.

The reflected light travels down the cavity once more until it reaches facet 1 when it is partially reflected back towards facet 2. This process carries on indefinitely. What is important to mention here is that optical intensity cannot be lost at the facets; it is either reflected or transmitted, as there are assumed to be no scattering losses. The relation $T = 1 - R$ can therefore be used to simplify the following expressions, where $T^2 = t^2$, and $R^2 = r^2$. R and T are, respectively, the fractions of the intensity reflected and transmitted at each facet.

By following the ray, as indicated in Fig. 5.1, it is easy to show that the transmitted wave will have an amplitude given by the following summation:

$$E_t = E_i t_1 t_2 e^{-ikl} e^{-\alpha l} \left[1 + r_1 r_2 e^{-2ikl} e^{-2\alpha l} + r_1^2 r_2^2 e^{-4ikl} e^{-4\alpha l} + \dots \right] \quad (5.1)$$

If we simplify equation 6.1 by substituting $T = t_1 t_2$ and $R = r_1 r_2$ and note that the term in the bracket is a geometric progression with a sum:

$$\frac{E_t}{E_i} = \left[\frac{T e^{-ikl} e^{-\alpha l}}{1 - R e^{-2ikl} e^{-2\alpha l}} \right] \quad (5.2)$$

Then the ratio of the incident to transmitted intensities is given by:

$$\left| \frac{E_t}{E_i} \right|^2 = \frac{T^2 e^{-2\alpha l}}{1 - 2R e^{-2\alpha l} \cos(2kl) + R^2 e^{-4\alpha l}} \quad (5.3)$$

Substituting $\gamma = e^{-\alpha l}$ and $T = 1 - R$, we obtain:

$$\left| \frac{E_t}{E_i} \right|^2 = \frac{(1 - R)^2 \gamma^2}{1 - 2R\gamma^2 \cos(2kl) + R^2 \gamma^4} \quad (5.4)$$

where γ now represents the fractional single pass loss of the waveguide.

Maximum transmission will occur when the denominator of equation 5.4 is at its smallest value. If we vary k only, then this will occur when $\cos(2kl) = 1$, i.e. when $kl = m\pi/2$, and m is an integer. In this case the Fabry-Perot transmission is said to be in the resonant state and is given by:

$$T_R = \left[\frac{(1 - R)\gamma}{1 - R\gamma^2} \right]^2 \quad (5.5)$$

On the other hand when $\cos(2kl) = -1$, i.e. when $kl = m\pi$, and again m is an integer, the resonant is said to be the anti-resonant state. The transmission is at its lowest value and is given by:

$$T_A = \left[\frac{(1 - R)\gamma}{1 + R\gamma^2} \right]^2 \quad (5.6)$$

By comparing these two expression it is now possible to obtain the loss of the waveguide, i.e. γ in terms of the transmission coefficients. Simplifying the expressions by defining K as:

$$K = \frac{T_R}{T_A} \quad (5.7)$$

the propagation loss, α , in the waveguide can be written as:

$$\alpha(\text{dB cm}^{-1}) = - \left(\frac{10}{L} \right) \log_{10} \left[\frac{(\sqrt{K} - 1)}{R(\sqrt{K} + 1)} \right] \quad (5.8)$$

where L is the device cavity length in *cm*.

Finally to solve equation 5.8 we need to know all of the parameters on the right hand side of the equation. We are to measure K from the Fabry-Perot resonances but we must also calculate the reflectance R . The reflectivity can be expressed at a dielectric interface as [13]:

$$R = \left(\frac{n_{\text{dielec}} - 1}{n_{\text{dielec}} + 1} \right)^2 \quad (5.9)$$

where n_{dielec} is the refractive index of the dielectric waveguide and 1 is the refractive index of air.

The equations 5.8 and 5.9 are used to calculate the loss of an optical waveguide in the following experiments. Fabry-Perot fringes are observed by varying kl and probing the waveguide with a narrow linewidth source at the wavelength of interest. kl is varied by heating the waveguide; heating has the effect of increasing the refractive index of the waveguide which changes the optical length of the waveguide. In order that the fringes are visible, the linewidth of the laser used to probe the waveguide must be much less than the free spectral range of the étalon. The free spectral range, which is defined as the separation between the frequencies of the étalon which lead to maximum transmission, can be shown to be [12]:

$$\Delta\nu = \frac{c}{2nL} \quad (5.10)$$

where c is the velocity of light, L is the length of the waveguide and n is the refractive index of the waveguide. The waveguides to be measured were 5 mm long and $n \approx 3.6$, so that the free spectral range was about 10^{10} Hz. This is the absolute maximum linewidth of a laser that can be used to observe the Fabry-Perot fringes, though obviously the narrower the linewidth of the source the greater the clarity of the fringes will be. A Ti:Sapphire laser, with an étalon installed in its cavity, was used in the experiments. The laser linewidth was around 60 MHz.

5.4 Experimental Set-up

The apparatus used to measure loss by the Fabry-Perot technique is shown in Fig. 5.2. Briefly, an argon-ion laser was used to pump the Ti:Sapphire laser which was tuneable over the wavelength range 700-1000 nm using an adjustable birefringent filter in conjunction with an interchangeable set of mirrors. To ensure narrow linewidth operation, an étalon was installed in the Ti:Sapphire laser cavity. The sample, which was 5 mm long, was mounted on a thin metal stand which was made to hold the waveguide above the translation stage with differential drives so that the objective lenses could be brought close up to the facets.

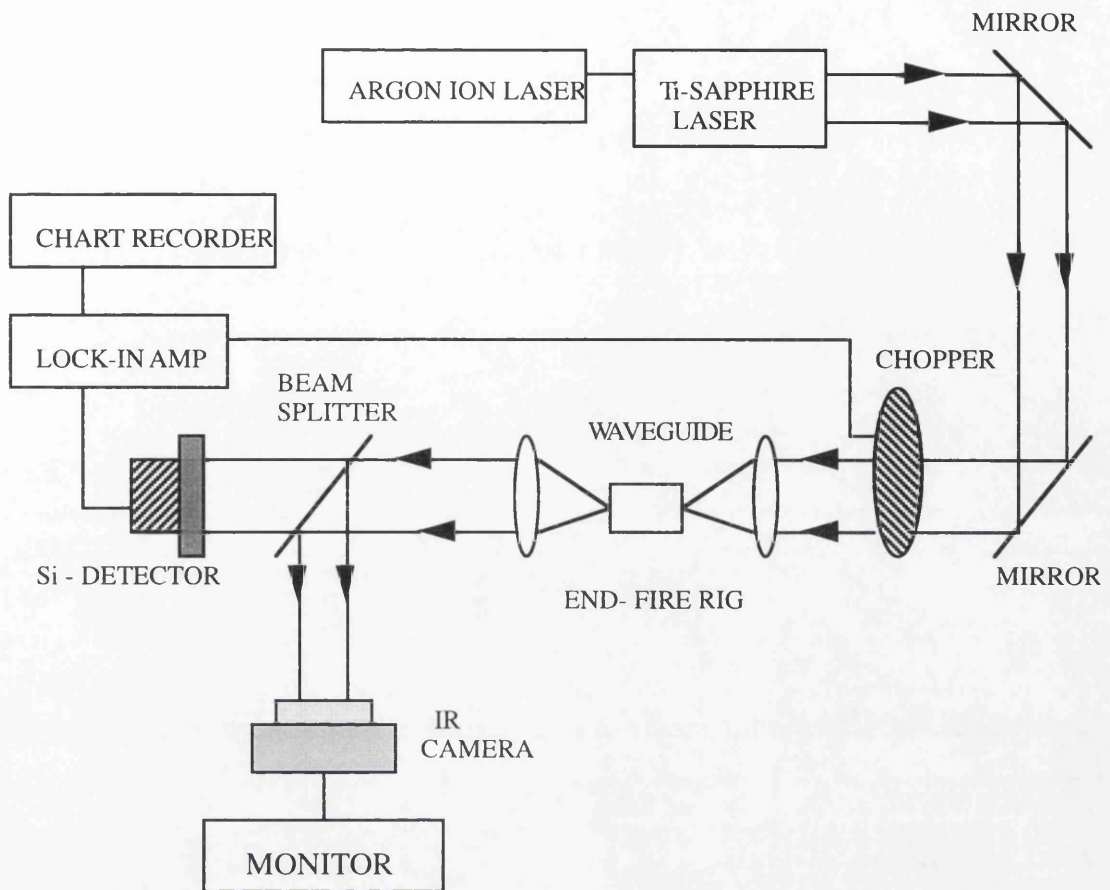


Fig. 5.2: Experimental set-up for the Fabry-Perot loss measurements.

The laser light was launched into the waveguides by means of end-fire coupling. The coupling efficiency is extremely sensitive to the position of the lenses, and so the lenses were mounted on translation stages with differential drives. Both the input and output lenses could be independently adjusted to optimise focusing and alignment, and the sample could also be translated and rotated independently of the lenses. When aligning a waveguide, the camera and monitor were used to assist in the alignment of the output facet and to confirm maximum guiding in the waveguides. A reference signal from the chopper and the output signal from the Si-detector were input to the lock-in amplifier. The photocurrent through the detector was measured by a phase sensitive lock-in amplifier, and the results were then plotted on a chart recorder.

The Fabry-Perot technique requires a heat source to warm the waveguide from above. The heating source used here was a soldering iron. This will change both the

length and the refractive index of the waveguide. The value of " K " can therefore be determined from an average of five or six of resonance/antiresonances cycles which are recorded on the chart recorder during the heating of the waveguide.

An example of such Fabry-Perot fringes obtained from a 5 mm long single mode waveguide, is given in Fig. 5.3.

It is noted that single mode guiding is important in this measurement since multi-mode guiding will produce resonance fringes which will not be in phase with each other, so resulting in measurement error [7].

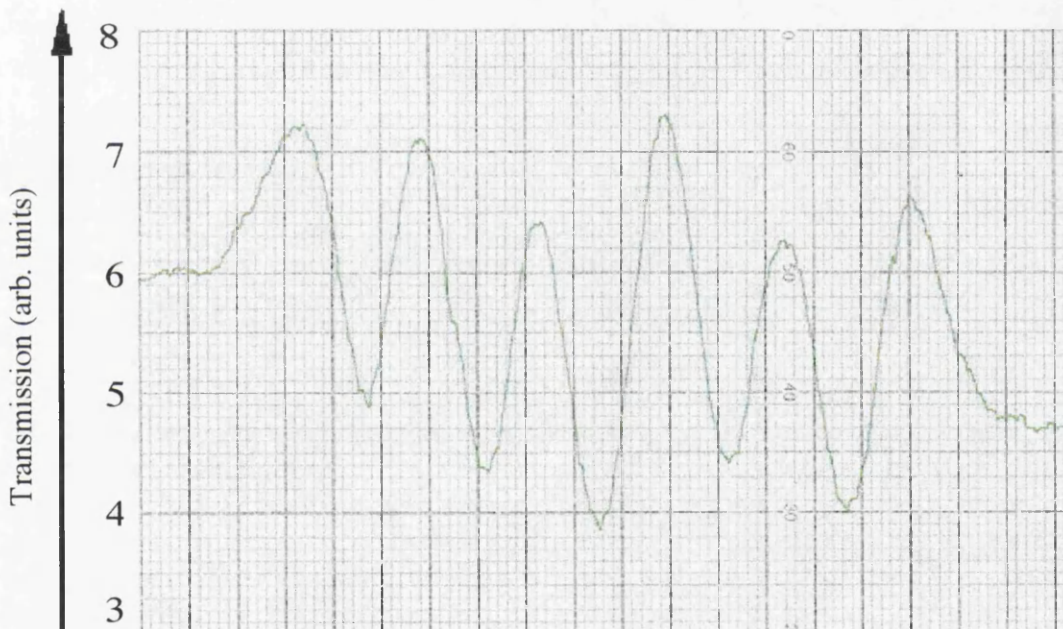


Fig. 5.3: Fabry-Perot resonances taken from a single mode 5 mm long waveguide at wavelength of 904 nm.

Optical propagation losses, as a function of wavelength were measured in the range of 760-930 nm. The results give the total propagation loss, α_{total} , and are shown in Fig. 5.4 for the MOCVD sample and for the MBE grown sample. The losses in the MBE grown material are slightly higher than in the MOCVD material.

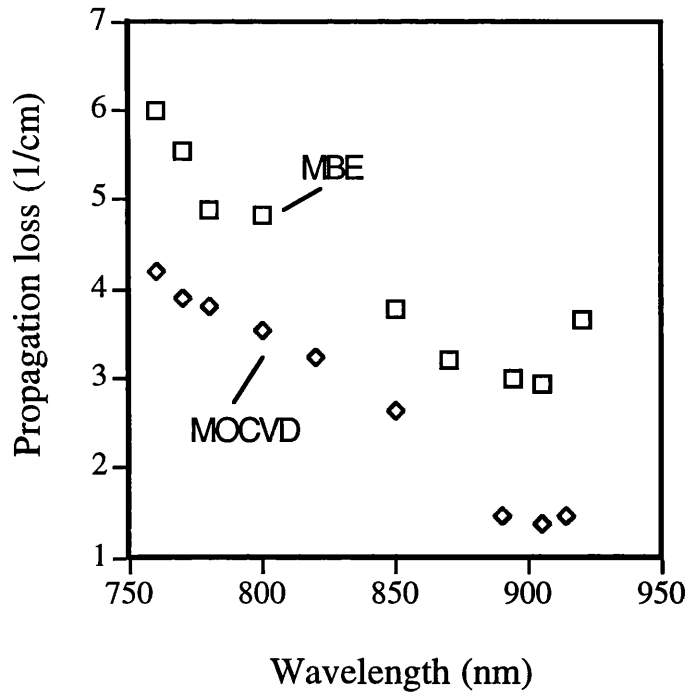


Fig. 5.4: The propagation loss as a function of wavelength for the MOCVD and the MBE grown sample.

In general, the plot of the waveguide losses as a function of wavelength can be divided into two regions in Fig. 5.4. The first region showed an increase in loss towards short wavelength, and the second region gave a gradually increasing loss towards the longer wavelength region. The fast increase in loss in region I, the short wavelength region, is dominated by band edge absorption since the guides at these wavelengths are near to Urbach tail of the band edge. The gradual increase in loss in region II, the long wavelength region, may be due to the combined effects of the free carrier absorption from the p and n-doped cladding layers and the radiation leakage loss due to the high refractive index, heavily p-doped, GaAs cap layer and the existence of shallow impurity bands in the forbidden gap.

The combined effects of the free carrier absorption from the p-and n-doped cladding layers, and of the radiation leakage loss into the GaAs cap layer were assessed, in the next section, using a program for solving electromagnetic wave propagation in a waveguide using the finite difference method (F-Wave IV) [14].

Secondly, transmission measurements were made using a Ti:Sapphire laser over a larger wavelength range and without the linewidth narrowing étalon. The optical power in front of the input objective P_{in} , and the output power from the waveguide P_{out} were both measured. The total waveguide loss can be derived from the transmission using the expression:

$$P_{out} = P_{in} C (1 - R)^2 \exp(-\alpha_{total} L) \quad (5.11)$$

where C is the coupling efficiency of light from before the objective into the guided mode excluding the effect of the input facet reflectivity, R is the facet reflectivity (taken to be 0.3), and L is the waveguide length. In this experiment, the waveguide length was, again, 5 mm. Using the value of α_{total} calculated from the Fabry-Perot measurements, the input coupling efficiency (C) could be found from equation 5.11. The value $C = 0.128$ was obtained. The results are shown in Figs. 5.7 and 5.8, from which it can be seen that there is close agreement between the two techniques over the complete wavelength range of the Fabry-Perot measurements.

5.5 Simulation of Waveguide Losses using F-Wave IV

F-Wave IV is used here to simulate the 2D optical field distribution in a 3 μm wide, 0.8 μm high rib waveguide with the structure shown in Fig. 3.7 (Section 3.6 in Chapter 3). The propagation of light in the cladding layers was calculated as a function of wavelength.

Simulations were carried out to study the field distribution in the as-grown sample in the wavelength range 760 to 1000 nm. This program does not accept a GaAs cap layer since it has a higher refractive index than the waveguide core. A 1.02 μm thick upper cladding layer was therefore used in the simulation instead of 1 μm . The electrical field interaction with the GaAs cap layer was then taken to be the same as with the top 0.02 μm region of this layer. The values of the refractive indices of AlGaAs at the particular wavelengths and aluminium fractions used in this simulation were taken from Fig. 3.4 (Section 3.4 in Chapter 3).

Data obtained from the simulation consists of the electrical field distribution in arbitrary units, which is directly proportional to the square root of the intensity, in both the x and y directions. Suppose that the field distributed in the x direction is E_x and in the y direction is E_y , the total field E_{total} distributed in the waveguide can be found from:

$$E_{total}^2 = E_x^2 + E_y^2 \quad (5.12)$$

The total intensity I_{total} of the guided light is directly proportional to the integrated square of the field which can be expressed as:

$$\int_{-\infty}^{+\infty} E_{total}^2 dx dy \propto I_{total} \quad (5.13)$$

Similarly, the intensity overlap with a particular layer can be written as:

$$\int_{layer(p)} E_{total(p)}^2 dx dy \propto I_{total(p)} \quad (5.14)$$

The optical overlap with the cladding layers and the leakage loss into the GaAs cap layer are calculated from the interaction of light in the particular layer expressed as a fraction of the total intensity. The loss due to free carrier absorption in the cladding regions will be :

$$\alpha_{UC} = C_{UC} \frac{I_{UC}}{I_{total}} \quad (5.15)$$

and

$$\alpha_{LC} = C_{LC} \frac{I_{LC}}{I_{total}} \quad (5.16)$$

where α_{UC} and α_{LC} are losses due to the absorption from the holes and electrons from the upper and lower cladding layers, C_{UC} and C_{LC} are the loss coefficients and I_{UC} and I_{LC} are the intensities overlapping with the upper and lower cladding layers,

respectively. The calculations show that the ratio $\frac{I_{UC}}{I_{total}}$ varies from 0.0076 to 0.0397, and $\frac{I_{LC}}{I_{total}}$ varies from 0.0102 to 0.0744 at wavelengths from 760 to 1000 nm.

It has been shown that free carrier absorption is linear [15]. An absorption coefficient of about 15 cm^{-1} for a hole concentration of about $5 \times 10^{17} \text{ cm}^{-3}$ and less than 10 cm^{-1} for an electron concentration of $5 \times 10^{17} \text{ cm}^{-3}$ were quoted. However, a relation for free carrier absorption as a function of hole and electron concentrations, which was found to fit various experiment data and is widely used, is given by [16]:

$$\alpha_{fc} \approx 7 \times 10^{-18} \times P + 3 \times 10^{-18} \times N \quad (5.17)$$

where P and N are the densities of holes and electrons respectively in cm^{-3} .

In this analysis, we therefore take C_{UC} as 3.5 cm^{-1} and C_{LC} as 1.5 cm^{-1} respectively for both p- and n-doping with concentrations of $5 \times 10^{17} \text{ cm}^{-3}$ using equation 5.17, and assume that C_{UC} and C_{LC} are constant throughout the range of wavelengths studied. Substituting these values into equations 5.15 and 5.16, and without taking band edge absorption into account, α_{UC} and α_{LC} will change from 0.027 to 0.14 cm^{-1} and 0.015 to 0.074 cm^{-1} at wavelengths between 760 to 1000 nm, respectively. As is shown in Fig. 5.5 the loss, due to free carrier absorption in cladding layers ($\alpha_{cladding} = \alpha_{UC} + \alpha_{LC}$), increases slowly with wavelength.

Similarly, the loss due to radiation leakage into the GaAs cap layer and substrate can be expressed:

$$\alpha_{cap/substrate} = C_{GaAs(cap/substrate)} \frac{I_{GaAs(cap/substrate)}}{I_{total}} \quad (5.18)$$

where $C_{GaAs(cap/substrate)}$ is the loss coefficient of the cap layer and substrate. This coefficient includes the absorption due to heavy hole doping ($5 \times 10^{18} \text{ cm}^{-3}$) and the radiation leakage resulting from the fact that the GaAs cap and substrate have a higher

refractive index than that of the core guiding layer. Again using F-Wave IV, the loss due to this mechanism is in the range $7.5 \times 10^{-10} \text{ cm}^{-1}$ to $1 \times 10^{-5} \text{ cm}^{-1}$ in the wavelength range 760 to 1000 nm. Therefore, although the leakage of light into the cap and substrate increases substantially with increasing wavelength, the loss is always negligible in the wavelength range being considered.

The total losses due to the combined effects of free carrier absorption in cladding layers and radiation leakage into the GaAs cap layer and substrate in the wavelength range 760 to 1000 nm are given in Fig. 5.5.

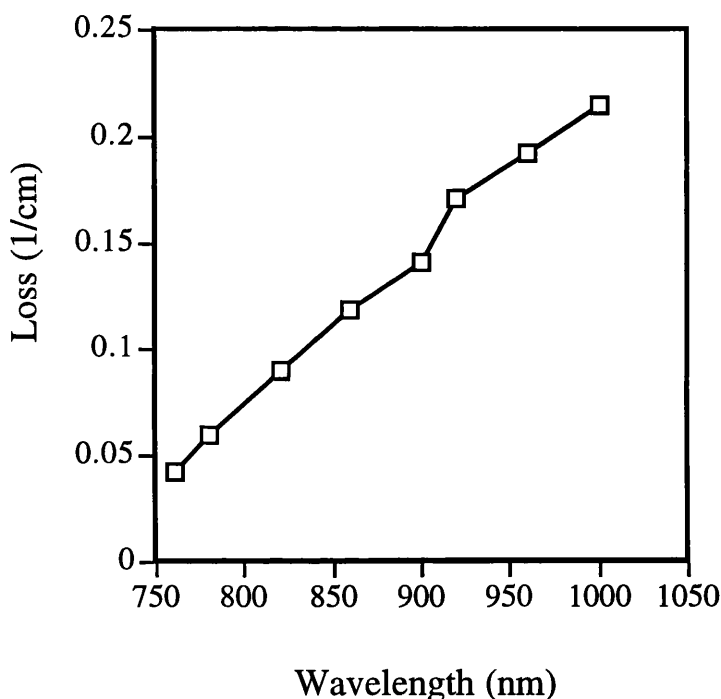


Fig. 5.5: The absorption from the free carrier absorption in cladding layers and from the GaAs cap layer and substrate as a function of wavelength as predicted by F-Wave IV.

So, the total propagation loss is essentially due to waveguide scattering and free carrier absorption. Single photon absorption beyond the band edge makes a negligible contribution to the propagation loss, but has a significant effect on the performance of the autocorrelator as is discussed in the next section.

5.6 Linear Absorption Photocurrent Measurements

In order to determine the magnitude of the single photon absorption, photocurrent measurements were made using the same experimental set-up as the transmission measurements. The laser beam was end-fire coupled into the waveguide, which was reversed-biased by 4.5 V. A 1 k Ω resistor was placed in series with the waveguide, and the photocurrent was found by measuring the voltage across the resistor using a lock-in amplifier.

The SPA coefficient, α_{SPA} , could now be found from the measurements of photocurrent using the equation:

$$\alpha_{SPA} = \frac{\alpha_{total} I_{ph} h\nu}{e\eta C(1-R)P_{in} [\exp(-\alpha_{total}L) - 1]} \quad (5.19)$$

where η is the quantum efficiency, e is the electron charge, h is Planck's constant, ν is the frequency and α_{total} is the propagation loss from the transmission measurements.

It was very important to ensure that SPA was being measured and that TPA effects were not present. Measurements were made to confirm that the photocurrent had a linear dependence on input power at several wavelengths. The results are shown in Fig. 5.6.

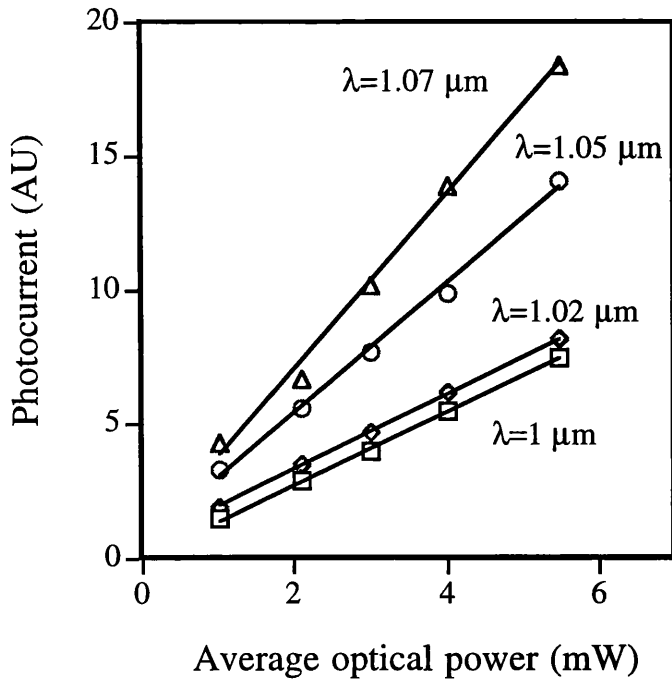


Fig. 5.6: Plot of the linear dependence of the photocurrent as a function of input optical power.

The variation of the SPA coefficient as a function of wavelength for MOCVD material is shown in Fig. 5.7.

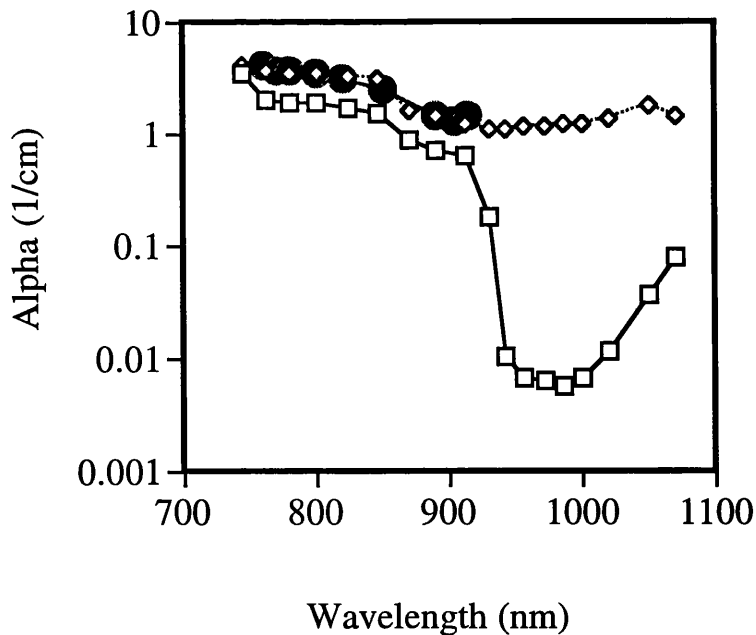


Fig. 5.7: Propagation losses as a function of wavelength for MOCVD material: ● measured by Fabry-Perot technique, ◇ from transmission measurements, □ single photon absorption from photocurrent measurement.

And similarly, the variation of the SPA coefficient as a function of wavelength for MBE material is shown in Fig. 5.8.

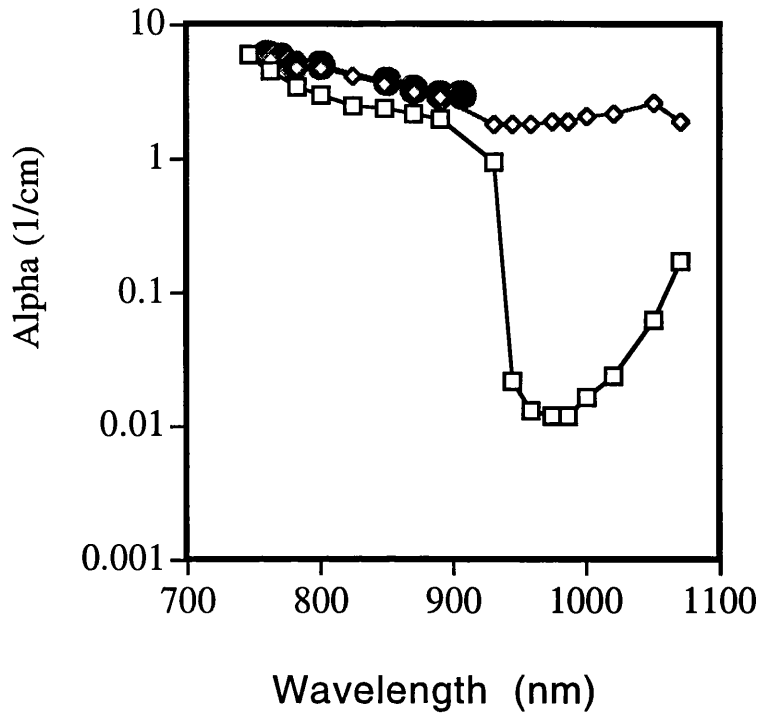


Fig. 5.8: Propagation losses as a function of wavelength for MBE material: ● measured by Fabry-Perot technique, ◊ from transmission measurements, □ single photon absorption from photocurrent measurement.

The behaviour can be divided into a number of regions. Initially there is a rapid decrease in SPA at short wavelengths, where the loss is dominated by band edge absorption due to the Urbach tail of the band edge. This loss was calculated for different wavelengths using the Urbach tail expression [17]:

$$\alpha = \alpha_0 \exp\left[-C(E_g - h\nu) / kT\right] \quad (5.20)$$

with the value of $\alpha_0 = 35 \text{ cm}^{-1}$. C is the empirical constant, k is Boltzmann's constant and T is temperature. Then, the measured α_{SPA} was compared with the Urbach tail expression for MOCVD material (Fig. 5.9). Initially the measured SPA follows the Urbach tail model but soon the Urbach tail absorption is insignificant compared to the measured absorption.

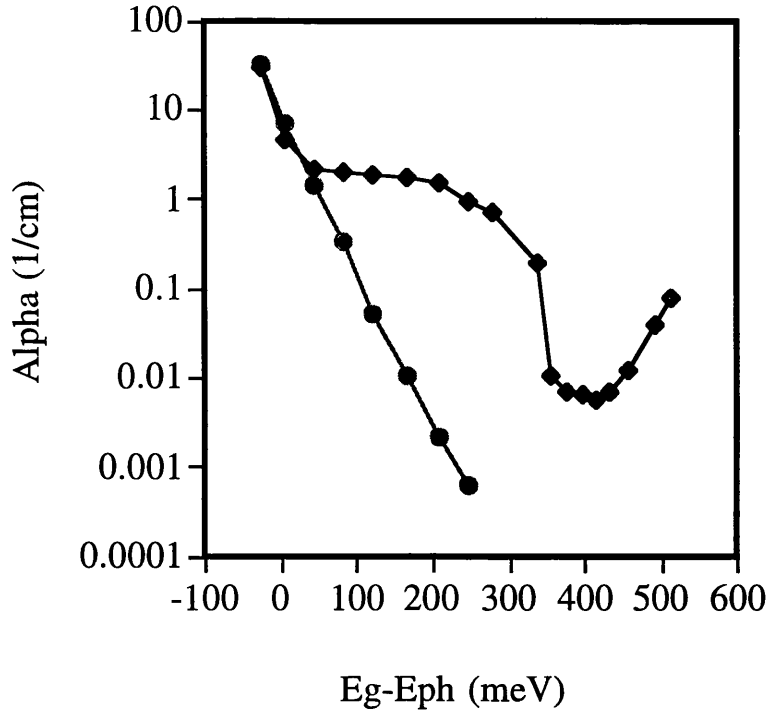


Fig. 5.9: Plot of comparison of the measured α_{SPA} (◆) with absorption predicted by Urbach tail model (●).

Beyond 800 nm, the experimental SPA coefficient becomes almost flat until dropping at 940 nm and then rising beyond 1000 nm. This behaviour is almost certainly due to deep levels caused by impurities present in the epitaxial material, the most probable impurity in $\text{Al}_x\text{Ga}_{1-x}\text{As}$ being oxygen [18-20], which is likely to form aluminium oxygen complexes such as AlO , Al_2O , and Al_2O_3 [19]. There are two particular traps with energy levels $E_T = 0.35$ eV and $E_T = 0.25$ eV which have been observed in AlGaAs [18]. The drop in the SPA at 940 nm corresponds to the energy of the deeper of these two traps in $\text{Al}_{0.2}\text{Ga}_{0.8}\text{As}$, the composition of the guiding layer, suggesting that it is these traps which are responsible for the SPA. It can also be seen that the α_{SPA} for the MBE material is higher than that in the MOCVD material suggesting that there is more oxygen incorporated in the latter.

5.7 Influence of Single Photon Absorption on the Contrast Ratio of the Waveguide Autocorrelator

To calculate the theoretical photocurrent as a function of the time delay, consider the two orthogonally polarised laser pulses being recombined in the waveguide after one is delayed with respect to the other. There are no interference effects because both beams are orthogonally polarised. The average autocorrelation photocurrent as a function of time delay between pulses is given by [2]:

$$I_{ph}(t_d) = e\Omega \left\{ \frac{2\alpha_{SPA}}{h\nu} I_{ave} + \frac{\beta t_p I_{ave}^2}{\sqrt{\pi} h\nu T} \left[1 + \exp\left(-\frac{t_d^2}{T^2}\right) \right] \right\} \quad (5.21)$$

where Ω is the volume in which the photogenerated carriers are created, I_{ave} is the average intensity of the beam, β is the two photon absorption coefficient, α_{SPA} is the single photon absorption coefficient, which is that fraction of the total waveguide propagation loss resulting from the generation of electron-hole pairs by single photons, t_p is the time between mode-locked pulses, t_d is the time delay between the two pulses in the waveguide and T is the duration of the laser pulses.

The contrast ratio is defined as the photocurrent ratio when the pulses are overlapped to that when they are non-overlapped. Therefore, using equation (5.21), the contrast ratio is :

$$\text{contrast ratio} = \frac{2 \left(1 + \frac{\beta}{\sqrt{2}\alpha_{SPA}} \frac{P_{peak}}{A} \right)}{2 + \frac{\beta}{\sqrt{2}\alpha_{SPA}} \frac{P_{peak}}{A}} \quad (5.22)$$

where, P_{peak} is the peak power in the guided mode, and A is the cross sectional area of the waveguide.

From the experimental data for autocorrelation measurements of mode-locked Nd:YLF laser pulses, β was found (Section 2.7, Chapter 4). β is not the same for all crystal orientations [21], but the effect of the crystal orientation dependence is to

increase not reduce the contrast ratio as it was discussed in section 4.7.2 in Chapter 4. The cross sectional area was calculated using F-Wave IV, and found to be $A = 4.2 \times 10^{-12} \text{ m}^2$. The contrast ratio was then calculated using data from the linear absorption measurement (α_{SPA}) and is shown in Fig. 5.10.

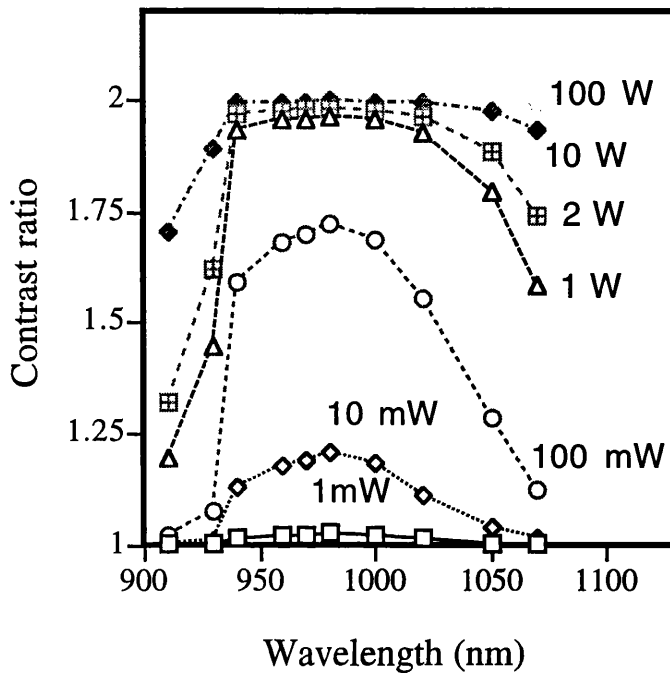


Fig. 5.10: Plot of the calculated contrast ratio as a function of wavelength.

It can be seen that, for low powers, the contrast ratio is well below 2:1. As the power is increased, the contrast ratio increases towards the value 2:1, more rapidly at wavelengths for which α_{SPA} is small. For wavelengths where α_{SPA} is larger, much higher powers are needed to achieve a contrast ratio of close to 2:1.

The waveguide autocorrelator used to measure the α_{SPA} was previously used to measure the contrast ratios achieved from a mode-locked Nd:YLF laser operating at $1.047 \mu\text{m}$ with different peak powers as discussed in Section 4.6.2, Chapter 4.

The measured contrast ratios along with earlier measurements of the contrast ratio from mode-locked Nd:YAG laser at $1.064 \mu\text{m}$ [1] are shown in Fig. 5.11. The results show that the ratio of the correlation peak photocurrent to the background are

1.92:1 ($P_{peak} = 13.5$ W), 1.88:1 ($P_{peak} = 4.5$ W), 1.73:1 ($P_{peak} = 1.1$ W), 1.63:1 ($P_{peak} = 0.7$ W) for the Nd:YLF laser and 1.7:1 for the Nd:YAG laser ($P_{peak} = 2.8$ W). It can be seen that these measurements are in close agreement with the contrast ratios which were calculated using the measured α_{SPA} .

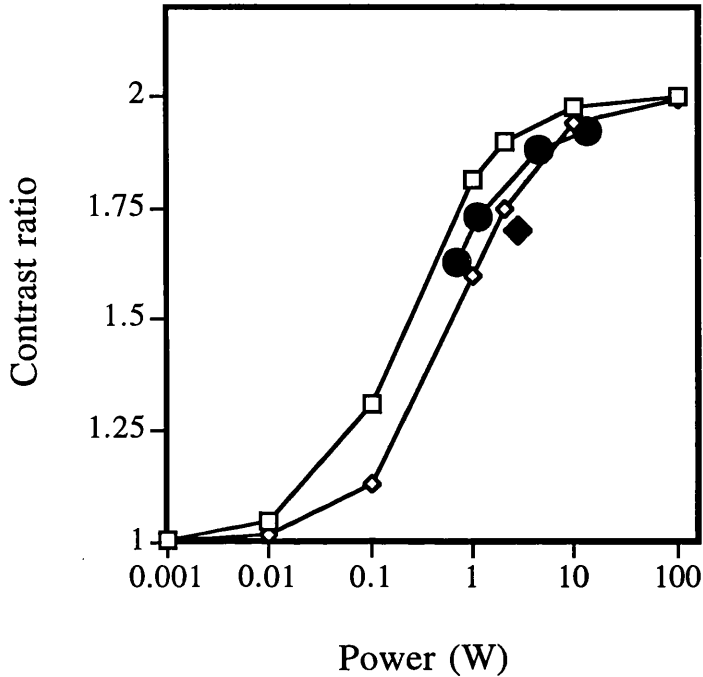


Fig. 5.11: Plot of the contrast ratio for different powers: calculated from model □ at 1047 nm and ◇ at 1064 nm; experimental ● at 1047 nm and ◆ at 1064 nm.

Also, a contrast ratio of ~ 1.5 was found for a Q-switched InGaAsP/InP laser at $1.3 \mu\text{m}$ by means of the p-i-n GaAs/AlGaAs waveguide [2]—at a peak power level in the waveguide of approximately 50 mW, corresponding to an insertion loss of approximately 20 dB.

5.8 Conclusions

To investigate the influence of linear absorption on autocorrelation performance, a photocurrent technique was used to measure linear photon absorption. It was shown that, because of the creation of a few carriers by single photon absorption while using TPA for pulse measurement, the contrast ratio resulting from

the overlap between two orthogonally polarised pulse trains in the waveguide is not 2:1, confirming theoretical predictions. In addition, the propagation loss of the waveguide was measured to be as low as 1.37 cm^{-1} at a wavelength of 904 nm. The achievement of such low propagation losses is essential for the realisation of high quality semiconductor guided-wave devices.

5.9 References

- [1] F. R. Laughton, J. H. Marsh and A. H. Kean, "Very sensitive two photon absorption GaAs/AlGaAs waveguide detector for an autocorrelator", *Electron. Lett.*, Vol. 28, pp. 1663-1665, 1992.
- [2] F. R. Laughton, J. H. Marsh, D. A. Barrow, and E. L. Portnoi, "The two photon absorption semiconductor waveguide autocorrelator", *IEEE J. Quantum Electron.*, Vol. 30, pp. 838-845, 1994.
- [3] E. Kapon and R. Baht, "Low loss single-moded GaAs/GaAsAl optical waveguides grown by organo-metallic vapour phase epitaxy", *Appl. Phys. Lett.*, Vol. 50, pp. 1628-1630, 1987.
- [4] R. A. Smith, "Semiconductors", Cambridge University Press, 1986.
- [5] G. H. Ames and D. G. Hall, "Attenuation in planar optical waveguides: Comparison of theory and experiment", *IEEE J. Quantum Electron.* Vol. 19, pp. 845-853, 1983.
- [6] K. H. Park, Y. T. Byun, Y. Kim, S. H. Kim, S. S. Choi , and Y. Chong, "Dependence of propagation loss on etching depth in $\text{Al}_{0.3}\text{Ga}_{0.7}\text{As}/\text{GaAs}/\text{Al}_{0.3}\text{Ga}_{0.7}\text{As}$ strip-loaded type waveguides", *Opt. Quantum Electron.*, Vol. 27, pp. 363-369, 1995.
- [7] R. J. Deri, R. J. Hawkins, and E. Kapon, "Rib profile effects on scattering in semiconductor optical waveguides", *Appl. Phys. Lett.*, Vol. 53, pp. 1483-1485, 1988.
- [8] P. K. Tien, "Light waves in thin films and integrated optics", *Appl. Opt.*, Vol. 10, pp. 2395-2413, 1971.
- [9] A. J. N. Houghton, D. A. Andrews, G. J. Davices, and S. Ritchie, "Low-loss optical waveguides in MBE-grown GaAs/GaAlAs heterostructures", *Opt. Comm.*, Vol. 46, pp. 164-166, 1983.
- [10] M. Haruna, Y. Segawa, and H. Nishihara, "Nondestructive and simple method of optical-waveguide loss measurement with optimisation of end-fire coupling", *Electron. Lett.*, Vol. 28, pp. 1612-1613, 1992.

- [11] R. G. Walker, "Simple and accurate loss measurement technique for semiconductor optical waveguides", *Electron. Lett.*, Vol. 21, pp. 581-583, 1985.
- [12] A. Yariv, "Optical Electronics", Chap. 6, CBS College Publishing, 1985.
- [13] E. Hecht, "Optics", Second Edition, Addison Wesley Publishing, 1989.
- [14] We would like to thank M. R. S. Taylor of Glasgow University for the use of the vector finite difference computer program.
- [15] H.C. Casey, Jr, D. D. Sell, and K. W. Wecht, "Concentration dependence of the absorption coefficient for n-and p-type GaAs between 1.3 and 1.6 eV", *J. Appl. Phys.*, Vol. 46, pp. 250-257, 1975.
- [16] H. C. Casey, Jr, and M. B. Panish, "Heterostructure Lasers", Part A, Academic Press, New York, 1978.
- [17] J. D. Dow and D. Redfield, "Toward a unified theory of Urbach's Rule and exponential absorption edges", *Phys. Rev. B*, Vol. 5, pp. 594-610, 1972.
- [18] P. K. Bhattacharya and S. Subramanian, "Correlation of photoluminescence and deep trapping in metal organic chemical vapour deposited $\text{Al}_x\text{Ga}_{1-x}\text{As}$ ($0 < x < 0.40$)", *J. Appl. Phys.* Vol. 55, pp. 3664-3668, 1984.
- [19] K. Akimoto, M. Kamada, K. Taira, M. Arai, and N. Watnabe, "Photoluminescence killer centre in AlGaAs grown by molecular beam epitaxy", *J. Appl. Phys.*, Vol. 59, pp. 2833-2836, 1986.
- [20] L. M. Smith, S. A. Rushworth, A. C. Jones, J. S. Roberts, A. Chew and D. E. Sykes, "Oxygen incorporation in aluminium-based semiconductors grown by metal organic vapour phase epitaxy", *J. Crystal Growth*, Vol. 134, pp. 140-146, 1993.
- [21] D.C. Hutchings and B. S. Wherrett, " Theory of anisotropy of two-photon absorption in zinc-blende semiconductors", *Phys. Rev. B*, Vol. 49, pp. 2418-2426, 1994.

Chapter 6

Two-Section Semiconductor Laser

6.1 Introduction

Semiconductor lasers are everywhere. They can be found at the bottom of the ocean in long-haul telecommunications systems, in orbit around the earth in remote sensing apparatus, in domestic living rooms and cars within disc players.

Laser action in a semiconductor was first reported almost simultaneously by four groups nearly four decades ago [1-4]. All lasers were fabricated from the III-V compound semiconductor gallium arsenide (GaAs). Further advances over the next few years converted the semiconductor laser from a laboratory curiosity to a practical, coherent light source having numerous functions.

In 1964, Lasher [5] proposed a two section bistable laser consisting of a Fabry-Perot injection laser with two electrically isolated p-contacts. One contact was to have an injection current passed through it; the other biased in such a way that it 'acts as a non-linear absorber of light'.

The technological progress of semiconductor lasers had received considerable impetus in 1966 due to a paper by Kao and Hockham [6] which suggested that an optical fibre made from silica might have potentially low loss to permit long distance transmission. Further work showed that the transmission wavelengths for the lowest loss and signal dispersion were 1.55 μm [7] and 1.3 μm [8], respectively.

Basov [9] in 1968 investigated two optically connected GaAs homojunction diodes, and observed self-sustained pulsations under conditions that one of the diodes absorbed and another amplified. Self sustained pulsations were observed in aged and degraded GaAs/AlGaAs semiconductor lasers [10]. In 1979 Dixon and Joyce [11] suggested a possible model for sustained oscillations found in

GaAs/AlGaAs double heterostructure lasers. Shortly after this, in 1982, Harder *et al.* [12] observed bistability and pulsations at microwave frequencies in CW GaAs semiconductor lasers with inhomogeneous current injection, over fifteen years after Lasher first proposed such a device. Inhomogeneous current injection was achieved by using a twin segment contact. They showed experimentally that, depending on the electrical bias conditions, the negative differential resistance across the absorber leads either to a narrow hysteresis loop with self-sustained pulsations or to bistability with a large hysteresis loop without self-sustained pulsations. It is noted that optical bistability, as the name implies, refers to the situation in which two stable optical output states are associated with a single input state. Self-pulsation is a strong repetitive intensity change in output power at repetition rates of the order of GHz. However, future optical communication systems are expected to operate at multi-gigabit per second data rates, and optical signal processing will be of prime importance in this respect. Key elements for optical signal processing are bistable devices, and one class of particularly promising components are properly designed segmented laser diodes [13, 14].

Picosecond pulse generation technology in semiconductor laser diodes is important for high-speed optical communication systems. Short optical pulses from diode lasers transmit high quality voice, video and data through optical fibre. In optoelectronic measurement applications short optical pulses are used to test, measure or characterise systems. For example, they can be used to obtain the impulse response of optical materials and components, as in pump-probe experiments [15]. Short electronic pulses for electronic circuit testing can be generated by electro-optic sampling [16]. Laser ranging, optical time domain reflectometry and sensing can use short optical pulses from semiconductor lasers to measure distance with high accuracy for high precision manufacturing and for guiding and automatic collision avoidance systems.

In this Chapter one of the important methods of achieving ultra-short pulses (two-section Q-switched diode laser) at high frequency rates is investigated. Q-switched semiconductor diode lasers are of interest for applications in optical fiber communication systems, or more generally as sources of optical pulses when high peak power and large depth of modulation are required at high repetition rates [17]. For example, in fiber optical systems using pulse gated receivers, a higher peak output power would mean that the coupling between the fibre and the laser would be less important and the distance between repeater stations, or the range of the communications links, could be extended. The short pulse duration would also mean an increase in the bit-rate of modulation or an increased bandwidth.

In this Chapter, the band filling effect is first described, followed by a review of self-pulsation in semiconductor lasers along with a physical description of this ultra-short pulse generating technique. The results from passively Q-switched two section lasers will then be documented, followed by design and characterisation of high speed material. Finally, the temperature dependence of threshold current of material QT 683 is investigated.

6.2 Band Filling in Semiconductor Lasers

Electrons injected into the active region of a semiconductor laser have a finite lifetime. Since electrons are fermions, they obey the Pauli exclusion principle and so cannot occupy the same energy state as others in the crystal. This is well known for free electrons and holes. Therefore if electrons are injected at a faster rate than they can recombine, higher energy states in the conduction band will become occupied so resulting in an effective increase in the bandgap, known as the Burstein-Moss (band filling) effect [18]. Radiative recombination can occur from these higher states resulting in a broadened spontaneous emission spectrum. The density of states of the active region of the laser is one of the key parameters in determining the wavelength spectrum of the spontaneous emission. It was shown in Chapter 2 that the density of states for a quantum well is different from that of a bulk semiconductor. The density

of states is conventionally approximated by a parabola for bulk material but in a quantum well it has a 'step-like' structure. For a given energy above the lowest confined state in the quantum well, the number of available states is lower. Consequently, the density of states per unit volume of active region is lower, therefore, large band filling occurs in the electron quantum state.

Because of the differences in the density of states functions between bulk and quantum well material and assuming parabolic bands [19]:

$$\Delta E_{BULK} \propto N^{2/3} \quad (6.1)$$

$$\Delta E_{QW} \propto N \quad (6.2)$$

where ΔE is the range of filled energy states and N is the number of injected carriers per unit volume of active region. Thus for a given value of N , ΔE will be larger in quantum well material.

Qualitatively, consider injecting the same number of electrons per unit volume of active region into both bulk and quantum well structures to fill up a range of energy states ΔE_{BULK} and ΔE_{QW} . It is obvious that $\Delta E_{QW} > \Delta E_{BULK}$ due to the difference in the densities of states. Since a greater range of energy states is filled in the quantum well, a wider wavelength range of spontaneous emission may be expected. It has been shown that the rapid increase of gain at low injection levels and the pronounced saturation toward high injection levels results from band filling as a direct consequence of the step-like density of states function in the QW [20].

6.3 Two-section Q-switched Diode Laser

Two types of Q-switching that are generally used and are addressed here; active and passive Q-switching.

6.3.1 Active Q-switching

The normal configuration used for active Q-switching consists of two-section laser with the long section forward biased to produce gain in the device and the short section reversed biased to suppress lasing in the structure, as shown in Fig. 6.1(a). An RF modulated electrical signal is also applied to the short section so that the section acts as an intracavity electroabsorption loss modulator. The physical phenomena utilised are the quantum confined Stark effect [21] in the modulator section and the enhanced carrier-induced band shrinkage effect [22] in the optical amplifier section. The room temperature absorption spectrum of a MQW displays enhanced absorption at the band edge, with a double-peaked structure, caused by excitons whose binding energy is enhanced by the two dimensional confinement. When an electric field is applied to the quantum wells perpendicular to the layers, the exciton absorption peak shifts to lower energy (Section 2.4.2, Chapter 2). This effect is much larger than the Franz-Keldysh effect seen in bulk materials. The dominant mechanism is the decrease in confinement energies, resulting in a red shift of the excitonic absorption energy. The band discontinuities prevent the ionisation of the exciton, allowing excitonic resonances to be observed at room temperature with large applied fields. In addition, the carrier induced band shrinkage effect is enhanced in MQW lasers compared to conventional double heterostructure lasers, resulting in a decrease of the lasing photon energy by about 20 meV [22] compared to the intrinsic absorption edge. Consequently, the two phenomena resulted in extremely large loss changes which vary according to the application of an electric field to the modulator section.

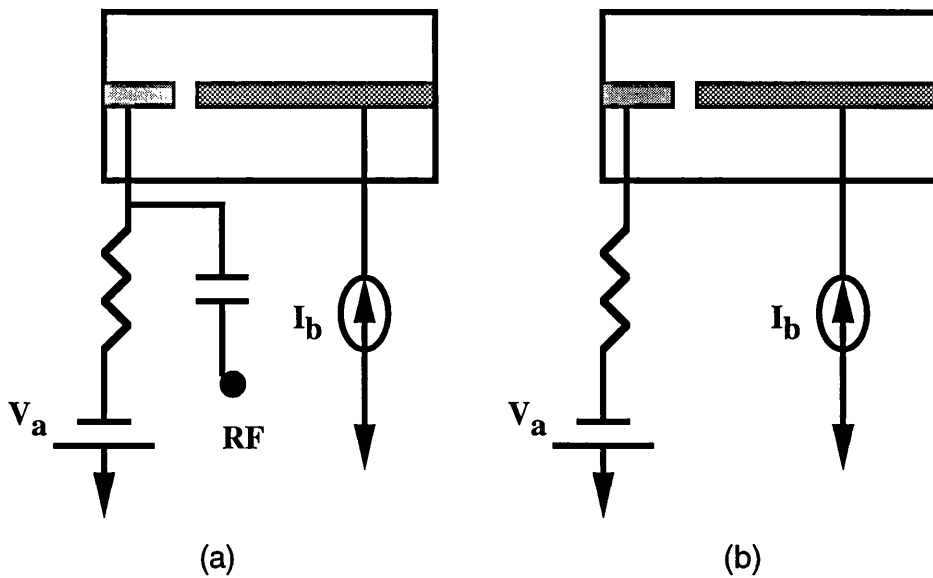


Fig. 6.1: Schematic diagram of two types of Q-switched diode laser: (a) active Q-switching (b) passive Q-switching.

When an electrical pulse is applied to the short section, the peak of the pulse forward biases the section, resulting in a narrow time window of low loss in the cavity for the optical pulse being emitted. The timing jitter of the emitted pulse train is lower than for passive Q-switching (Section 6.3.2) due to the presence of a high stability driving source. It has been shown that a pulse width as narrow as 18.6 ps FWHM at a repetition rate of more than 3 GHz can be produced by active Q-switching in a GaAs/AlGaAs MQW laser [23]. The pulse width was observed to be dependent on the current which was injected into the amplifier section, decreasing with increasing injected current. A standard double heterostructure GaAs/AlGaAs two section laser producing actively Q-switched pulses of 15 ps FWHM wide at a repetition frequency of 1 GHz has been reported [15]. The measured pulse energy was 4 pJ and the spectral width was 2.4 THz which gave a high time-bandwidth product of 36.

6.3.2 Passive Q-switching (Self-Pulsation)

Passive Q-switching is known as one of the simplest techniques for generating picosecond optical pulses in diode lasers. A feature of semiconductor diode lasers is their ability to allow ready incorporation of saturable absorbers of the same material as the active medium of the laser. Passive Q-switching or self-pulsation in laser

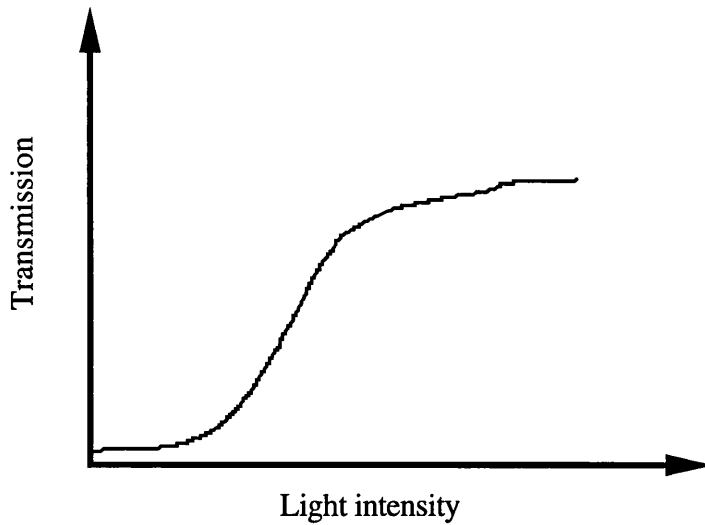
diodes is caused by instabilities induced by regions of saturable absorption coupling with regions of high gain. The fundamental difference between the two techniques, i.e. active and passive Q-switching, is that in contrast to active Q-switching no external electrical or optical modulation is required to produce ultra-short optical pulses. In the case of active Q-switching the pulse repetition frequency is set by an external RF or optical signal, whereas for passive Q-switching the frequency is governed by the laser parameters and pumping conditions. A standard configuration for a passively Q-switched two-section laser is shown in Fig. 6.1 (b). The long section is the gain section and the short section of the two section laser acts as a *saturable absorber*. The optical switching function is performed by a saturable absorber in passive Q-switching. This is a length of waveguide which is not pumped by the injected current (indeed it is usually reversed-biased). At low optical intensities, strong absorption takes place and the optical wave passing through the absorber is severely attenuated. Lasing is therefore inhibited. At high optical intensities the generation of electron-hole pairs occurs at a much higher rate than recombination and band-filling take place. When sufficient states in the bands are filled (with electrons and holes), the rate at which absorption transitions can take place falls and the absorption coefficient within the absorber drops—i.e. the absorption saturates. A high intensity optical pulse therefore experiences much lower attenuation than a low intensity pulse.

In the two section laser described above, the long section is forward biased to provide gain and the absorber region is reversed biased to reduce its recovery time. Population inversion builds up in the active region and, eventually, an optical noise spike is amplified to the point where the absorber saturates and a large optical pulse is emitted. The length of the pulse is determined by the length of time taken for the population inversion to be depleted. The repetition rate of the pulses is determined by the length of time taken for the gain region to recover. The repetition frequency can therefore be tuned by altering the drive current to the device.

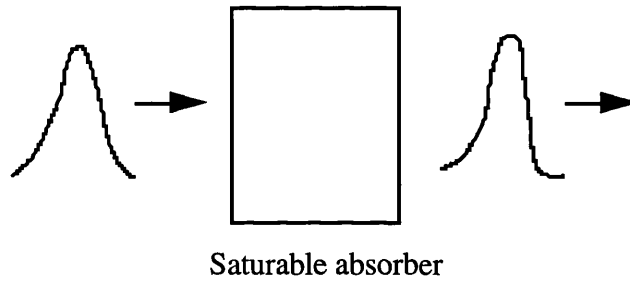
6.3.2 Description of Self-Pulsating Behaviour

It is well known that saturable absorption introduced into a semiconductor laser cavity plays an important role in the dynamic behaviour of a semiconductor laser, and can cause bistable operation or self-pulsations. The effect on the dynamic stability is due to the non-linear relationship between the gain and the carrier density.

The action of a saturable absorber is illustrated in Fig. 6.2 (a). As a result of the non-linear transmission characteristics of the absorber, the initial amplitude distribution of the light is distorted when a light beam is passed through it. The passage of a light pulse leads to pulse shaping, as shown in Fig. 6.2 (b). The absorption of the leading edge of the pulse is increased as compared with the trailing edge, the peak-to-peak ratio of the initial amplitude fluctuation of the beam being increased and its time duration being decreased as a result of the non-linear transmission characteristics of the absorber. This process is repeated over and over again by reflecting the light back and forth between the laser mirrors, which leads to the generation of asymmetric ultra-short pulses.



(a)



(b)

Fig. 6.2: Typical transmission characteristic of a saturable absorber and illustration of pulse shaping by the absorber.

To generate self-sustained pulsations or self-Q-switched pulses, the saturable absorber in the laser cavity must satisfy a number of conditions. The most important parameters that affect the dynamic behaviour of the laser are the ratio of the differential loss da/dn of the absorber to the differential gain dg/dn of the amplifier section and the ratio of the carrier lifetime in the gain τ_g and the absorber τ_a sections. It can be shown [11, 24] that in order to generate Q-switched pulses the following conditions should be satisfied:

$$\frac{da/dn}{dg/dn} > 1 \quad (6.1)$$

and

$$\tau_a/\tau_g < 1 \quad (6.2)$$

Owing to the non-linear dependence of gain/absorption on the carrier concentration in diode lasers, as illustrated in Fig. 6.3 [25], the values of dg/dn and da/dn can be controlled by using different current inputs applied to different sections of the laser. As a result, the pulsewidth, the peak power, and the repetition rate are dependent on the driving currents. Ranges of parameters τ_g , τ_a , dg/dn , da/dn and current densities where self-Q-switching occurs can be calculated using the simple rate equations [24].

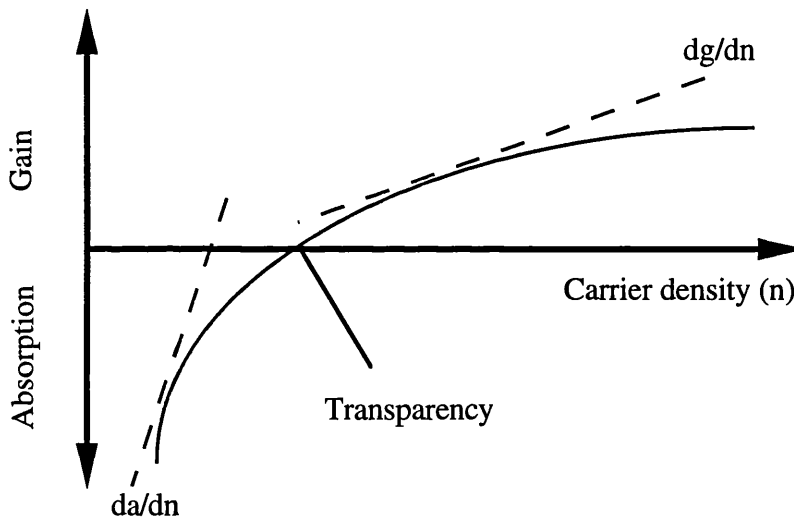


Fig. 6.3: Saturation characteristics of the modal gain (gain or absorption) in semiconductors as a function of carrier density. The differential gain is represented by dashed lines.

Fig. 6.4 illustrate the time dependence of the gain and loss in the laser cavity and shows how self-sustained pulsations are formed. Initially, before the formation of the pulse, section (a) of Fig. 6.4, the loss is greater than the gain. Any spontaneous emission produced in the laser cavity is absorbed by the saturable absorber. The gain builds up and eventually exceeds the unsaturated loss (a). At this point the leading edge of a pulse is formed from noise; at the same time the saturable absorber bleaches and the loss drops to the unsaturable loss (b), the loss due to mirror transmission, free carrier absorption, waveguide loss etc. As the intensity of

the pulse increases, the gain drops, however because the loss saturates faster than the gain, the central part of the pulse is amplified. When the gain reaches saturation below the unsaturable loss, the trailing edge of the pulse experiences net loss. If the recovery time of the loss is faster than that of the gain, then the loss will remain higher than the gain everywhere except near the peak of the pulse.

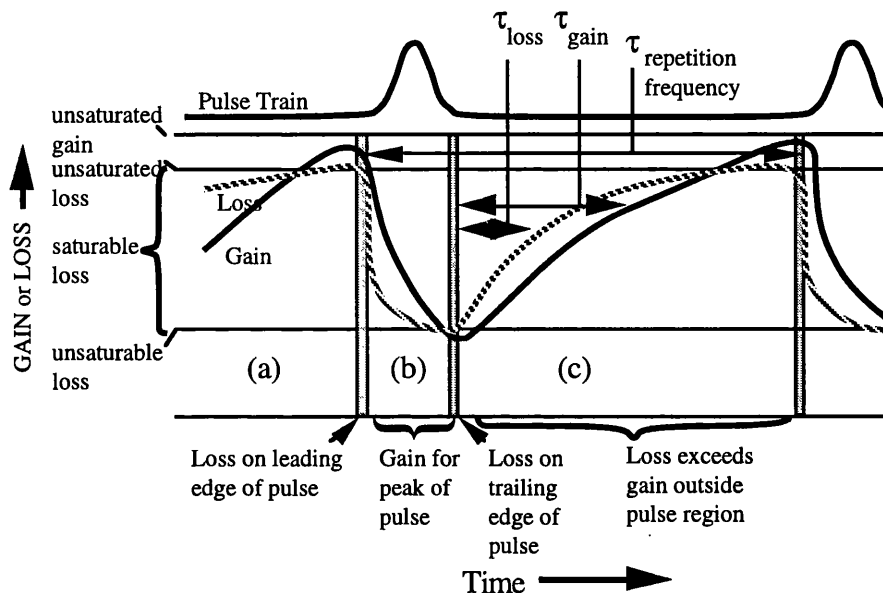


Fig. 6.4: Gain and loss dynamics for self-pulsation.

Although the formalism is very similar to modelocking, the physics of self-pulsating is very different. In the case of mode-locking the pulse is shorter than the cavity round trip time and travels back and forth being repetitively shaped by the action of the gain and absorber [26]. The repetitive shortening of the pulse is limited by dispersive pulse broadening which occurs as the pulse travels through the cavity. Passive Q-switching produces pulses that are longer than the cavity round trip time, which means that the laser can be treated as a lumped element [27]. The pulse builds up from noise and is shaped by the action of the gain and absorber, however, unlike mode-locking, it is not repetitively shaped. Therefore, it is not required to include dispersion when determining the equilibrium pulse shape.

Investigations of gain saturation mechanisms have shown it to have a strong effect on laser diode dynamics [28]. Gain saturation is due to effects such as dynamic

carrier heating and spectral hole burning. It has been shown that the effect of gain saturation on Q-switched behaviour is that the pulsewidth increases linearly with increasing gain saturation coefficient, while the peak power decreases [29]. However, gain saturation does not greatly influence the repetition rate of output pulses.

6.4 Device Fabrication

Passive Q-switching is a very attractive method to produce ultra-short optical pulses with high peak powers. This is usually attained in a two-segment laser consisting of an optical amplifier and an electroabsorption loss modulator. The amplifier is driven by injection current while the modulator section makes use of the quantum confined Stark effect. The two section diode laser with a monolithic intracavity saturable absorber is illustrated in Fig. 6.5.

This section covers the fabrication of monolithic two-section lasers, from the description of the wafer used, up to mounting the device for tests. Section 6.4.1 describes the semiconductor material structure used in the two-section Q-switched lasers, whereas in Section 6.4.2 every process step of fabrication of the lasers is described in detail.

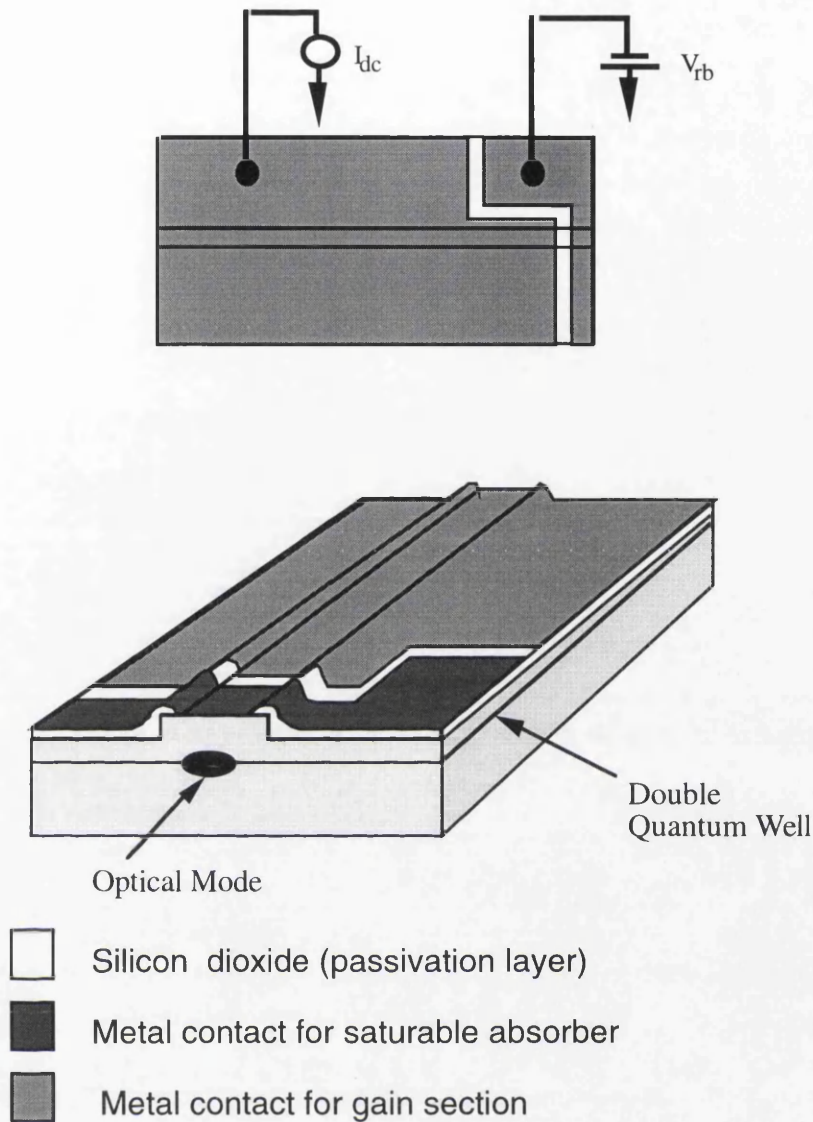


Fig. 6.5: Schematic diagram of the two section laser configuration.

6.4.1 Material Structure

The lasers were fabricated using a wafer (QT 674) which included an active layer containing an InGaAs/GaAs double quantum well, grown by metal organic vapour phase epitaxy (MOVPE) in Sheffield University. The semiconductor material structure consisted of a $0.3\ \mu\text{m}$ thick, heavily P-doped with zinc ($5.5 \times 10^{18}\ \text{cm}^{-3}$) GaAs cap layer. This was followed by a $1.2\ \mu\text{m}$, p-type, carbon doped ($1.2 \times 10^{18}\ \text{cm}^{-3}$) $\text{Al}_{0.57}\text{Ga}_{0.43}\text{As}$ upper cladding layer; a $0.15\ \mu\text{m}$ graded $\text{Al}_x\text{Ga}_{1-x}\text{As}$ waveguide region, with $0.2 \leq x \leq 0.57$ (undoped); the quantum well structure consisting of two $10\ \text{nm}$ $\text{In}_{0.2}\text{Ga}_{0.8}\text{As}$ wells spaced by three $25\ \text{nm}$ GaAs

barriers; a 0.15 μm graded $\text{Al}_x\text{Ga}_{1-x}\text{As}$ lower waveguide region, $0.57 \geq x \geq 0.2$ (undoped); and the lower cladding layer was formed by $\text{Al}_{0.57}\text{Ga}_{0.43}\text{As}$ silicon n-doped ($1.5 \times 10^{18} \text{cm}^{-3}$) layer with 1.2 μm thickness. A GaAs substrate and a 1 μm thick GaAs buffer layer, both n-doped with silicon ($1 \times 10^{18} \text{cm}^{-3}$), were used.

6.4.2 Fabrication Technique

The technique employed to fabricate the two section Q-switched semiconductor lasers is described here, step by step, starting from the scribing of the semiconductor wafer up to the point where the laser is ready for tests. The general technology and processes for semiconductor device fabrication can be found in reference 30. The fabrication procedure is:

- 1) Sample cleaving: The wafer was scribed into $8 \times 8 \text{ mm}^2$ pieces using the wafer scriber. The cleavage must follow the crystal orientation of the semiconductor material.
- 2) Sample cleaning: by immersion in the organic solvents: opticlear, methanol and acetone, in this order, in an ultrasonic bath for 5 minutes for each solvent. This was followed by R. O. (reverse osmosis) water rinsing and nitrogen blow drying.
- 3) Silica deposition: the sample was then coated with a thin mask layer of silica (2000 Å) in a plasma enhanced chemical vapour deposition machine (PECVD), to serve as a hard mask for the dry etching process (with SiCl_4) that will form the waveguide.
- 4) Resist spinning: using photoresist S1400-17 spun at 4000 rpm for 30 seconds. This is a positive photoresist and its final thickness was approximately 0.8 μm .
- 5) Resist baking: the sample with resist was place in an oven at 90 °C for 30 minutes.

6) Photolithography: The waveguide mask consisted of 15 stripes, each one being 3.5 μm wide and 10 mm long, separated from each other by 600 μm , so forming a 10 by 10 mm^2 mask. The sample was exposed for 4 seconds in mask aligner. The alignment of the waveguide stripes parallel to the cleavage edge of the sample is very important and critical to guarantee perpendicular laser facets at the laser cleaving stage. The sample was developed and washed in deionised water, then post-baked at 120 $^{\circ}\text{C}$, to harden the resist.

7) Dry etching: The silica was etched in a Plasmatech 80 reactive ion machine for 5 minutes, using C_2F_6 . The sample was then cleaned in acetone for 10 minutes and washed in R. O. water. The silica pattern left on the sample acted as a mask and was used to produce sharp edge definition of the etched waveguide. Then, reactive ion etching (RIE) using silicon tetrachloride (SiCl_4) was performed in order to form the waveguide. The best results were obtained at a forward rf power of 100 W and gas flow of 9 sccm, which has an etch rate of about 160 nm/min. Finally the silica mask was removed in buffered hydrofluoric acid.

8) Silica deposition: SiO_2 deposition by plasma enhanced chemical vapour deposition (PECVD)[31]. Layer thickness was 200 nm. This silicon dioxide layer was to serve as a current injection blocking layer. Then, sample was cleaned in acetone for 10 minutes and washed in R. O. water and blown dry using nitrogen.

9) Resist spinning: using photoresist S 1400-17 spun at 4000 rpm for 30 seconds, as in step 4.

10) Resist baking: sample with resist was placed in an oven at 90 $^{\circ}\text{C}$ for 30 minutes, as in step 5.

11) Photolithography: to open a current injection window on top of the waveguide using mask aligner. The thinner resist used makes the mask alignment easier than thicker ones, since the mask can come closer to the sample before touching the resist layer. The dark field ferric oxide mask consisted of a set of 2.5 μm wide stripes,

fitting the waveguide mask described in step 6. The sample was exposed for 6 seconds, then developed to open up a window in the resist above the waveguides.

12) Post- baking: sample with resist was placed in an oven at 120 °C for 30 minutes. The post-baking was required to harden the resist before etching.

13) Wet etching: wet chemical etching with hydrofluoric acid (HF) was used to remove the silicon dioxide layer from the top of the waveguide, opening a current injection window on it. The etch rate is approximately 10 nm/s, but 50% over-etching was used to ensure total removal of the silica. The etching time was 30 seconds. HF does not etch GaAs. Then, the sample was cleaned as in step 2.

14) Resist spinning: using photoresist S1400-31 spun at 4000 rpm for 30 seconds. This is a positive photoresist and its final thickness was approximately 1.8 μm . The sample was placed in the oven at 90 °C for 15 minutes, then immersed in chlorobenzene ($\text{C}_6\text{H}_5\text{Cl}$) for 15 minutes and finally baked again at 90 °C for 15 minutes. The use of thicker resist and chlorobenzene facilitated the lift-off of thick layers of metal. The sample was aligned and exposed for 12 seconds and then developed and washed.

15) Deoxidising etch: with HCl and water (HCl—4, H_2O —1) for 30 seconds, to remove any surface oxidation of the P^+ GaAs contact layer. It improved considerably the adhesion of the metal to the silica layer as well as the electrical properties of the contact. Poor adhesion of the metal to the silica layer underneath makes gold wire bonding to the contact pads very difficult.

16) Top metalisation: deposition of p-type metallic contact by evaporation at a vacuum pressure of 2×10^{-6} torr. An ohmic contact was formed with the deposition of Ni/Au (60 nm nickel and 150 nm of gold). The use of an ohmic contact is an important issue for semiconductor Q-switched lasers since, in the saturable absorber section, carriers are to be removed with minimal electrical resistance by reverse biasing the section. In order to have uniform metal deposition on the walls of the waveguide the

evaporation was performed with the sample tilted by +45 degrees to one side and -45 degrees to the other side of the waveguide. Then, for lift-off, the sample was immersed in acetone and washed.

17) Substrate thinning: using the resist S1400-31 to protect the top of the sample, with waveguide and metallic contacts, prior to the thinning process. The sample was mechanically hand polished using 9 μm and 3 μm Al_2O_3 grit to reduce the substrate thickness to approximately 150 μm , and then refluxed in the organic solvents. This was followed by a R. O. water rinse and nitrogen blow drying.

18) Deoxidising etch: as in step 15.

19) Metallisation: deposition of n-type metallic contact by evaporation. An ohmic contact was formed by the deposition of Au/Ge/Au/Ni/Au (14 nm of gold, 14 nm of germanium, 14 nm of gold, 11 nm of nickel and 200 nm of gold). Fig. 6.6 shows the cross-section of the sample at the waveguide at this stage of fabrication.

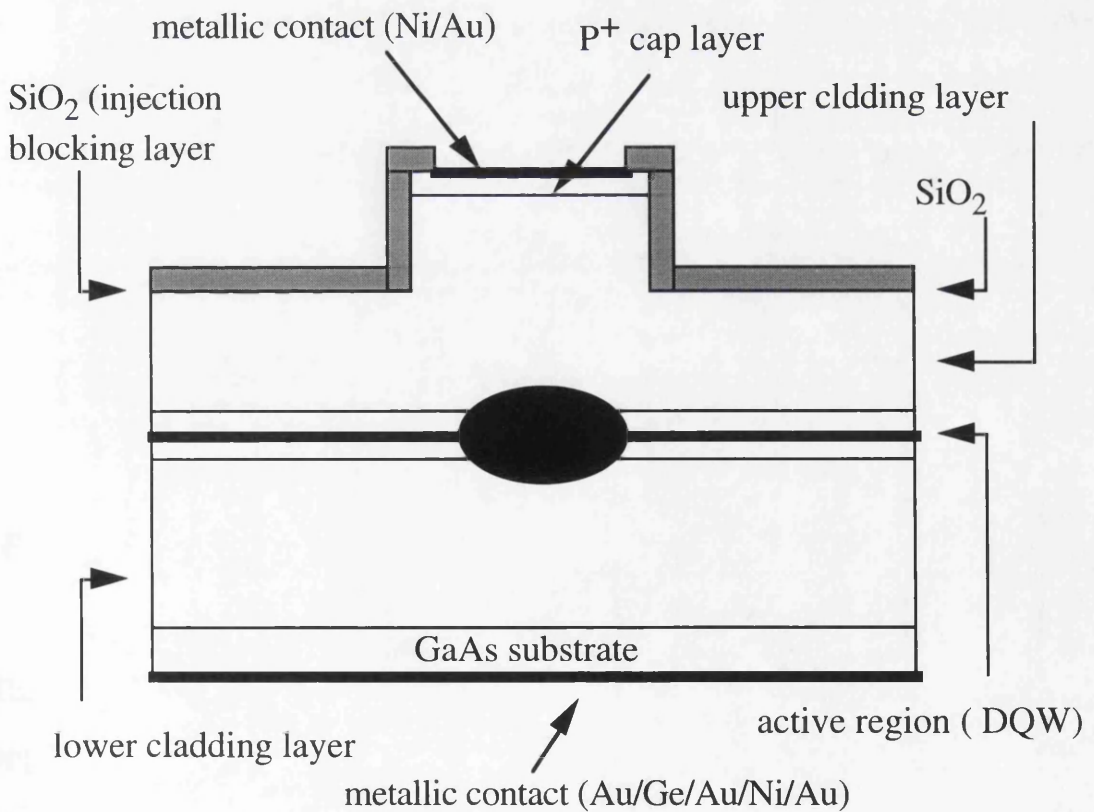


Fig. 6.6: Cross-section of the laser at the waveguide. The layers of the material structure and metallic layers deposited during the fabrication process are shown.

20) Wet etching: to improve the electrical isolation between sections. The electrical isolation between gain and absorber sections is an important issue on the design and fabrication of semiconductor Q-switched lasers. The isolation can be improved by removing the highly doped GaAs cap layer from the gap region between the sections using wet etching ($\text{NH}_3\text{-H}_2\text{O}_2$; 1-20) for 6 seconds, which stops on the AlGaAs layer. By measuring the resistance between gain and absorber sections when no bias was applied, a DC electrical isolation of about $4.7 \text{ k}\Omega$ was obtained after wet etching. A typical result is illustrated in Fig. 6.7.

These measurements were made with a Hewlett Packard 4145A semiconductor parameter analyser.

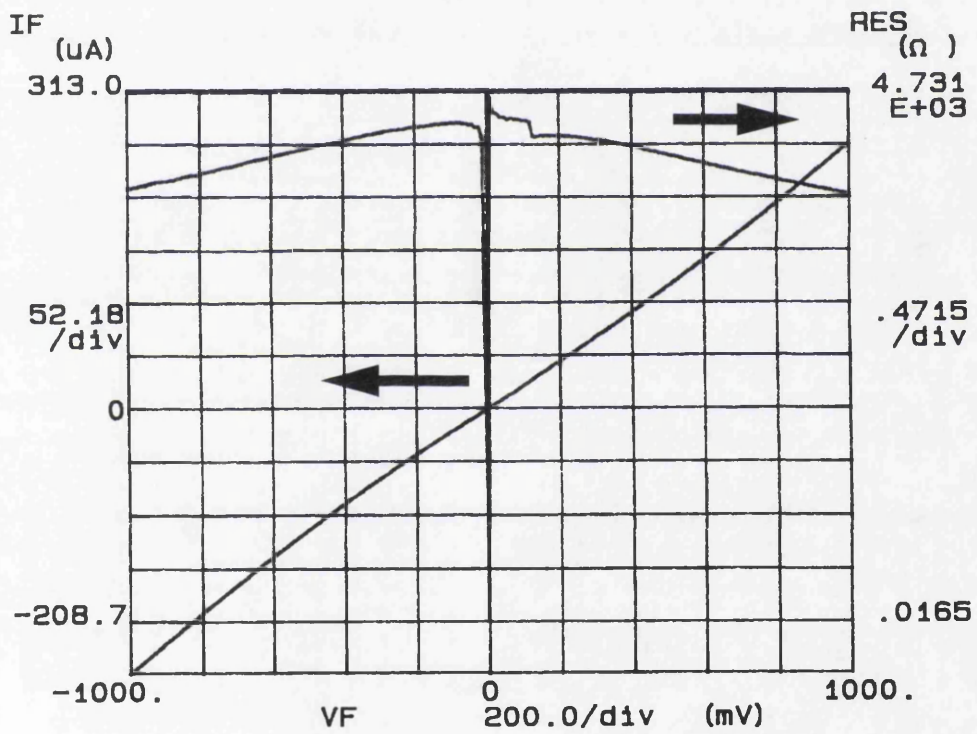


Fig. 6.7: Plot of current/voltage (lower arrow) and resistance/voltage (upper arrow) between the two sections.

The lower arrow in Fig. 6.7 shows the voltage/current curve (left hand axis), the upper curve (right hand axis) illustrates the dynamic resistance against voltage calculated from the voltage/current curve. Both curves are close to linear indicating that the contact is ohmic.

21) Laser cleavage: using the wafer scribe. The lasers had to be cleaved individually, therefore the scribing of the optical facet of the lasers was performed first. The cleavage of the optical of each laser is accomplished by aligning the scribe with one of the edges. The non-optical facet of the laser was then cleaved.

22) Laser soldering: by indium soldering. For CW operation the laser had to be mounted on a base that provided proper heat sinking. The base used was a copper block coated with 60 nm nickel and 200 nm gold. The laser was soldered to the base with indium. The softness of the indium solder absorbs the strain caused by the different thermal expansion coefficient between the semiconductor and metal base.

23) Wire bonding: gold wire (20 μm thick) bonding was made from the contact pads on the laser to the pads on the laser mounting, from which the electrical connections to the power supplies were to be made. The ultrasonic bonding was performed with a Kulicke & Soffa 4123 wedge bonder. After wire bonding, the laser was ready for tests. Fig. 6.8 shows the two-section laser after bonding.

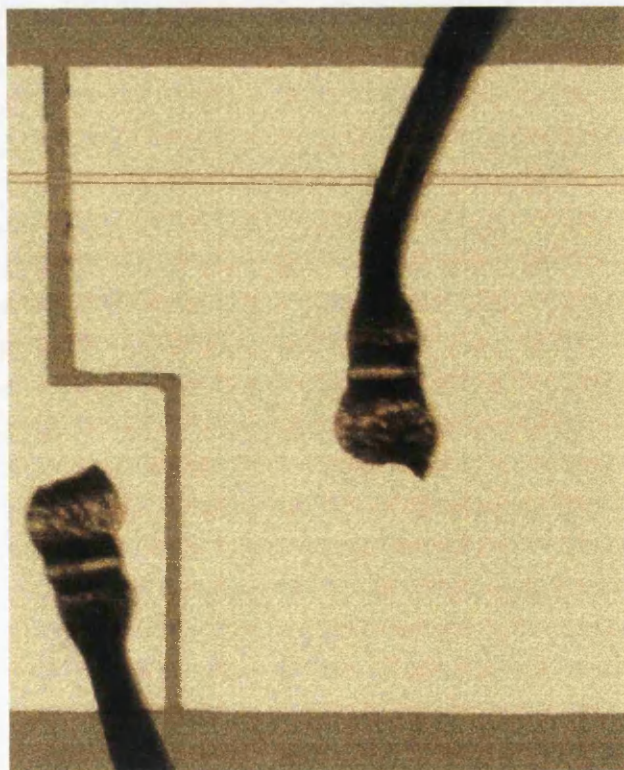


Fig. 6.8: Photograph of the two-section laser used for the Q-switched laser.

6.5 Testing

The two-section lasers were initially tested in a pulse regime with a mark space ratio of 2500:1 before selecting those with the best characteristics for mounting onto heat sinks and wire bonding. Also important in the characterisation of semiconductors is to obtain the output optical power, the threshold current and current density, and lasing efficiency. This was carried out by measuring the output power as a function of injected current (L-I curve).

This section describes the techniques employed to characterise the fabricated two-section Q-switched lasers.

6.5.1 Experimental Set-up

Figure 6.9 shows the experimental set-up used to test lasers. The rig is fully automated and is controlled from an Apple Mac computer using Lab View (a commercial software package from National Instruments) which allows accurate measurements to be taken very quickly.

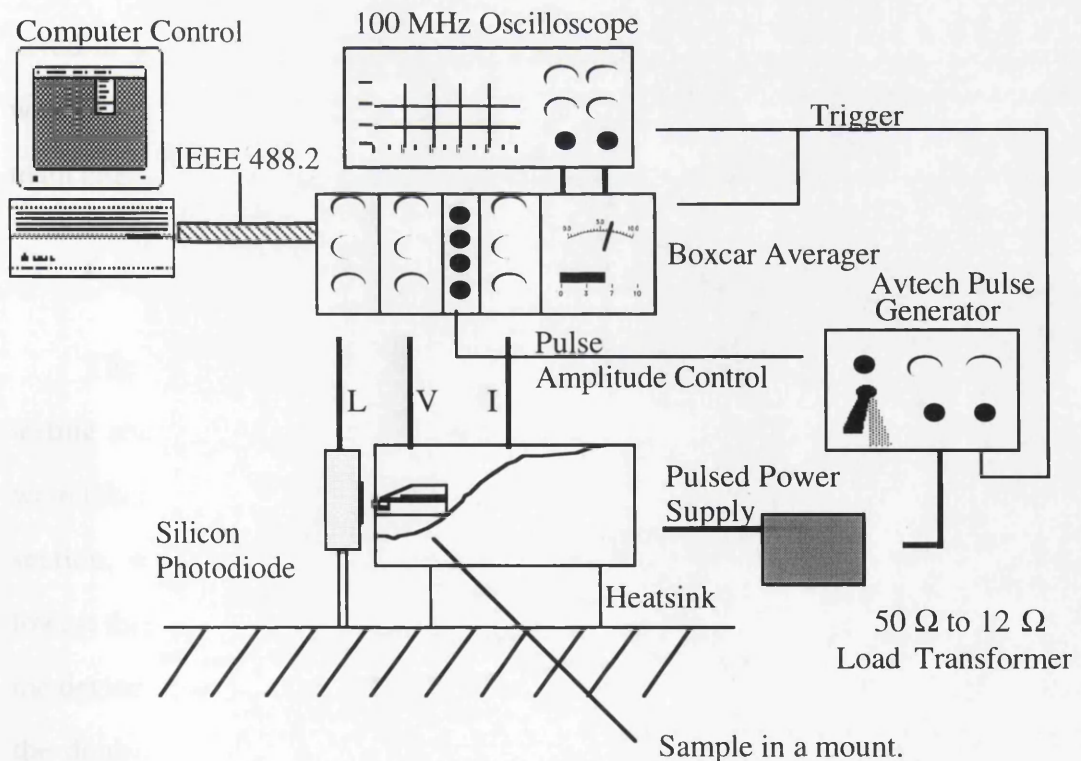


Fig. 6.9: Experimental set-up for measuring laser characteristics.

The current supply is an Avtech pulse generator which has an adjustable pulse width and repetition rate. All pulse measurements in this Chapter were carried out using a 400 ns pulse at a 1 kHz repetition rate (i.e. a duty cycle of 0.04 %). The pulse generator can be controlled manually which allows the lasers to be tested very quickly (to see if they work) before taking any accurate measurements. Between the signal generator and the laser there is a variable attenuator and a transformer which allows a wide range of currents to be supplied to the devices (0–4 A).

The electrical contacts to the devices were made by clamping the laser in a spring-loaded, gold-plated clip, p-side down, in such a way that the output of only one facet was monitored by the detector. Because of the lasing wavelengths under investigation, the detector used was a Silicon photodiode which was reversed biased at 4.5 V. A box car integrator was used to recover the pulse analogue signal from the photodetector. It averages the measurements over a number of cycles which reduces the noise from the signal. This data is then transferred to the computer via an IEEE GPIB which then calculates the current through the laser, the voltage across the laser and the power output from the laser. The data is also displayed on the screen and saved in memory. The output of the box car is also monitored by an oscilloscope which looks at the current through the laser and the output from the detector and is the main indicator to the operator that the laser is working.

6.5.2 Device Characterisation

The sample was scribed into individual devices of 400 μm cavity length, for testing and assessment. The current-light characteristics of all the lasers fabricated were taken after scribing. The lasers were tested using the laser rig described in last section, with both sections of the p-contact forward biased. The lasers with the lowest threshold currents and best quantum efficiencies were chosen in determining the device and material parameters. A typical light-current result for material QT 674, the double quantum well structure grown by MOCVD at Sheffield, is shown in Fig. 6.10; the threshold current is around 9 mA and the quantum efficiency is

around 20 % per facet. Because of imperfections in material and processing, all lasers do not have similar characteristics. The threshold currents of the devices with both contacts forward biased were very low, ranging from 9 to 16 mA.

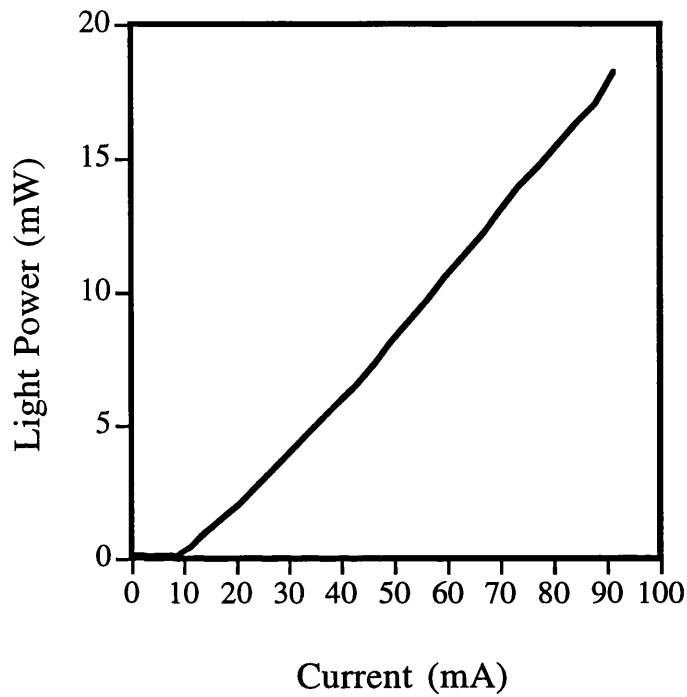


Fig. 6.10: Light-Current characteristic for material QT 674

Figure 6.11 shows a typical Current-Voltage characteristic of a mounted laser with a dynamic resistance of 15 Ω .

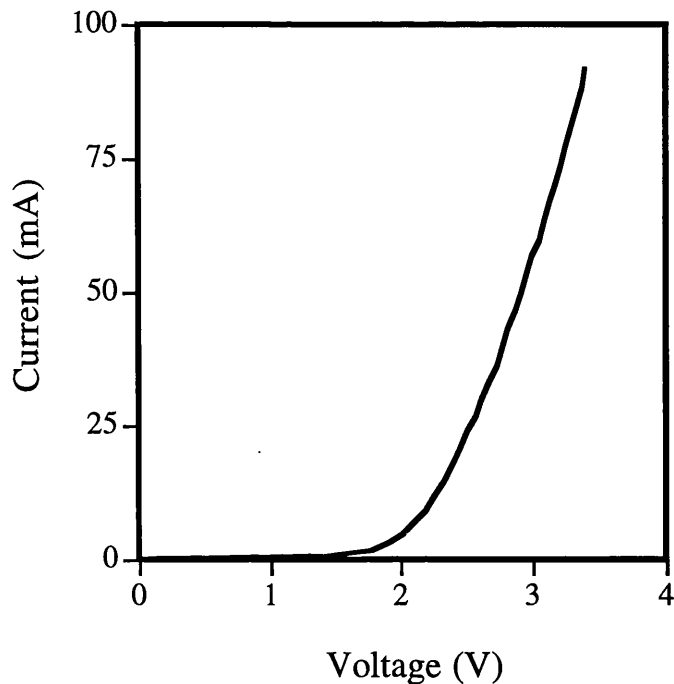


Fig. 6.11: Current-Voltage characteristic for material QT 674.

Future studies of new metallic contact recipes should lead to improvements on the dynamic resistance, with benefits to the overall laser operation, such as lower forward voltage and higher efficiency.

6.5.3 Optical Spectra

The optical spectra of the devices were observed at various levels of reverse bias. This experiment showed what impact an increase in reverse bias in absorber section had on the lasing characteristics of the self-pulsating laser diode.

The laser was tested under a pulsed regime. The gain section of the laser was driven with 2 ns pulses of 130 mA whose amplitude was kept constant while the saturable absorber voltage was varied between 0 and 2.44 V.

The full width at half maximum (FWHM) of the optical spectrum changes from around 1 nm at zero bias to around 2.5 nm at 2.44 V. This broadening of the spectrum is due to the effect of the self-pulsations in the laser; as the reverse bias is increased the self-pulsations become clearly defined and the pulses narrow. As the

temporal profile of the pulse narrows, a corresponding increase in the spectral width occurs. This relationship can be explained and described by the inverse Fourier transform theorem (Eq. 4.2, Chapter 4), therefore, to form a shorter pulse more longitudinal modes are needed. The effect of the reverse bias in wavelength of the laser can be explained by the fact that the absorption peak of the saturable absorber shifts to a longer wavelength, as predicted by the Stark Effect [21].

6.5.4 Testing the Devices under Self-Pulsation

With both sections electrically bonded, the device could be tested for self-pulsation. The experimental set-up is illustrated in Fig. 6.12, where the laser was driven by a pulse generator. The advantage of this method was that the sampling oscilloscope was triggered directly from the pulse generator. In this arrangement, the output from the laser diode was collected by a collimating lens and focused onto a fast photodetector via a single mode fibre. The output from the detector was connected to the sampling head of a sampling oscilloscope.

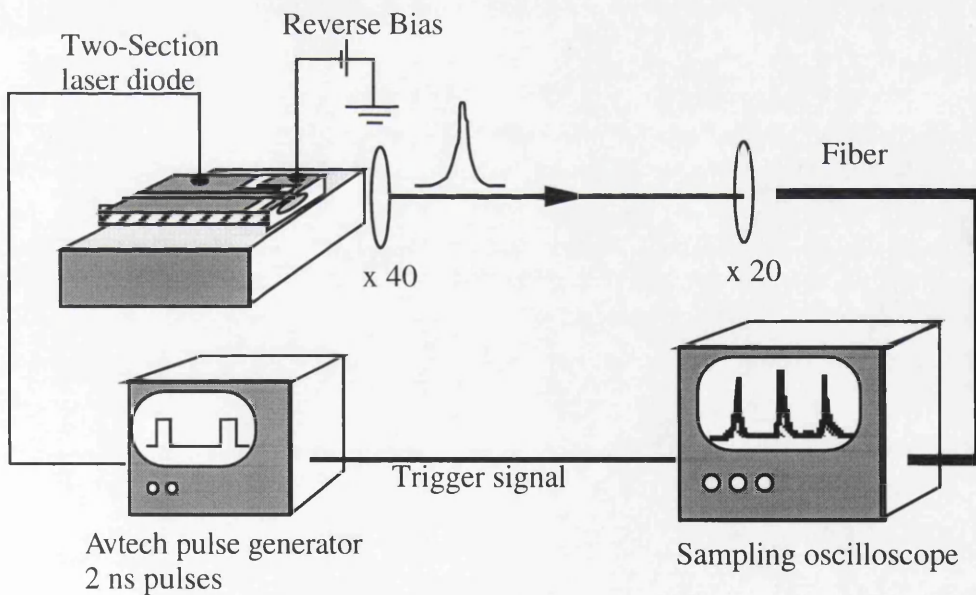


Fig. 6.12: Schematic diagram of experimental set-up for pulsed measurements.

The sampling oscilloscope was triggered from the pulse generator via a delay line so that, by varying the delay, the pulse appeared on the sampling oscilloscope. The main disadvantage of this method was its poor time resolution, which depends

on the rise time of the photodetector and the sampling head. The photodetector's bandwidth was 18 GHz and the sampling head has a bandwidth of 50 GHz, therefore the best resolution expected from this arrangement was around 30 ps. The gain section was pumped using an Avetech pulse generator which supplied a 2 ns pulse with a rise time of 300 ps driven at 10 kHz. A reverse bias of between 0 and 7 V was supplied to the absorber section.

6.5.5 Temporal Measurements

Initially the bonded lasers were measured in a pulsed regime using the laser test rig illustrated in Fig. 6.12. The pulses detected by a photodetector, with a frequency response of 18 GHz, were then sampled using a communication signal analyser (Tektronics CSA 402). When no reverse bias is applied the relaxation oscillations, which arise from the coupling between the optical field and the carriers in the active layer of the device, are clearly visible. A typical result is shown in Fig. 6.13. The relaxation oscillation frequency data is obtained by taking the inverse of the separation between the first and the second spike of the optical output.

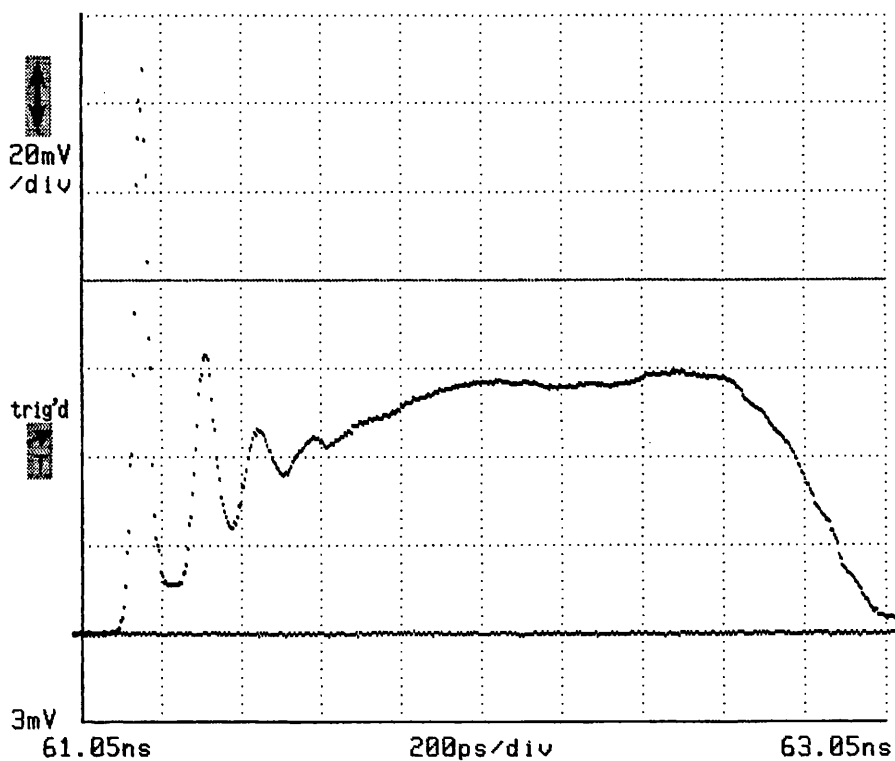


Fig. 6.13: Trace of relaxation oscillation of two-section laser.

The relaxation oscillations in these devices are stronger than would normally be observed due to the absorption effects in the unpumped section. As the reverse bias is increased, the pulse train becomes more well resolved. A typical result from a device self-pulsating at around 5 GHz with a reverse bias of 2.4 V across the absorber section, is shown in Fig. 6.14.

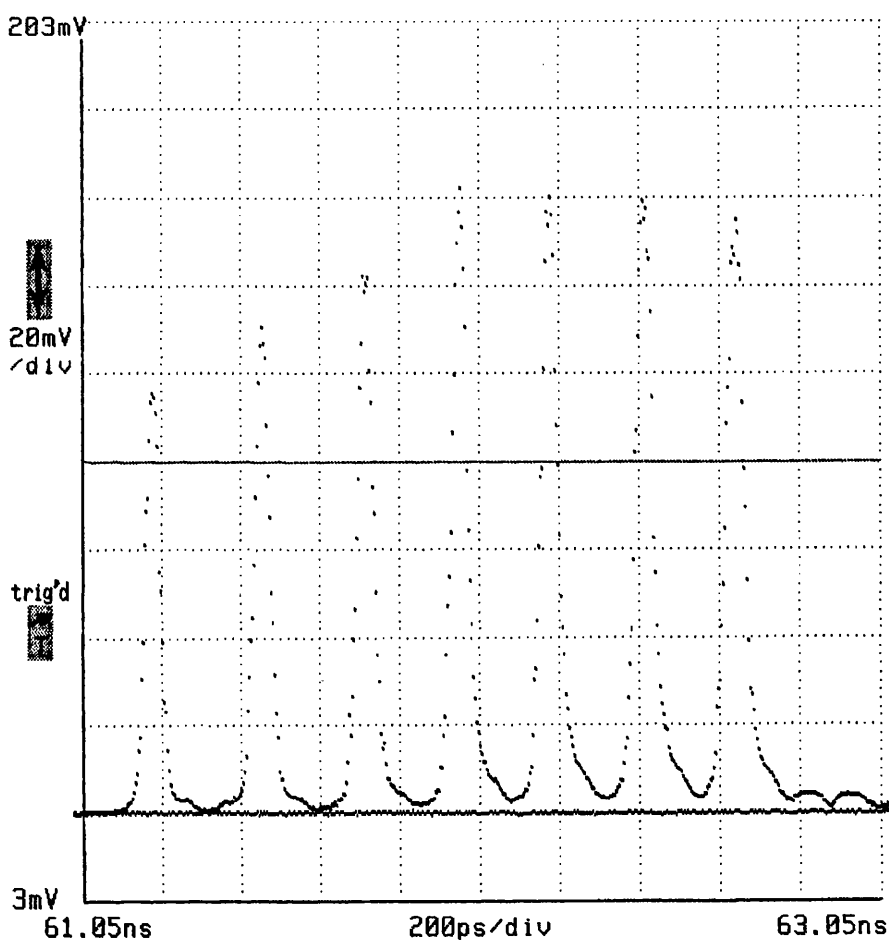


Fig. 6. 14: Trace of self-pulsation of two-section laser.

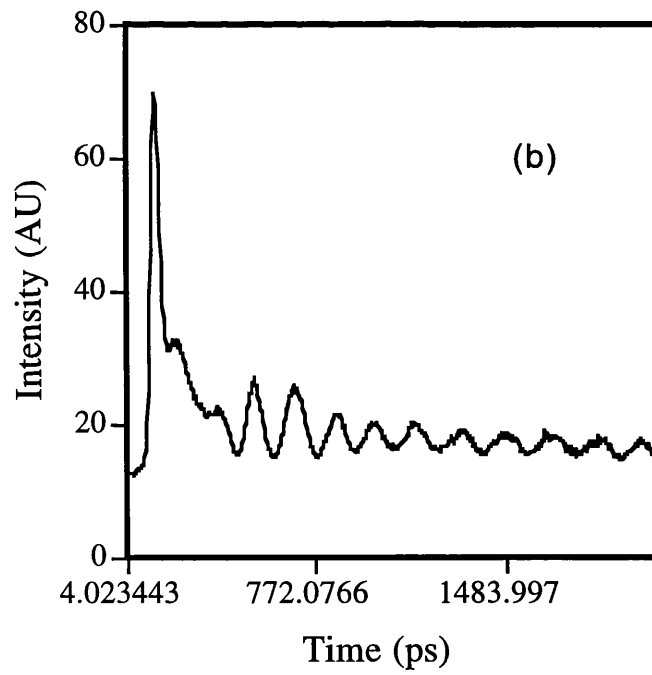
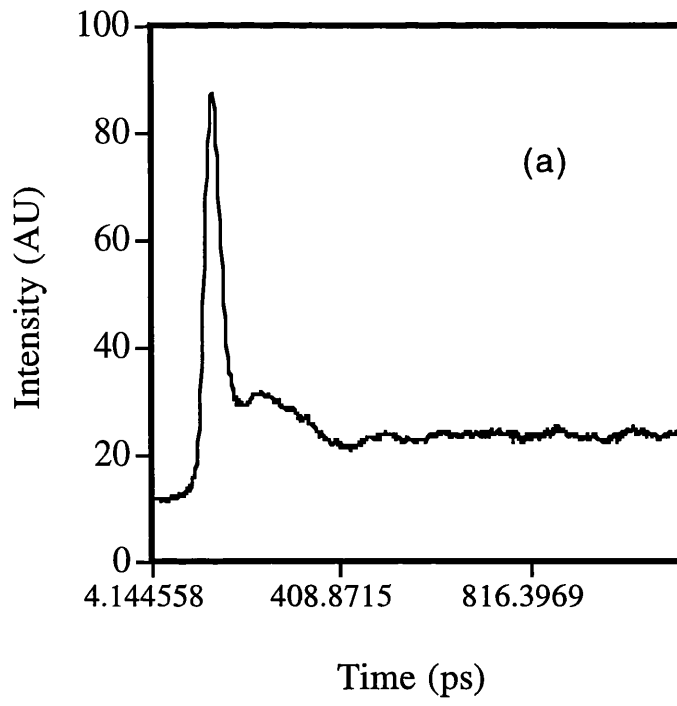
6.5.6 Streak Camera Results

Temporal measurements were then taken using a streak camera, Hamamatsu C 5680, in this Department. The self-pulsation laser diode was driven in a pulsed regime using a 2 ns pulse generator. The output from the device was collimated and then focused onto the slit of the camera. The streak camera technique gave a temporal resolution of less than 2 ps with both the pulse width and the repetition frequency of the Q-switched pulse train observed accurately.

The results showed high repetition rates. One device with a cavity length of 400 μm and saturable absorber length of around 16 μm was observed to self-pulsate at 12.5 GHz with a full width at half maximum of 20 ps. The drive current to the gain section was 480 mA and the saturable absorber was reverse biased by 4.6 V.

6.5.7 The Effect of Reverse Bias on Self-Pulsation

The effect of the reverse bias on the self-pulsation frequency was also observed and recorded with the streak camera. The gain current was kept constant, with a average current of 134 mA, while the reverse bias was increased from 0 to 7 V. The evolution of the observed pulse train with an increasing reverse bias voltage applied to the saturable absorber is shown in Fig. 6.15. Fig. 6.15 (a) shows the effect of applying a pulse to the laser with zero reverse bias on the saturable absorber. This unpumped region still produces enough absorption and hence enough instability along the laser cavity to produce relaxation oscillations in the light output which are observed for the first nanosecond, after which the laser runs cw. Fig. 6.15 (b) shows the effect of a reverse bias of 1.8 V across the saturable absorber. As the reverse bias increased to 2.4 V, Fig. 6.15 (c), the pulse train becomes well resolved indicating an increase in absorption. At 5.1 V, Fig. 6.15 (d), the pulse train starts to become less resolved, indicating a decrease in absorption. This implies that the absorption of the saturable absorber has a non-monotonic dependence on the applied bias voltage.



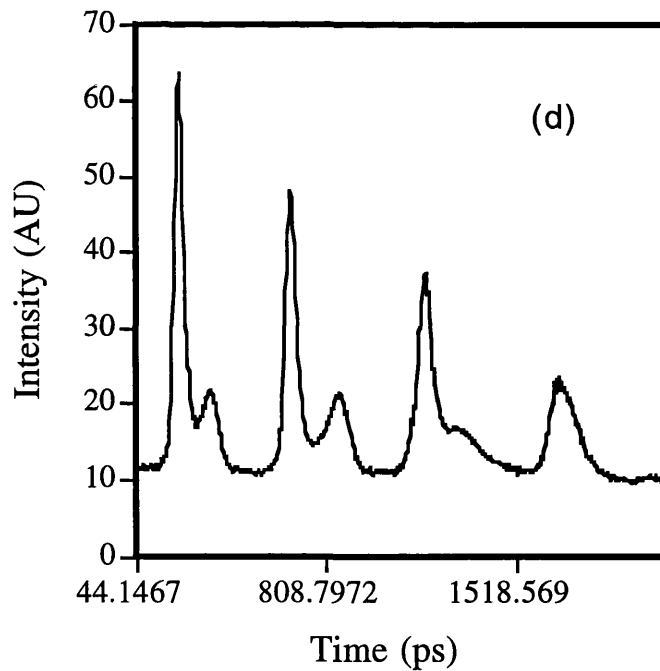
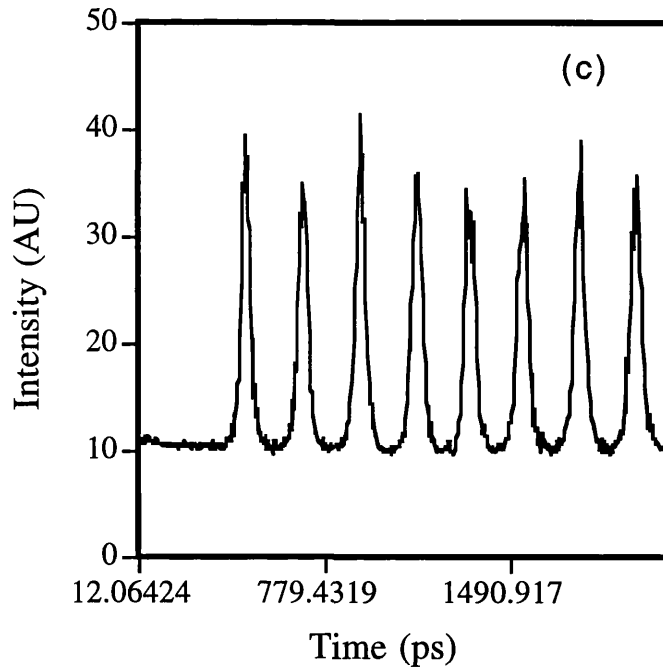


Fig. 6.15: The effect of reverse bias on a two-section laser driven by a constant current, 134 mA, taken by streak camera. a) 0 V reverse bias, b) 1.8 V, c) 2.5 V, and d) 5.1 V.

In Fig. 6.16, we see the dependence of the repetition rate with the saturable absorber reverse voltage. Increasing the magnitude of the reverse voltage, the repetition rate decreases from 7.2 GHz at 1.8 V to 4.6 GHz at 2.1 V, increasing again to 5.5 GHz at 2.5 V. As the reverse bias is increased to 4.8 V the repetition frequency decreases to another minimum of 3.5 GHz. The repetition frequency then increases to another maximum at about 6 V corresponding to a self-pulsating frequency of 6 GHz. These results demonstrate that the absorber section may be used to control the repetition frequency of the pulse train.

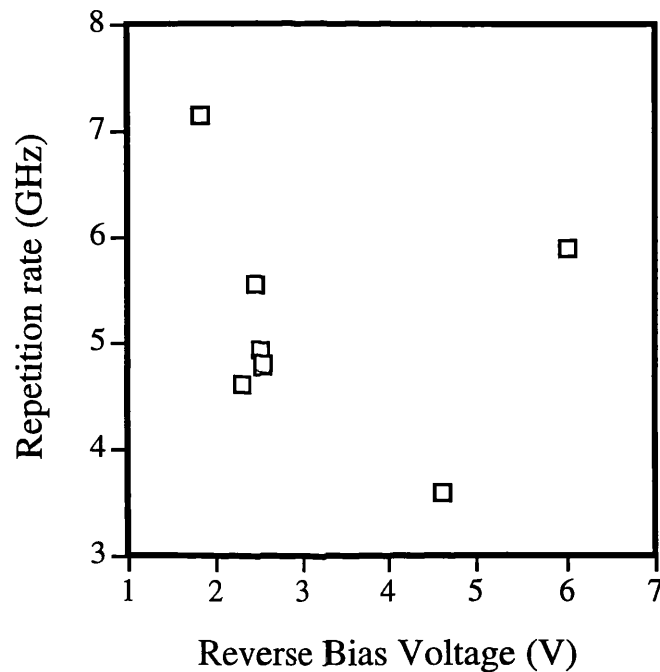


Fig. 6.16: Repetition rate dependence on the saturable absorber voltage taken from streak camera results.

In Fig. 6.17, the dependence of the pulse width with the saturable absorber reverse voltage is shown. We can see that, increasing the reverse voltage from 1.8 V to 2.1 V, the pulse width decreases from 80 ps to around 50 ps, and further increasing the voltage widens the pulse width again. The pulse width then decreases to around 30 ps at 4.6 V, and then increasing the voltage to around 6 V the pulse width widens yet again. This indicates that there is an optimal operating point for the devices which depends on the desired frequency and pulsewidth.

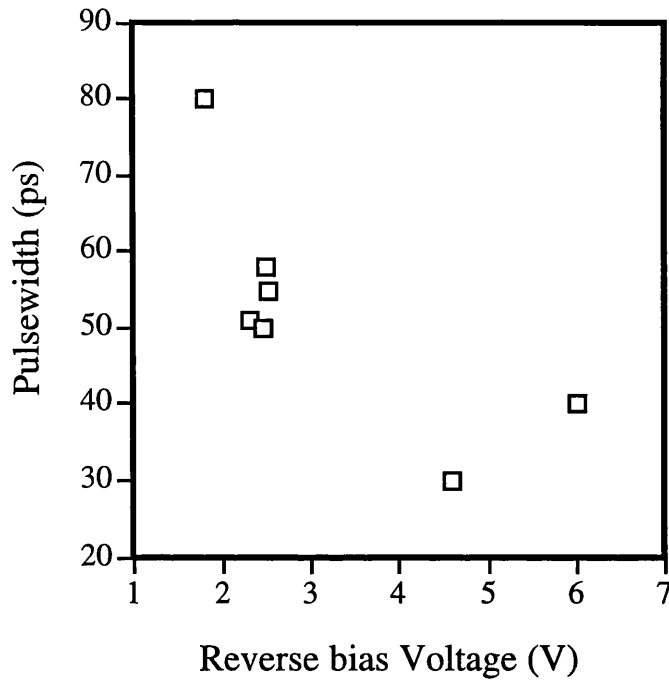


Fig. 6.17: Pulse width dependence on the saturable absorber voltage.

6.5.8 CW Measurements

The current-light characteristics of the same laser as in Fig. 6.10 were taken in CW operation. The laser was tested using the laser test rig shown in Fig. 6.19, with both sections of the p-contact forward biased. For this experiment, the fibre was only connected to the power meter and the output power from the laser was measured for the variation of the injected current on the laser. The temperature was maintained by a Peltier cooler at 15 °C. A typical light-current result is illustrated in Fig. 6.18; the threshold current is around 13 mA. The threshold is 3 mA higher in this case than in pulsed operation due to heating effects.

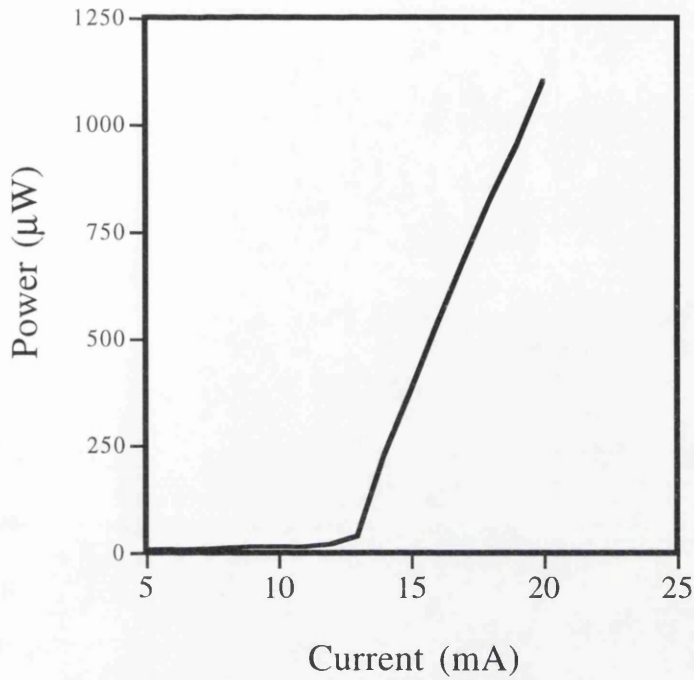


Fig. 6.18: Light-Current characteristic in CW case.

Next, the two-section devices were tested with a constant current source in a Peltier cooler sample holder, Fig. 6.19.

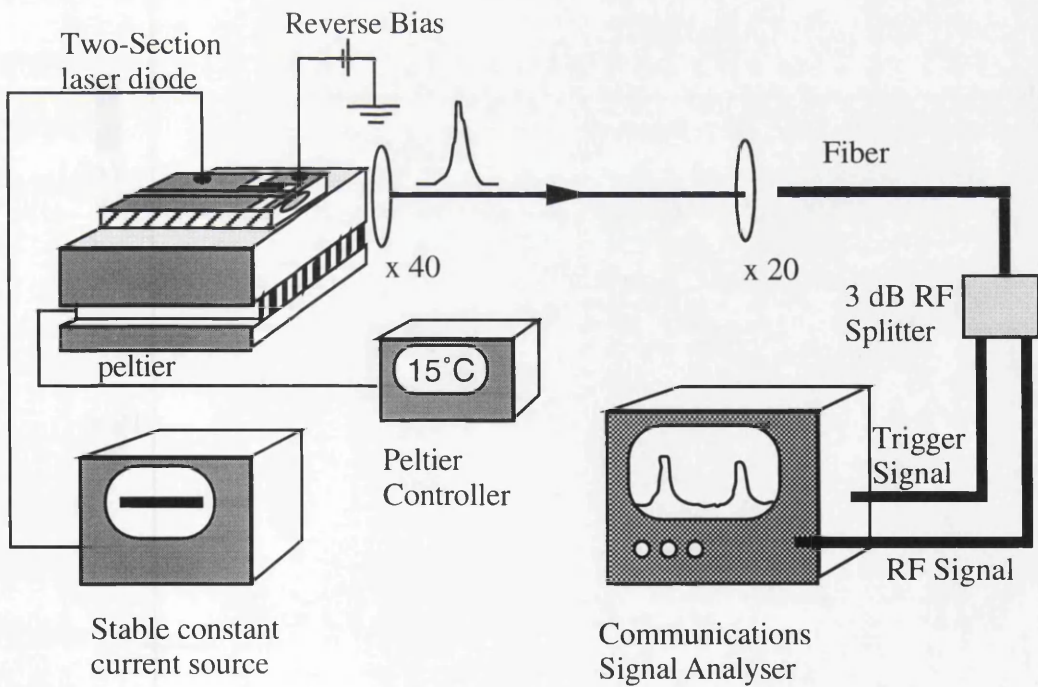


Fig. 6.19: Schematic diagram of an experimental set-up to measure CW passive Q-switching.

Passive Q-switching was obtained by applying a constant current to the gain section and a reverse bias to the saturable absorber. The reverse bias circuit had a 1 k Ω current limiting resistor to protect the saturable absorber from breaking down. The Peltier cooler was set to 15 °C during the experiment. The optical pulse from the laser was collected by a collimating lens (x 40) and focused onto a photodiode via a single mode fiber. The output from the detector was divided into two equal signals using a RF splitter. One signal was connected to the head of sampling oscilloscope (Tektronics CSA 402), the other electrical signal was used to trigger the oscilloscope via a photodiode. The optical pulses could then be monitored in time. One such trace is shown in Fig. 6.20. The laser in this case was driven by a 47 mA current with 1.2 V reverse bias present across the saturable absorber, and had a self-pulsating frequency of 1.1 GHz. Due to electrical reflections from the RF splitter, small oscillations are seen in between each pulse.

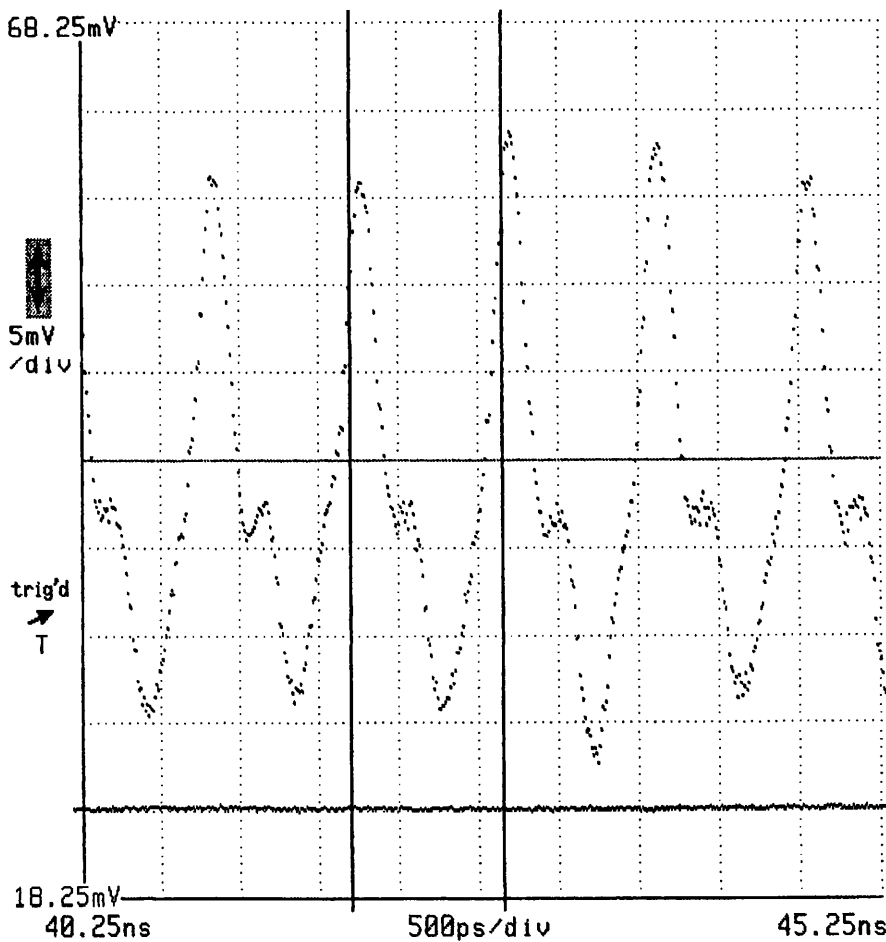


Fig. 6.20: Trace from a communications signal analyser of a CW pulse train.

6.6 High Speed Material

A reduction in the threshold current density is not the only advantage of using strained active layers in heterostructure injection lasers—predictions have also been made of significantly higher speed operation. The higher modulation frequencies that can be obtained in lasers with quantum (QW) active layers are thought to be linked to an enhancement of the gain and its energy derivative near QW levels. For example, in QW lasers with strained layers, the modulation bandwidth can be increased by a factor of 4 compared with DH lasers [32]. It has been shown [33, 34] that as well as the addition of strain in the active region, an increase in the number of quantum wells and the addition of p-doping in the barriers can increase the modulation response. The mechanisms that produce these high values of intrinsic modulation bandwidth are discussed in Chapter 1.

Initially, by using a high speed material structure with four wells compressively strained by 35% and p-doped similarly to reference [33], it was proposed that a decrease in pulse width and an increase in repetition frequency would be seen. The material structure was grown but unfortunately was found not to lase due to strain relaxation, so a new material structure was designed and the wafer was grown. Because of lack of time, only the quality of the material was investigated.

6.6.1 Material Structure and Characterisation

The lasers were fabricated using a wafer, QT 880, which included an active layer of InGaAs/GaAs double quantum wells, grown by metal organic chemical vapour deposition (MOCVD) in Sheffield University. The semiconductor material structure was sequentially grown on a (100) n⁺-GaAs substrate misoriented by 3 degrees; a 0.1 μm n⁺-GaAs buffer layer (Si- doped 1x10¹⁸ cm⁻³); a 0.1 μm graded layer (Si- doped 1x10¹⁸ cm⁻³); a 1.2 mm n-Al_{0.60}Ga_{0.40}As cladding layer (Si- doped 1x10¹⁸ cm⁻³); a 0.15 μm GRINSCH layer (undoped); a 250 Å GaAs undoped waveguide layer; two 50 Å In_{0.22}Ga_{0.78}As wells separated by a 100 Å

GaAs barrier; a 250 Å GaAs undoped waveguide layer; a 0.15 μm GRIN SCH layer (undoped); a 1.2 μm p-Al_{0.60}Ga_{0.40}As cladding layer (C- doped 5-6x10¹⁷); and a 0.2 μm p⁺-GaAs contact layer (Zn- doped 8.6x10¹⁸).

The use of such a high Al mole fraction in the cladding layers, allows an increase in the waveguide vertical confinement factor, leading both to an increase in relaxation frequency at a given current, due to an increase in photon density, and a substantial decrease in core and cladding layer thickness.

In order to investigate the quality of the material and the lasing wavelength, a simple wide oxide stripe gain guided laser was fabricated. Information such as threshold current density for infinite cavity length (J_o), internal quantum efficiency (η_i) and internal propagation loss (α) can be obtained from $L-I$ (light output power versus injected current) characteristics of these broad area oxide stripe lasers [20]. It is useful to have an good idea of the quality of the material prior to the fabrication of more complex structures and devices.

6.6.2 Fabrication, Experiment and Results

Initially, oxide stripe lasers were fabricated in the following manner: the samples were first coated with a layer of 200 nm of SiO₂. 75 μm wide stripe windows were defined using photolithography and C₂F₆ RIE to open the windows. These lasers are gain-guided and the 75 μm wide stripe used allows the current spreading effect in the upper cladding layer of the material to be neglected. The current spreading makes the effective current injection area larger the actual area of the stirpe structure, which introduces an error to the calculation of the current densities [35]. Samples were then thinned to a thickness of around 160 nm and metal contacts (n—Au/Ge/Au/Ni/Au, 14nm/14nm/14nm/11nm/240nm, and p—Ti/Pb/Ti/Au, 30nm/33nm/30nm/140nm) were evaporated using a computer controlled metal evaporator ('Plassys'). The samples were then annealed using RTA at 360 °C

for 60 s and scribed into individual lasers with lengths of 400, 600, 800, and 1000 μm .

The lasers were operated in pulsed current mode at room temperature using the test rig shown in Fig. 6.9. The current pulse width was 400 ns and the repetition frequency was 1 kHz (i.e. duty cycle 0.04 %). Measurements such as L - I characteristics and lasing spectrum were performed. The lasing wavelength was determined using an optical spectrum analyser (Advantest) and was taken from 800 μm cavity length lasers operated above threshold.

The lasers with the lowest threshold currents and best quantum efficiencies were chosen in determining the device and material parameters. These devices were assumed to have the best metal contacts and facets. Fig. 6.21 shows the L - I characteristics of the best lasers with lengths from 400 μm to 1000 μm . 'Kinks' in the curves normally imply that the laser, at certain current, is switching from one transverse mode to a different one as is expected in oxide stripe lasers.

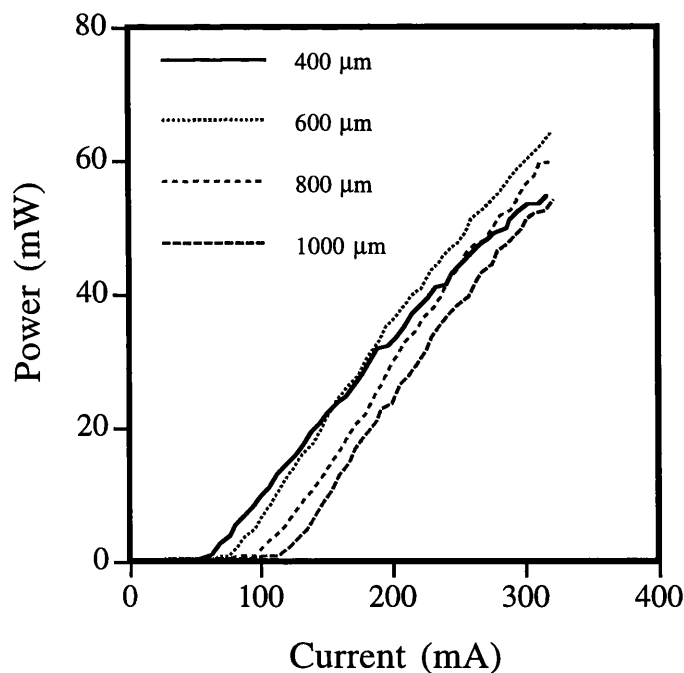


Fig. 6.21: Light-Current characteristics for different cavity length lasers.

From Fig. 6.21, the threshold current and quantum efficiency were obtained. Fig. 6.22 shows a plot of $\ln(J_{th})$ against $1/L$ from which we can obtain the threshold current density for an infinitely long laser. The intercept on the y-axis (where $L=\infty$) yields a value of around 144 A/cm².

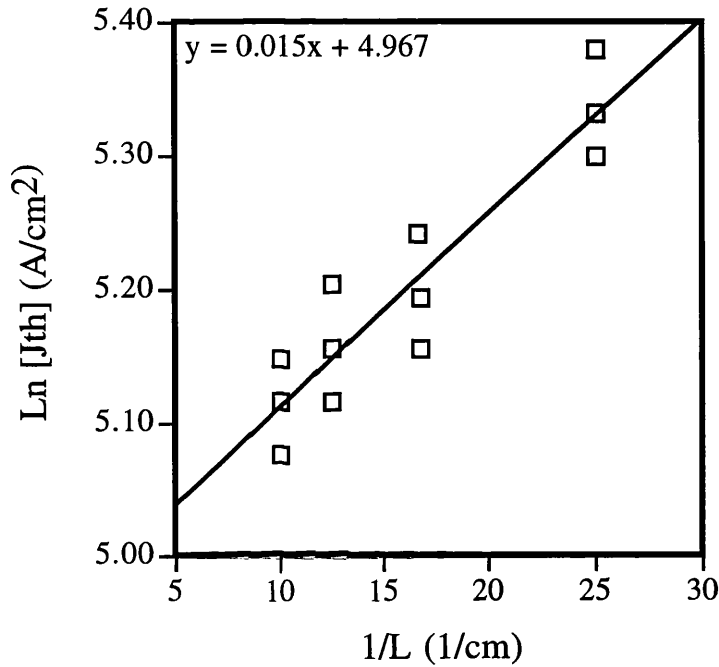


Fig. 6.22: Graph of $\ln(J_{th})$ against $1/L$.

The gain factor, $n\Gamma g_0$, can be found from the gradient of this graph assuming a power reflection coefficient of $R = 0.3$. For these devices the gain factor is equal to around 21 cm⁻¹.

We can find internal quantum efficiency and total internal loss by plotting $1/\eta_{ex}$ as a function of cavity length, Fig. 6.23.

Using Equation:

$$\frac{1}{\eta_{ex}} = \frac{1}{\eta_i} - L \left(\frac{\alpha}{\eta_i \ln R} \right) \quad (6.3)$$

where η_{ex} is the external quantum efficiency or slope efficiency above threshold, η_i is the internal quantum efficiency, α is the loss coefficient, L is the cavity length, and R is the reflection coefficient of the end facets. It can be seen that the intercept with the y-axis is equal to the inverse of the internal quantum efficiency which is equal to 78% in this case. Equation (6.3) also states that the gradient of the graph is equal to $-\alpha/\eta_i \ln(R)$ from which the material loss at the lasing wavelength, α , can be easily found. Assuming $R = 0.3$ and $\eta_i = 0.78$ then for this material, α is equal to 3 cm^{-1} . Therefore these results indicate that the material has low losses and good efficiency.

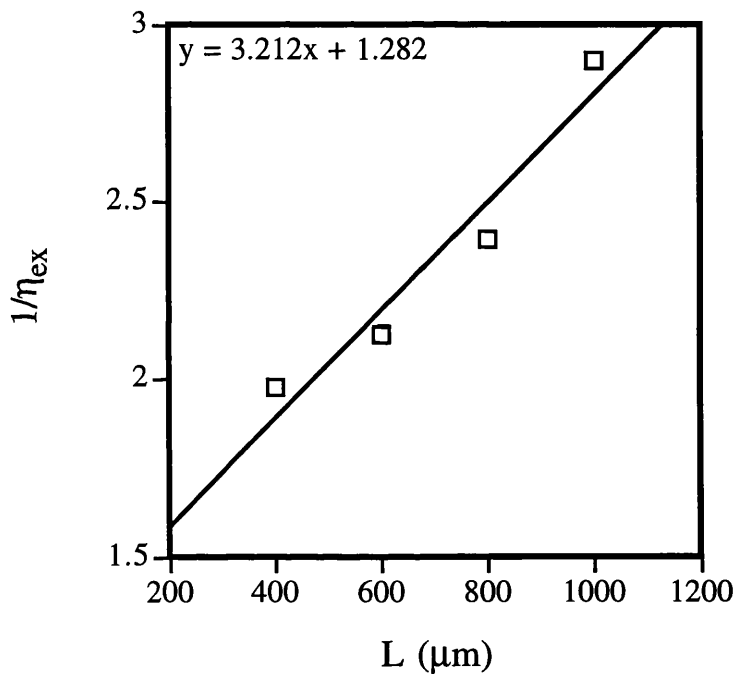


Fig. 6.23: Plot of $1/\eta_{ex}$ as a function of the laser cavity length.

Fig. 6.24 shows the output spectrum of the laser with $800 \mu\text{m}$ cavity length at room temperature. This spectrum was obtained from laser operated just above threshold (150 mA). It lased multi-moded since the laser is gain-guided with the weak optical confinement and is a simple Fabry-Perot device. The lasing wavelength is around 980 nm.

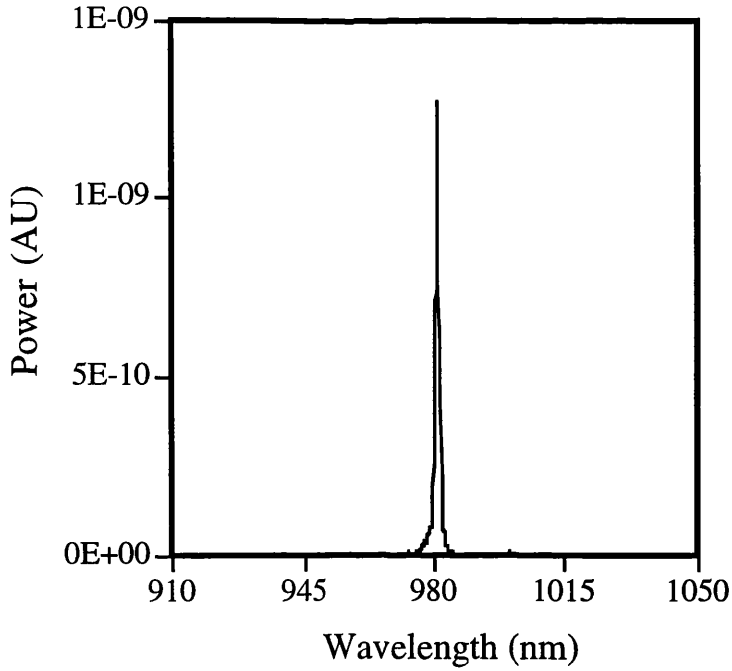


Fig. 6.24: Spectrum of oxide stripe laser from material QT 880.

6.7 Temperature Dependence of the Threshold Current

The two dimensional (2D) nature of electron motion in the quantum well (QW) structure introduces several unique features to semiconductor lasers as discussed in Chapter 1. For instance, the threshold current of QW laser is found to be less temperature sensitive than that of conventional double heterostructure (DH) lasers [36]. Therefore, DQW material, QT 683, was investigated by measuring the threshold current at low temperatures to see if threshold current was strongly temperature dependent.

6.7.1 Introduction

The threshold current density of a semiconductor laser is usually expressed by [36]:

$$J_{th} = J_0 \exp\left[\frac{(T_2 - T_1)}{T_0}\right] \quad (6.4)$$

where T_0 is the characteristic temperature, which is used to express the temperature sensitivity of threshold current. A high value of T_0 indicates that the fractional change of I_{th} between T_2 and T_1 is small.

Experimental observations of the threshold current density (J_{th}) in the vicinity of room temperature have a strong fractional temperature dependence [37]. This is due to recombination in the barrier, chiefly by nonradiative processes [38]. The carriers in the QW's are in thermal equilibrium with those in the barriers. As the temperature is increased, the carriers tend to spend more time in the barrier due to a higher energy level where, if there are traps, they can suffer nonradiative recombination. This reduces the lifetime of carriers and the efficiency of the laser and, J_{th} is increased.

Different values of T_0 for GaAs devices from 180 to 437 K have been reported [38]. High values of T_0 have been reported by Weimann and Schlapp [39] who measured " $T_0 > 300$ K" for modified MQW lasers; GRIN-SCH devices had T_0 in the range 260-290 K.

Also, it has been reported that the temperature dependence of threshold current density depends upon factors such as cavity length and the number of quantum wells [37]. In addition, it has been shown that threshold current density depends upon the barrier height in the MQW [40]. As the barrier height becomes too high, it is increasingly difficult for carriers to pass over the barrier and be injected into the next well. The carrier injection efficiency is therefore decreased, so resulting in increased J_{th} .

6.7.2 Material, Experiment and Results

The double quantum well (DQW) laser material, QT 683, used here was grown by MOVPE at Sheffield University. The device structure was sequentially grown on a n^+ -GaAs (Si- doped $1 \times 10^{18} \text{ cm}^{-3}$); a $1.5 \mu\text{m}$ n - $\text{Al}_{0.58}\text{Ga}_{0.42}\text{As}$ cladding layer (Si- doped $2 \times 10^{17} \text{ cm}^{-3}$); a $0.1 \mu\text{m}$ $\text{Al}_{0.31}\text{Ga}_{0.69}\text{As}$ undoped waveguide layer; an

undoped active region consisting of two 100 Å GaAs quantum wells separated by 100 Å Al_{0.31}Ga_{0.69}As barrier; a 0.1 μm Al_{0.31}Ga_{0.69}As undoped waveguide layer; a 0.7 μm p- Al_{0.58}Ga_{0.42}As upper cladding layer (C- doped 1.1x10¹⁸ cm⁻³); and a 0.1 μm p⁺- GaAs contact layer (Zn- doped 1.3x10¹⁹ cm⁻³).

The material was tested by making 75 μm oxide stripe lasers in the usual fashion, cleaved into lengths from 300 to 1200 μm to measure the laser properties. The measurements of temperature dependence of threshold current were carried out at different temperatures. The devices used for the experiment were oxide insulated 75 μm wide stripe lasers, 900 μm cavity length. The measurement was carried out in pulse mode, with pulse width of 3 ns and a repetition rate of a few kHz, so heating effects should have been minimal.

The threshold currents were measured for temperature from 77 to 300 K. A graph of Ln(J_{th}) versus temperature is shown in Fig. 6.25. One can obtain the value of T_0 , from Fig. 6.25 by taking Ln(J_{th}) at two different temperatures and using Equation (6.4).

T_0 was found to be 290 K which is in good agreement with the literature. Finally, the result shows that the MOVPE material has weak temperature dependence, so it is good quality laser material.

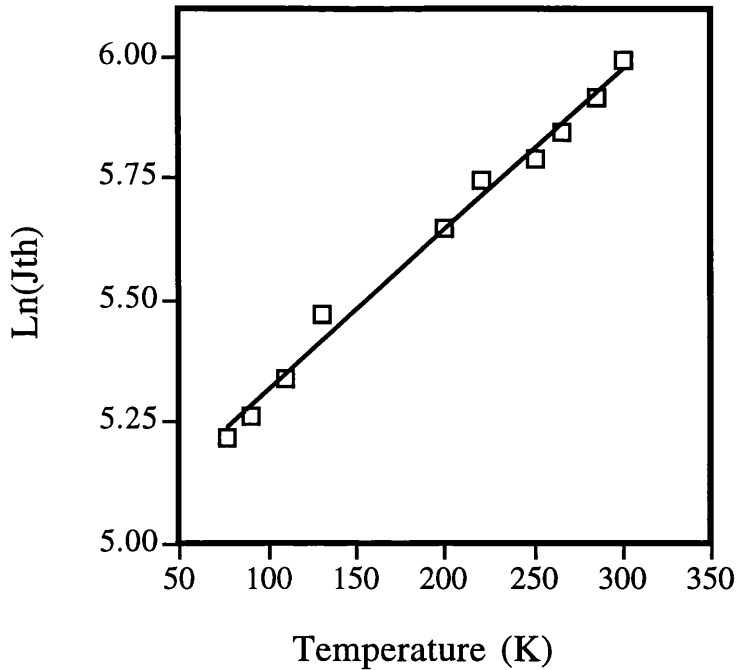


Fig. 6.25: Plot of $\text{Ln}(J_{th})$ versus Temperature for material QT 683.

6.8 Conclusions

This Chapter has reviewed the principles and the physics involved in the Q-switching process, with particular emphasis on passively Q-switched semiconductor lasers. The different methods for achieving Q-switching in semiconductors have been discussed. The fabrication technique used to produce two-section lasers was described in detail. The results of the device characterisation, from material QT 674, were given showing low threshold currents and high quantum efficiencies. Then, the results of the two-section self-pulsating lasers were presented. The devices were first tested in a pulsed regime to examine their self-pulsation behaviour at high currents, then the self-pulsating characteristics were examined in a CW regime.

The high speed material, QT 880, was designed and oxide stripe lasers were made to characterise the material. However, insufficient time prevented an investigation of the Q-switching behaviour of two section lasers from this material.

Finally, the temperature dependence of the threshold current of the material QT 683 was investigated. The results show a state of the art temperature dependence of threshold current for MOVPE material.

6.9 References

- [1] R. N. Hall, G. E. Fenner, J. D. Kingsley, T. J. Soltys, and R. O. Carlson, "Coherent light emission from GaAs junctions", *Phys. Rev. Lett.*, Vol. 9, pp. 366-368, 1962.
- [2] M. I. Nathan, W. P. Dumke, G. Burns, F. H. Dill, Jr, and G. Lasher, "Stimulated emission of radiation from GaAs p-n junctions", *Appl. Phys. Lett.*, Vol. 1, pp. 62-64.
- [3] N. Holonyak, Jr, and S. F. Bevacqua, "Coherent (visible) light emission from Ga (As_{1-x}P_x) junctions", *Appl. Phys. Lett.*, Vol. 1, pp. 82-83, 1962.
- [4] T. M. Quist, R. H. Rediker, R. J. Keyes, W. E. Krag, B. Lax, A. L. McWhorter, and H. J. Zeiger, "Semiconductor maser of GaAs", *Appl. Phys. Lett.*, Vol. 1, pp. 91-92, 1962.
- [5] G. J. Lasher, "Analysis of a proposed bistable injection laser", *Solid-State Electron.*, Vol. 7, pp. 707-716, 1964.
- [6] K. C. Kao, and G. A. Hockham, "Dielectric-fibre surface waveguide for optical frequencies", *Proc. IEE*, 113, pp. 1151-1158, 1966.
- [7] T. Miya, T. Terunuma, T. Hosaka, and T. Miyashita, "Ultimate low-loss single-mode fibre at 1.55 μm ", *Electron. Lett.*, Vol. 15, pp. 106-108, 1979.
- [8] D. N. Payne, and W. A. Gambling, "Zero material dispersion in optical fibres", *Electron. Lett.*, Vol. 11, pp. 176-178, 1975.
- [9] N. G. Basov, "0-1 dynamics of injection lasers", *IEEE J. Quantum Electron.*, Vol. 4, pp. 855-864, 1968.
- [10] E. S. Yang, P. G. McMullin, A. W. Smith, J. Blum, and K. K. Shih, "Degradation-induced microwave oscillation in double heterostructure injection lasers", *Appl. Phys. Lett.*, Vol. 24, pp. 324-327, 1974.
- [11] R. W. Dixon, and W. B. Joyce, "A possible model for sustained oscillations (pulsations) in AlGaAs double-heterostructure lasers", *IEEE J. Quantum Electron.*, Vol. 15, pp. 470-474, 1979.

- [12] Ch. Harder, K. Y. Lau, and A. Yariv, "Bistability and pulsations in semiconductor lasers with inhomogeneous current injection", *IEEE J. Quantum Electron.*, Vol. 18, pp. 1351-1361, 1982.
- [13] H. Uenohara, Y. Kawamura, H. Iwamura, K. Nonaka, and T. Kurokawa, "Side-light injection MQW bistable laser using saturable absorption and gain quenching", *Electron. Lett.*, Vol. 28, pp. 1973-1975, 1992.
- [14] J. Hörer, K. Weich, M. Möhrle, and B. Sartorius, "Optimization of the optical switching characteristics of two-section Fabry-Perot lasers", *IEEE Photonics Tech. Lett.*, Vol. 5, pp. 1273-1275, Nov. 1993.
- [15] D.J. Derickson, R. J. Helkey, A. Mar, J. R. Karin, J. G. Wasserbauer, and J. E. Bowers, "Short pulse generation using multisegment mode-locked semiconductor lasers", *IEEE J. Quantum Electron.*, Vol. 28, pp. 2186-2202, Oct. 1992.
- [16] J. A. Valdmanis and B. Mourou, "Subpicosecond electrooptic sampling: principles and applications", *IEEE J. Quantum Electron.*, Vol. 22, pp. 67-78, Jan. 1986.
- [17] D. Z. Tsang, and J. N. Walpole, "Q-switched semiconductor diode lasers", *IEEE J. Quantum Electron.*, Vol. 19, pp. 145-156, Feb. 1983.
- [18] P. Horan, and W. Blau, "Optical nonlinearity near the bandgap in semiconductor", *Contemp. Phys.*, Vol. 28, pp. 59-68, 1987.
- [19] G. H. B. Thompson, "Physics of Semiconductor Laser Devices", John Wiley & Sons, Ltd, 1980.
- [20] P. S. Zory, Jr. (Editor), "Quantum Well Laser", *Quantum Electronics: principles and applications series*, Academic Press, 1993.
- [21] D. A. B. Miller, D. S. Chemla, T. C. Damen, A. C. Gossard, W. Wiegmann, T. H. Wood, and C. A. Burrus, "Band-edge absorption in quantum well structures: The Quantum Confined Stark Effect", *Phys. Rev. Lett.*, Vol. 53, pp. 2173-2176, 1984.
- [22] S. Tarucha, H. Kobayashi, Y. Horikoshi, and H. Okamoto, "Carrier-induced energy-gap shrinkage in current-injection GaAs/AlGaAs MQW heterostructures", *Jpn. J. Appl. Phys.*, Vol. 23, pp. 874-878, 1984.

- [23] Y. Arakawa, A. Larsson, J. Paslaski, and A. Yariv, "Active Q switching in a GaAs/AlGaAs multiquantum well laser with an intracavity monolithic loss modulator", *Appl. Phys. Lett.*, Vol. 48, pp. 561-563, 1986.
- [24] M. Ueno, and R. Lang, "Conditions for self-sustained pulsation and bistability in semiconductor lasers", *J. Appl. Phys.*, Vol. 58, pp. 1689-1692, 1985.
- [25] F. Stern, "Calculated spectral dependence of gain in excited GaAs", *J. Appl. Phys.*, Vol. 47, pp. 5382-5389, 1976.
- [26] P. W. Smith, Y. Silberberg, and D. A. B. Miller, "Mode-locking of semiconductor diode lasers using saturable excitonic nonlinearities", *J. Opt. Soc. Am. B*, Vol. 2, pp. 1228-1236, 1985.
- [27] A. E. Siegman, "Lasers", Oxford University Press, 1986.
- [28] M. P. Kesler and E. P. Ippen, "Subpicosecond gain dynamics in GaAlAs laser diodes", *Appl. Phys. Lett.*, Vol. 51, pp. 1765-1767, 1987.
- [29] P. P. Vasil'ev, "High-power high-frequency picosecond pulse generation by passively Q-switched 1.55 μm diode lasers", *IEEE J. Quantum Electron.*, Vol. 29, No. 6, pp. 1687-1692, 1993.
- [30] S. M. Sze, "Semiconductor Devices: Physics and Technology", Wiley, 1985.
- [31] P. N. Kember, "Plasma deposition of insulators for semiconductor applications", *Plasma News*, Oxford Plasma Technology, No. 4, Sep. 1992.
- [32] K. Uomi, N. Chinone, T. Ohyoshi, and T. Kajimura, "High relaxation oscillation frequency (beyond 10 GHz) of GaAlAs multiquantum well lasers", *Japan. Appl. Phys.*, Vol. 24, pp. L539-L541, 1985.
- [33] J. D. Ralston, S. Weisser, I. Esquivias, E. C. Larkins, J. Rosenzweig, P. J. Tasker, and J. Fleissner, "Control of differential gain, nonlinear gain, and damping factor for high-speed application of GaAs-based MQW lasers", *IEEE J. Quantum Electron.*, Vol. 29, Jun. 1993.
- [34] K. Uomi, "Modulation-doped multi-quantum well (MD-MQW) lasers", *Japan. J. Appl. Phys.*, Vol. 29, pp. 81-87, Jan. 1990.
- [35] A. Yariv, "Optical Electronics", CBS College Publishing, 1985.

- [36] Y. Arakawa and H. Sakaki, "Multidimensional quantum well laser and temperature dependence of its threshold current", *Appl. Phys. Lett.*, Vol. 40, 1982.
- [37] P. Blood, A. L. Kucharska, C. T. Foxon, and K. Griffiths, "Temperature dependence of spontaneous emission in GaAs-AlGaAs quantum well lasers", *Appl. Phys. Lett.*, Vol. 55, 1989.
- [38] P. Blood, E. D. Fletcher, K. Woodbridge, K. C. Heasman and A. R. Adams, "Influence of the barriers on the temperature dependence of the threshold current in GaAs-AlGaAs QW lasers", *J. Quantum Electron.*, Vol. 25, pp. 1459-1468, 1989.
- [39] G. Weimann and W. Schlapp, "GaAs-AlGaAs MQW and GRIN-SCH lasers grown by molecular beam epitaxy", *Phys. Rev. B*, Vol. 129, pp. 459-464, 1985.
- [40] W. T. Tsang, "Heterostructure semiconductor lasers prepared by molecular beam epitaxy", *IEEE J. Quantum Electron.*, Vol. 20, 1984.

Chapter 7

7.1 Summary and Conclusions

This Chapter presents a summary of the more important aspects of the two-photon absorption waveguide autocorrelator and passively Q-switched two-section semiconductor lasers that have been studied in this thesis and gives a general conclusion to this project, as well as some prospects for future work.

Chapter one is an introduction to the thesis. It gave a general outlook on quantum well structures, semiconductor lasers, and outlined the advantages of quantum well lasers over the conventional double heterostructure lasers. The methods of short pulse generation from diode lasers including Q-switching, gain-switching and mode-locking were then described, and the methods of detection of ultra-short pulses, i.e. direct and indirect autocorrelations, were addressed.

Chapter two provides the theoretical background to the work, with particular emphasis on linear and non-linear absorption (i.e. free carrier absorption, two-photon absorption) in bulk semiconductor materials. The concept of excitons in bulk and quantum well materials were then described.

The processes involved in the techniques for fabrication of waveguide autocorrelator devices used in this work, from the waveguide theory and numerical methods necessary to design the material were described in Chapter 3. The device employs two photon absorption, which is a non-linear mechanism, and it is this which gives rise to the autocorrelation trace, from which the pulsewidth can be measured.

Chapter four provides a brief theoretical treatment of ultra-short optical pulses, which leads to the concept of a bandwidth-limited pulse. This is followed by a description of the methods of detection and measurements of such pulses. The

advantages of non-linear autocorrelation techniques, i.e. intensity and interferometric autocorrelations, over the linear counterparts for pulsewidth measurements were discussed. The working characteristics of the waveguide autocorrelator were fully investigated here, and its ability for integration in optical communications systems. Its high sensitivity will make it very attractive for pulse detection and measurement systems in the communications industry.

Initially, we demonstrated the practical use of the two-photon waveguide autocorrelator, by obtaining the part of interferometric autocorrelation from a mode-locked Nd³⁺:YAG laser operating at wavelength 1.06 μm . When the laser was mode-locked at frequency of 76 MHz, the pulse width was about 100 ps. However, the whole interferometric trace was not observed because the maximum dynamic range was only 13 ps.

We then used the same waveguide to perform autocorrelations and measured the pulse width of a mode-locked Nd³⁺:YLF laser. Interferometric autocorrelation measurements have been made for the first time using the device. The pulsewidth was found to be approximately 17.7 ps, corresponding well with previous pulsewidth measurements, 16.3 ps, made using a conventional second harmonic generation (SHG) autocorrelator. Also the autocorrelation trace for a Q-switched InGaAsP/InP laser at 1.3 μm was obtained using the waveguide autocorrelator [1]. Hence there are no fundamental reasons why this type of device should not be able to perform autocorrelations on pulses at 1.5 μm . On the other hand, InGaAsP is the material of choice for this application because its two-photon absorption coefficient allows a higher sensitivity than is possible with GaAs, which has a much lower TPA coefficient [2]. Such an enhancement in β would provide good signal levels at low optical power. Therefore, the use of TPA in a semiconductor waveguide was found to be a practical and sensitive alternative to the use of SHG for autocorrelation measurements. Furthermore, the device is waveguide-based and so has the potential both for integration and for simple coupling into a fibre-based interferometer.

The complete polarisation dependence of the two-photon absorption coefficient was also obtained from photocurrent measurements in an AlGaAs waveguide autocorrelator at a wavelength of 1.047 μm . The measured contrast ratio was slightly greater than 2 which exceeds the value obtained if isotropic Kleinmann symmetry of the nonlinearity is assumed.

In addition, in this Chapter, the TPA-induced photocurrent has been characterised in a GaAs waveguide photodetector in response to femtosecond pulses at 1.5 μm . The experiments verified that the photocurrent varies inversely with optical pulse width for a twenty-fold variation in pulsewidth. The device also demonstrated a sub-nanosecond electrical response time. These experiments demonstrate the possibility of applying such devices as non-linear detectors at to retrieve peak intensity and pulse width related information at communications wavelengths at high speed.

Chapter 5 was concerned with loss measurements in a AlGaAs waveguide, in particular the loss due to single photon absorption. The theory of the Fabry-Perot technique used to measure the loss of the waveguides was addressed initially. Losses as a function of wavelength from a 5 mm long single mode waveguide, in the wavelength range 760-930 nm were measured. Linear absorption photocurrent measurements, in the wavelength range 730-1000 nm were then carried out in the same device. It was shown that, due to the creation of carriers by single photon absorption while using TPA for pulse measurements, the contrast ratio of the waveguide autocorrelator is not 2:1 as predicted theoretically. In addition, the propagation loss of the waveguide was measured to be as low as 1.37 cm^{-1} at a wavelength of 904 nm. Such low loss waveguides may form the basis for efficient guided-wave devices for integrated optoelectronics.

Chapter 6 describes the dynamic behaviour of Q-switched two-section diode lasers. First a brief description of Q-switching in semiconductor lasers was presented. The material structure and fabrication process were then described for two-

section lasers, followed by the test and characterisation of such devices. Passive Q-switching has been demonstrated in strained layer InGaAs/GaAs double quantum well material with intracavity saturable absorbers. The efficient loss modulation achieved through the quantum confined Stark effect and the carrier induced band shrinkage effect, as well as high differential gain, leads to the generation of narrow optical pulses at a high repetition rate. The results show that short pulses with a full width at half maximum of 20 ps at high repetition rates of 12.5 GHz were generated and should be useful for optical fiber communication systems and other applications requiring such high rates. Also, the absorption of the saturable absorber for quantum well material was observed to have a non-monotonic dependence on the applied reverse bias. Lack of time prevented the pulsewidth of the Q-switched semiconductor lasers being measured using the waveguide autocorrelator. This should be the subject of future work.

7.2 Future Work

A proposed autocorrelation device for future investigation is a reverse-biased p-i-n waveguide with multiple contacts along its length, which must be electrically isolated from each other. To obtain a pulse width measurement using the multi-contact autocorrelator, the pulse train would be split into two beams and then end fired into either end of the waveguide. The pulses would then propagate through the waveguide from both ends where they would form an interference wave pattern, which is measured by the change in photocurrent along the waveguide. The pulsewidth will be determined by measuring the photocurrent as a function of contact position. The advantage of this device is that the path lengths of both pulses do not have to be varied and, therefore, the coupling into the waveguide can be kept constant. Further work in this field should be used to produce a fibre-pigtailed autocorrelator. The waveguide could be fully integrated by coupling either end of the device to an input and output fibre and then wire bonded and packaged. The advantage of a possible fibre-pigtailed autocorrelator is that the Michelson

interferometer could be made up completely in fibre using a 3 dB fibre splitter to divide the pulse train into two paths, with two polarisation controlled fibres and a fibre stretcher in one arm of the interferometer. The fibres could then be recombined and connected to the packaged autocorrelator.

Future work on two-section semiconductor lasers will involve the design and fabrication of devices with higher strain, increased number of wells, and p-doped MQW layers to optimise the device parameters and achieve short optical pulses and higher self-pulsation repetition frequencies.

7.3 References

[1] F. R. Laughton, J. H. Marsh, D. A. Barrow, and E. L. Portnoi, "The two-photon absorption semiconductor autocorrelator", *IEEE J. Quantum Electron.*, Vol. 30, No. 3, pp. 838-845, 1994.

[2] H. K. Tsang, L. Y. Chan, J. B. D. Soole, H. P. LeBlanc, M. A. Koza, and R. Bhat, "High sensitivity autocorrelation using two-photon absorption in InGaAsP waveguides", *Electron. Lett.*, Vol. 31, No. 20, pp. 1773-1774, 1995.